# SPIN TRANSFER TORQUE INDUCED OSCILLATION AND SWITCHING IN MAGNETIC TUNNEL JUNCTION

A DISSERTATION
SUBMITTED TO THE FACULTY OF THE GRADUATE SCHOOL
OF THE UNIVERSITY OF MINNESOTA
BY

YISONG ZHANG

IN PARTIAL FULFILLMENT OF THE REQUIREMENTS
FOR THE DEGREE OF
DOCTOR OF PHILOSOPHY

PROFESSOR JIAN-PING WANG, ADVIOSR

May 2014

# Acknowledgements

I would like to express the deepest appreciation to all the following people. First, I would like to show my greatest appreciation to my Ph.D advisor Professor Jian-Ping Wang for all his guidance, support and patience over the years. I've greatly benefited from his knowledge, experience and vision on scientific research. I would also like to thank all my committee members: Professor Randall Victora for his excellent teaching and knowledge sharing; Professor Paul Crowell for his valuable discussion and significant help; and Professor Anand Gopinath for his useful suggestion and continuing support.

I would like to thank Dr. Xiaofeng Yao and Dr. Hao Meng for all their knowledge and experience I've inherited. Special thanks to Dr. Hui Zhao for all the collaboration and in-depth discussion. I would also like to thank all the lab colleagues, MINT and MRSEC students both past and current for their friendship and help: Dr. Yunhao Xu, Dr. Xiaoqi Liu, Yuanpeng Li, Dr. Nian Ji, Dr. Ying Jing, Dr. Hao Wang, Dr. Liang Tu, Dr. Andrew Lyle, Dr. Tofizur Rahma, Xuan Li, Todd Klein, Brain Glass, Jonathan Harms, Yi Wang, Yinglong Feng, Xiaowei Zhang, Xiaohui Chao, Angeline Klemm, Shaoqian Yin, Meiyin Yang, Yang Lv and Jinmin Liu, Dr. Mahdi Jamali, Dr. Xi Chen, Tao Qu, Dr. Te-Yu Chen and Dr. Jaesang Oh.

This work was supported primarily by the MRSEC Program of the National Science Foundation under Award Number DMR-0819885. Addtionally, I want to thank all of the staff at the Nanofabrication Center (NFC).

I am deeply grateful to my wife Lijuan You, my mom and dad. They are always there supporting me and encouraging me with their love. This thesis is dedicated to them.

# Abstract

Spin transfer torque (STT) induced magnetization switching and oscillation in nanometer scale magnetoresistance (MR) devices have been studied intensively due to its direct application in the non-volatile STT random access memory (STT-RAM) and its potential application in the high frequency spin torque oscillatior (STO). STO could be used in high-density microwave signal processor and chip-to-chip communication system due to its nanometer scale footprint and ultra high oscillation frequency. STO has also been suggested in the magnetic recoridng head for the microwave assisted magnetic recording (MAMR) and in the high-speed magnetic reader for future hard disk drive. However, several critical engineering challenges for those exciting STO applications are still remaining, including optimizing the operating condition, tuning the frequency, narrowing the linewidth and improving the output power.

In this thesis work, the spin transfer torque induced oscillation is experimentally studied in MgO barrier based magnetic tunnel junctions (MTJs) with focus on the improvement of the key performances of the STO. The power angular dependence of spin torque oscillation is experimentally studied in dual MgO barrier MTJs based on the understanding of the relation between the MR and oscillation output power. It is proved that the STO electrical power increases with the polarizer canting angle. Meanwhile, the results also reveal a solution for extending the oscillation operating condition. Furthermore, the MTJ based STO device with a built-in hard axis polarizer is designed and studied. This design provides an external-field-free STO with high power, low critical current and extended operation range of the driving current for the first time. Additionally, two oscillation modes in the dual MgO barrier MTJs are observed and

investigated. It is found from the field-dependent power spectra that the extra oscillation mode may come from the weakly-pinned top reference layer. A single-shot time-domain measurement to characterize the switching time of each switch under different voltages for MTJs in the nanosecond precessional regime was carried out too.

# Contents

# List of Tables

# List of Figures

# Chapter 1. Introduction

In this dissertation, the spin transfer torque induced oscillation and switching are studied in MgO barrier based high magnetoresistance magnetic tunnel junction. So, in this chapter, the following concepts are introduced and discussed step by step. First, the mechanism, device structures and applications of the giant magnetoresistance (GMR) and tunneling magnetoresistance (TMR) are briefly reviewed because the ferromagnetic/ nonmagnetic/ ferromagnetic sandwich structured GMR spin valve and the magnetic tunneling junction (TMJ) are the widely studied devices for the spin transport electronics (spintronics). In section 2, one of the most popular topics of spintronics in the past decade, spin transfer torque, is reviewed. Additional to fundamental studies, the advanced nanometer fabrication and high frequency characterization technologies trigger intensive development of the spin transfer torque induced magnetization switching which leads to a promising application for the high spend, non-volatile random access memory. Furthermore, in section 3, the spin transfer torque induced magnetization oscillation is reviewed by focusing on (1) understanding the oscillation operation condition and device design, (2) understanding the tuning factors for the oscillation key metrics: frequency, linewidth and output power. To improve these critical metrics is the motivation for this thesis work.

# 1.1 Magnetoresistance based nanometer scale device

### 1.1.1 Giant magnetoresistance effect and spin valve device

The giant magnetoresistance (GMR) effect was first observed in Fe(001)/Cr(001) magnetic superlattices [1] and Fe/Cr/Fe sandwich structure [2] in 1988. In both cases, the ferromagnetic Fe layers are antiferromagnetically coupled at zero magnetic fields, while the Fe layers are aligned at the same direction by an external magnetic field. When the sensing current is applied in the film plan, the state of magnetic layers antiferromagnetically coupled with each other gives high resistance and the state of magnetic layers being parallel to each other gives low resistance, shown in Figure 1-1. The GMR ratio is defined as

$$GMR\ \% = \frac{R_{AF} - R_F}{R_F} \times 100\ \% \qquad \text{Eq. 1-1}$$

where the $R_{AF}$ is the resistance when the magnetic layers are antiferromagnetic coupled and the $R_F$ is the resistance when the magnetic layers are ferromagnetic aligned by the external magnetic field. By this definition, the GMR ratio was observed as 85% for the Fe(001)/Cr(001) magnetic superlattices and 1.5% for the Fe/Cr/Fe sandwich structure. The mechanism of the GMR effect can be explained by the two spin channel model in the ferromagnetic metal proposed by Mott in 1936 [3]. Figure 1-2 shows a schematic picture to describe the different resistance in the ferromagnetic/non-magnetic metal multilayer system based on two spin channel model. The contact pads are located at both sides to have the current flowing in the plane of the layers. When the electrons travel in the metal layers, the spin of the electrons can maintain their polarity, up or down, for certain length.

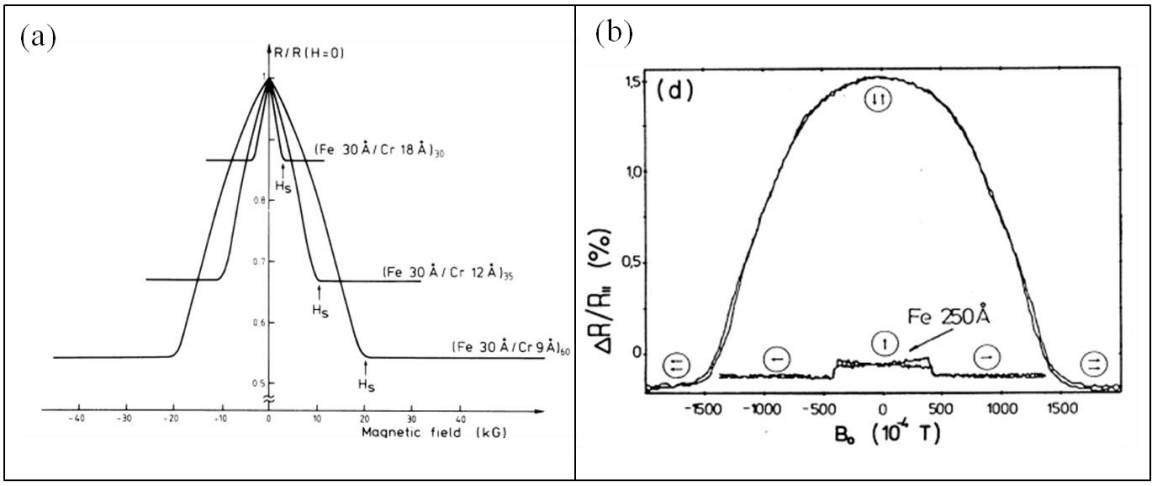


Figure 1-1 Giant magnetoresistance effect first observed in (a) Fe(001)/Cr(001) magnetic superlattices [1] and (b) Fe/Cr/Fe sandwich structure with antiferromagnetic interlayer exchange [2].

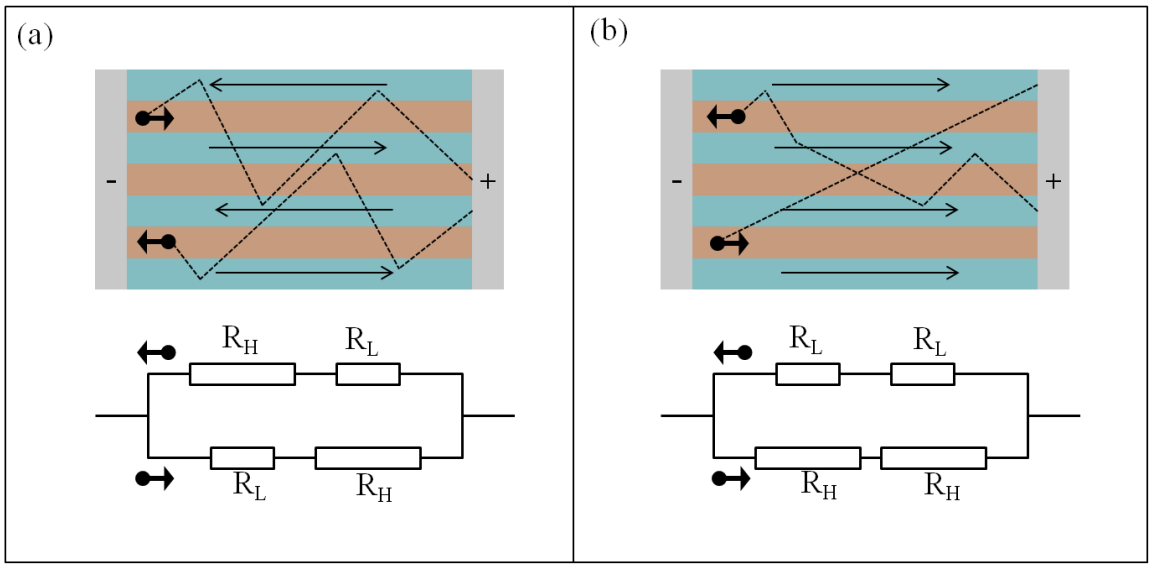


Figure 1-2 Schematic drawing of GMR two spin channel model for (a) anti-parallel magnetic layers and (b) parallel magnetic layers.

So the electrons can be considered as traveling through the layers in two channels, one for spin up electrons and another for spin down electrons. And the total resistance can be considered as two parallel connected resistors for two spin channels. When the electrons travel through the ferromagnetic material, the spin scattering depends on the angle between the spin momentum and local magnetization. The scattering between free electrons and local magnetization is weak when spin of the electrons is parallel to the local magnetization. And, in this case, the resistance is lower compared to the anti-parallel case.

Figure 1-2 (a) shows antiferromagnetic coupled ferromagnetic layers (layers with arrows indicating the direction of magnetization) which are separated by non-magnetic metal layers (layers without arrows). In this case, spin up electrons (bold arrow pointing left) experience both parallel and anti-parallel local magnetization. The resistance of the spin up channel can be written as $R_H + R_L$ where the $R_H$ and $R_L$ represent the high and low resistance states, respectively. The spin down channel shows the same resistance for the spin down electrons (bold arrow pointing right) traveling in the antiferromagnetic layers. So the total resistance is $R_{AF} = (R_H + R_L)/2$ for the antiferromagnetic coupled superlattices or sandwich structure. Figure 1-2 (b) shows the parallel aligned ferromagnetic layers (layers with arrows pointing at the same direction) separated by non-magnetic metal layers as well. In this case, spin up electrons are anti-parallel to all the local magnetization. So the resistance for spin up channel is $(R_H + R_H)$ while the resistance for spin down channel is $(R_L + R_L)$. Total resistance can be calculated as $R_F = 2 \times (R_H \times R_L)/(R_H + R_L)$ for the ferromagnetic aligned case. Based on Eq. 1-1 the GMR can be written as

$$GMR\ \% = \frac{(R_H - R_L)^2}{2 \times (R_H + R_L)} \times 100\% \ > 0 \qquad \text{Eq. 1-2}$$

The two spin channel model and Eq. 1-2 can also be used as a simple way to describe the GMR effect with the sensing current perpendicular to plane (CPP), shown in Figure 1-3 (a). In this CPP GMR, the spin up and spin down electrons are forced to travel perpendicular to the magnetic layers while, in the current in plane GMR (CIP GMR), the electrons only moves between magnetic layers due to electron motion under Pauli exclusion principle and thermal fluctuation. The MR ratio of the CPP GMR was predicted to be higher than the CIP GMR [4] and measured from a Co/Ag magnetic

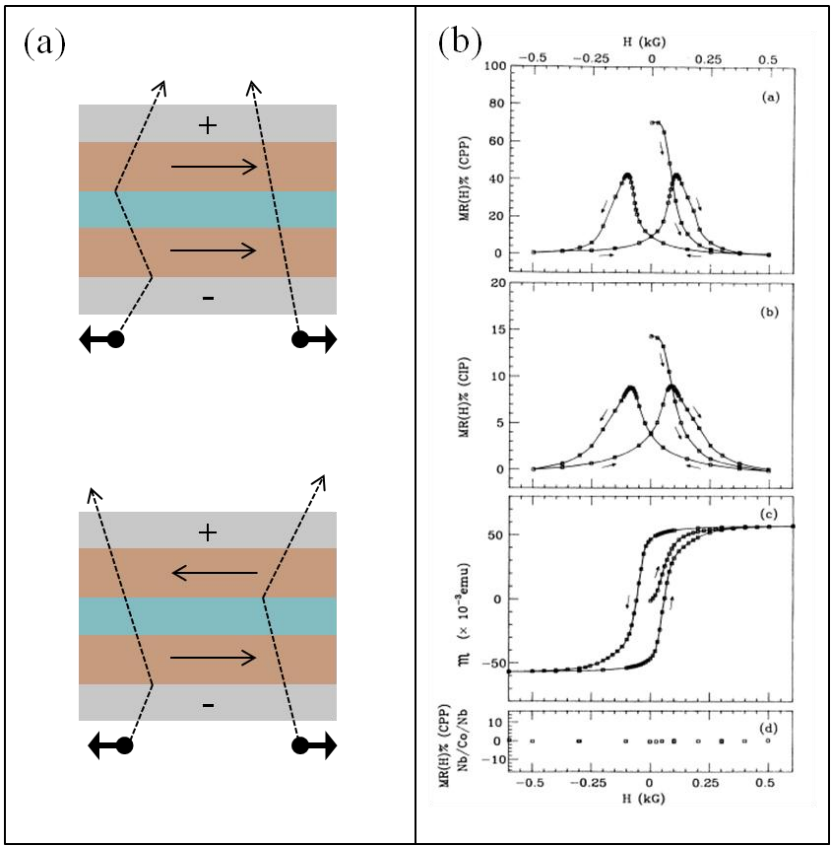


Figure 1-3 (a) Schematic drawing of the CPP GMR (b) the first giant magnetoresistance effect measured by current perpendicular to plane [5].

superlattices showing more than three times higher MR ratio measured by CIP technique from the same sample [5], as shown in Figure 1-3 (b). The CPP GMR can also be measured in the sandwich structure, which has been a basic building block for various fundamental studies such as the spin transfer torque induced magnetization switching and oscillation which will be introduced in section 2 and 3 of this chapter.

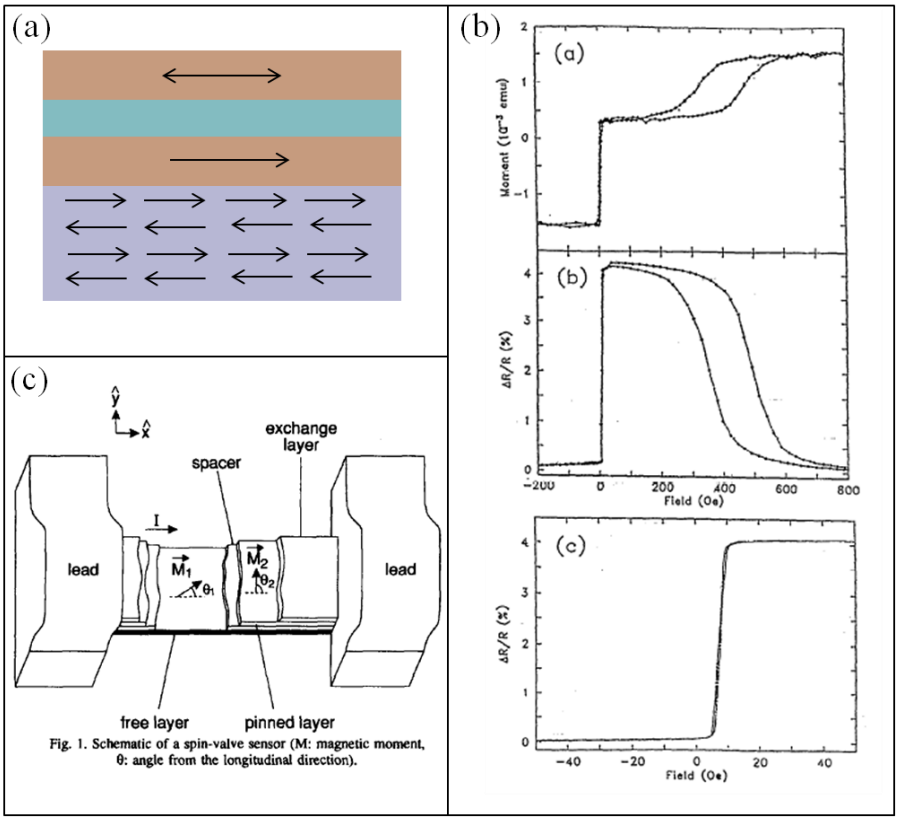


Figure 1-4 (a) Schematic drawing of the SV-GMR (b) signal field response of the SV-GMR[6] (c) HHD recording head using SV-GMR as reader sensor [7].

Figure 1-4 (a) shows the schematic drawing of the concept of GMR spin valve (GMR-SV), which was first developed in NiFe/Cu/NiFe GMR sandwich structure with the FeMn antiferromagnetic layer next to one of the NiFe layers [6, 8]. So the magnetization of this NiFe layer was constrained by the exchange anisotropy through the coupling to the

FeMn antiferromagnetic layer, and this NiFe magnetic layer can be defined as pinned layer. The NiFe magnetic layer on the other side of the metal spacer is considered as the free layer because the magnetization of this layer can be rotated under small applied magnetic field as shown in Figure 1-4 (b) [6]. This GMR-SV structure provides a direct and quantitative measurement of the dependence between the resistance and the relative rotation of the free layer magnetization to the pinned layer magnetization. The GMR effect and the spin valve structure directly led to a technological application as a sensitive magnetic field sensor with low saturation free layer [7, 9-12]. Figure 1-4 (c) shows the SV-GMR used as the reader of the recording head in the hard disk drive (HDD) [7, 9].

### 1.1.2 Tunneling magnetoresistance and magnetic tunnel junction device

Based on the studies on spin dependent tunneling by Meservey and Tedrow [13], the tunneling resistance between two ferromagnetic films was first reported by Julliere in 1975 [14]. The model of tunneling conductance between ferromagnetic layers was also proposed by Julliere. A schematic drawing is shown in Figure 1-5 (a) and (b) for magnetic layers parallel and anti-parallel states respectively. In Julliere's model, the tunneling probability is proportional to the product of the available electron states on one side of the barrier and the empty state at the other side of the barrier. By assuming that the electrons tunnels without spin flip, the spin up and spin down can be considered as two independent channels and conductance is the sum of the conductance of two spin channels. In the parallel case, shown in Figure 1-5 (a), the spin up (red arrows) is the majority for both magnetic electrodes while the spin down (blue arrows) is the minority.

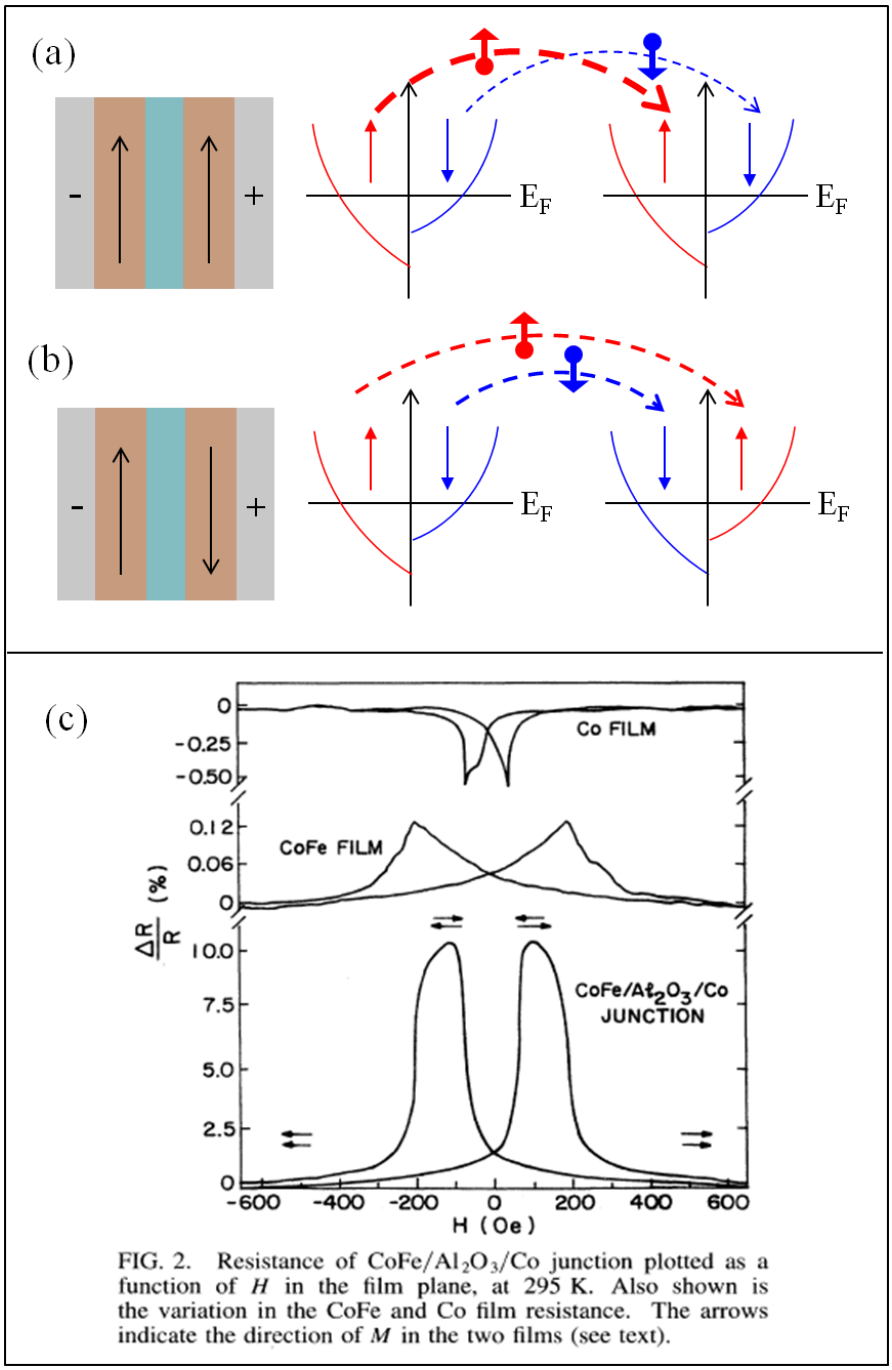


FIG. 2. Resistance of CoFe/$Al_2O_3$/Co junction plotted as a function of $H$ in the film plane, at 295 K. Also shown is the variation in the CoFe and Co film resistance. The arrows indicate the direction of $M$ in the two films (see text).

Figure 1-5 Schematic drawing of the electron tunneling in MTJ with two magnetic layers in (a) parallel and (b) anti-parallel state. (c) Demonstration of the TMR effect in an $Al_2O_3$ based MTJ at room temperature [15].

So the conductance for the parallel case is

$$G_P = DOS_{maj,L} \times DOS_{maj,R} + DOS_{min,L} \times DOS_{min,R} \quad \text{Eq. 1-3}$$

where the $DOS_{maj,L}$ and $DOS_{maj,R}$ represent the density of state (DOS) for majority spin of magnetic layers on the left and right shown in Figure 1-5 (a) and the $DOS_{min,L}$ and $DOS_{min,R}$ are for the minority spin. In this parallel state, the spin up is the majority for both layers, which contributes to the conductance more as shown the red thick dash line in Figure 1-5 (a). The spin down channel, on the other hand, has less contribution to the conductance shown as the blue thin dash line. For the anti-parallel case, shown in Figure 1-5 (b), the spin up is the majority for one of the magnetic layer but the minority for another, as well as the spin down. So the conductance for the anti-parallel case is

$$G_{AP} = DOS_{maj,L} \times DOS_{min,R} + DOS_{min,L} \times DOS_{maj,R} \quad \text{Eq. 1-4}$$

In the magnetic layer, the DOS difference between the majority and minority is defined as spin polarization ratio:

$$P = \frac{DOS_{maj} - DOS_{min}}{DOS_{maj} + DOS_{min}} \quad \text{Eq. 1-5}$$

which is the important parameter for the magnetic tunneling junction. So the conductance for both parallel and anti-parallel states can be rewritten as:

$$G_P = \frac{1+P_L}{2} \times \frac{1+P_R}{2} + \frac{1-P_L}{2} \times \frac{1-P_R}{2}$$
$$G_{AP} = \frac{1+P_L}{2} \times \frac{1-P_R}{2} + \frac{1-P_L}{2} \times \frac{1+P_R}{2} \quad \text{Eq. 1-6}$$

where the $P_L$ and $P_R$ represent the spin polarization ratios for the magnetic layers on the left and right in Figure 1-5. So the tunneling magnetoresistance (TMR) can be written as:

$$TMR = \frac{R_{AP} - R_P}{R_P} = \frac{G_P - G_{AP}}{G_{AP}} = \frac{2 \times P_L \times P_R}{1 - P_L \times P_R} \times 100\% \quad \text{Eq. 1-7}$$

The Julliere's model and Eq. 1-7 have been widely used to explain the TMR effect in MTJs with the amorphous tunneling barrier which is considered as single energy barrier. The TMR from the amorphous $Al_2O_3$ barrier based MTJ was reported by two groups, giving 11.8% [15] , as shown in Figure 1-5 (c), and 20% [16] magnetoresistance ratios at room temperature. The highest TMR ratio from amorphous $Al_2O_3$ barrier based MTJ was measured as 70% with CoFeB magnetic electrodes at room temperature [17].

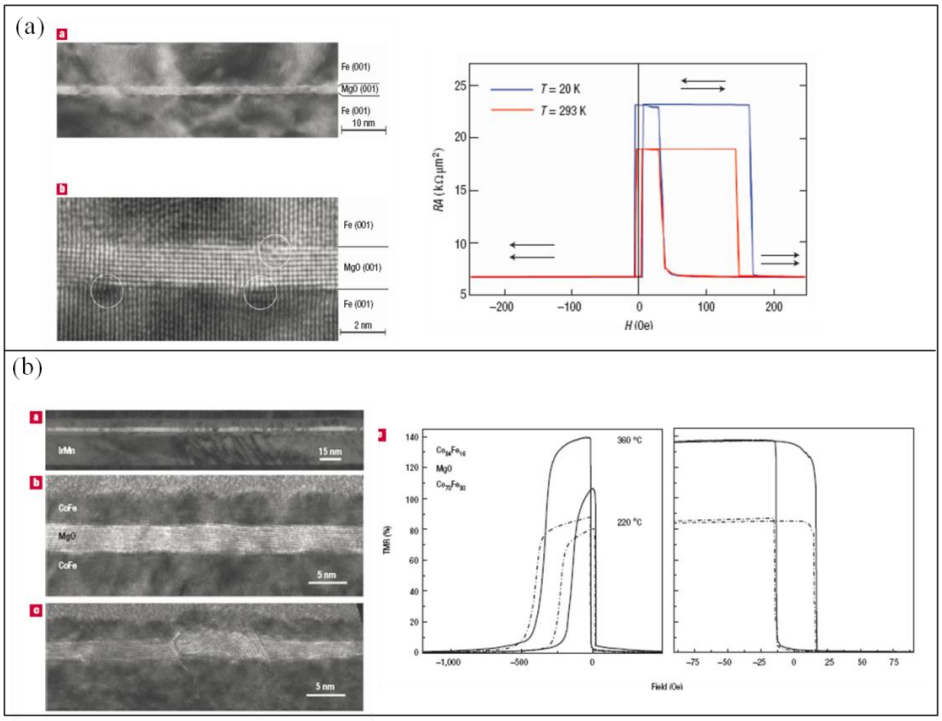


Figure 1-6 MgO (100) tunneling barrier based MTJ with more than 200% TMR ratio developed by using (a) molecular beam epitaxy [18] and (b) magnetron supttering with a post thermal anneling [19].

In 2004, TMR ratio was reported more than 200% from (100) oriented MgO tunneling barrier with (100) oriented Fe magnetic electrodes prepared by molecular beam epitaxy [18] shown in Figure 1-6 (a), and with (100) oriented CoFe magnetic electrodes

grown by magnetron sputtering along with a post thermal annealing [19], shown in Figure 1-6 (b). The high TMR ratio in the epitaxial Fe/MgO/Fe (100) MTJ was first calculated and predicted by Butler el. al [20] and Mathon el. al [21] in 2001. The mechanism for the high TMR in the epitaxial Fe/MgO/Fe (100) MTJ is called the symmetry filtering effect [22]. Based on the calculation, the conductance of the epitaxial tunneling junction is determined by the symmetry of the Block states in the magnetic electrodes and the evanescent states in the barrier, as well as the decay rate of the states with difference symmetry in the barrier. For epitaxial Fe (100), the Block states along the (100) direction for majority spin and minority spin are shown in Figure 1-7 (a). In majority spin channel, the state with $\Delta_1$ symmetry mainly contributes to the conductivity. Because it is around the Fermi level and effectively coupled to evanescent $\Delta_1$ symmetry state in epitaxial MgO (100) with relevantly low decay rate. For minority spin channel, the state with $\Delta_5$ symmetry, instead of $\Delta_1$, is available around the Fermi level with higher decay rate in MgO barrier compared with $\Delta_1$ symmetry state. When both Fe (100) electrodes are parallel to each other, the states with $\Delta_1$ symmetry are available for the majority spin channel of both electrodes cross the MgO barrier, and the conductivity is high. However, in the anti-parallel case, the tunneling probability of the electrons with $\Delta_1$ symmetry is much lower because the state with $\Delta_1$ symmetry is not available for the counter electrode. This results a lower conductivity. The significant differences of the Block state with $\Delta_1$ symmetry near Fermi level and the decay rate in the barrier between majority and minority spin channels result high TMR ratio of the epitaxial Fe/MgO/Fe (100) MTJ.

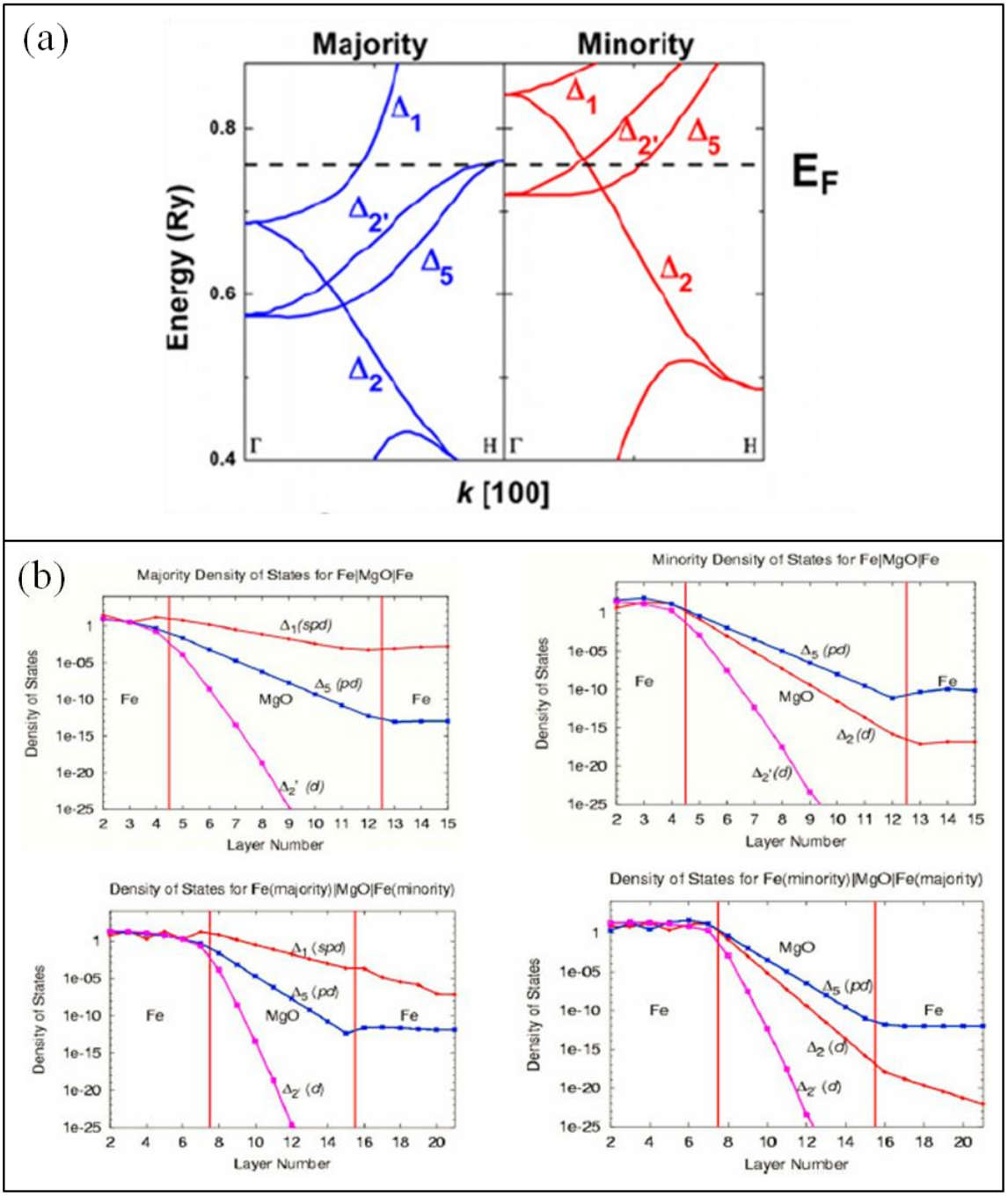


Figure 1-7 (a) The band structure of bcc Fe in [1 0 0] direction [23]. (b) Tunnelling density of states for majority spin and minority spin [22].

The development of the MTJ triggered an increase of the data storage areal density to 100 Gb/in$^2$ and beyond with the high TMR MgO barrier based MTJ [24-27]. Figure 1-8 (a) shows the TEM image of the reader using MTJ as its basic field sensing unit. The reader sensor stack also includes the synthetic anti-ferromagnetic structure and the anti-ferromagnetic pinning layer similar to the GMR spin valve stack. The MgO barrier based MTJ is currently used as the reader of the recording head in the hard disk drive reaching 1 Tb/in$^2$ areal density. The magnetic random access memory (MRAM) is another successful application, commercialized based on the development of the MTJ. The concept of the MRAM started in the 1950s and was known as magnetic core memories [28-29]. With the development of the magnetic thin film technology, MRAM was built using the anisotropic magnetoresistance (AMR) and GMR device as the storage units [30-34]. It is not until the development of MTJ that the MRAM was commercialized as a non-volatile memory due to its higher resistance and higher magnetoresistance ratio [35-40]. Figure 1-8 (b) gives the schematic drawing of MRAM's basic write and read unit using MTJ containing a magnetic free layer and a pinned layer. The magnetic free layer, as the information storage layer, can be switched or written by the magnetic field supplied by two word lines at the top and bottom of the MTJ. Two current lines supply the reading back the resistance by passing the sensing current perpendicular to the MTJ stack. MRAM with this type of writing mechanism is known as the toggle MRAM. The spin transfer torque RAM (STT-RAM) is a newly developed MRAM which has a different free layer writing mechanism based on spin transfer torque introduced in the next section.

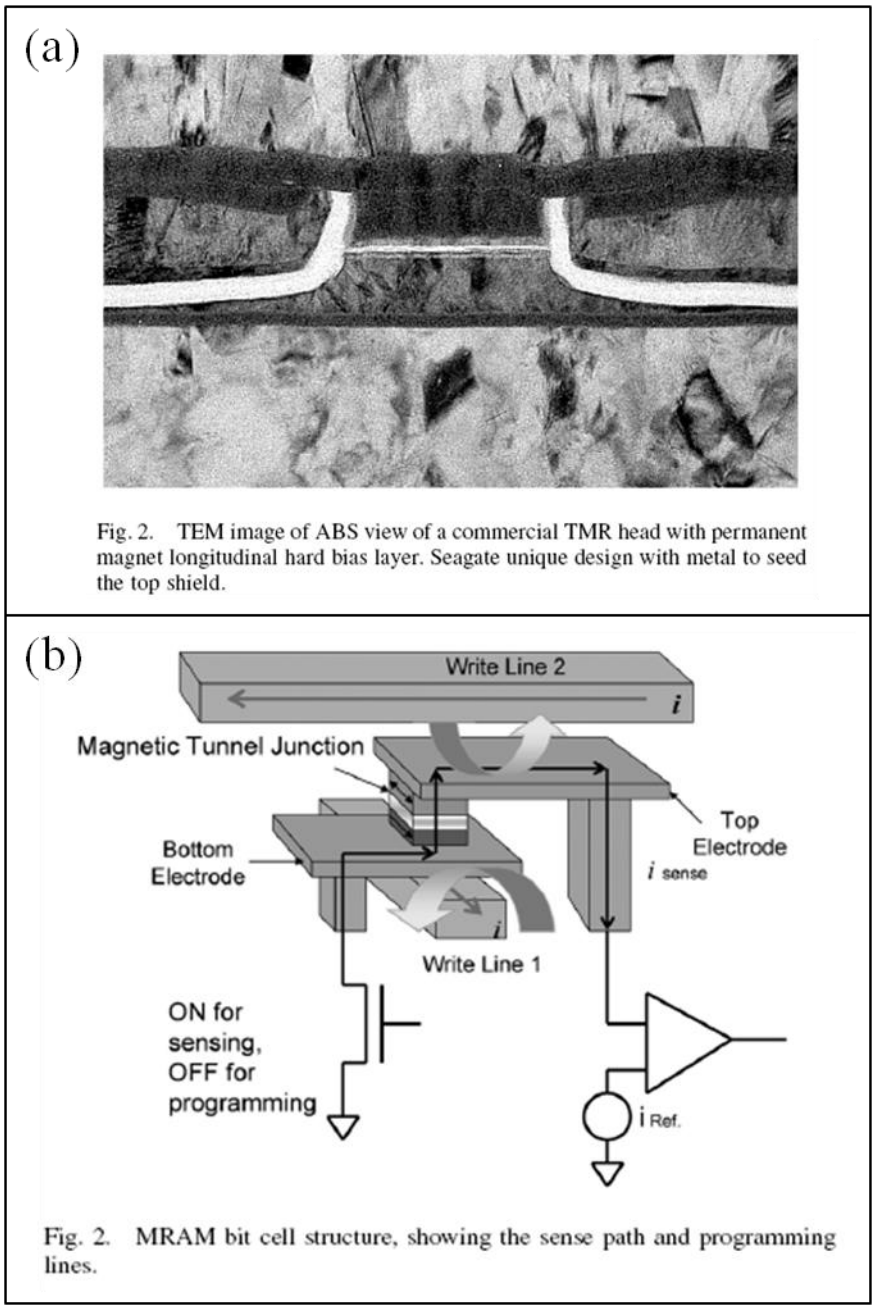


Figure 1-8 (a) TMR reader in the hard disk drive [27]. (b) MRAM using MTJ as the bit cell [39].

## 1.2 Spin transfer torque

Spin transfer torque (STT) in case of ferromagnetic/non-magnetic/ferromagnetic system was first studied by Slonczewski [41] and Berger [42] in 1996. The theoretical calculation suggested that the magnetizations of the ferromagnetic layers can be excited and switched due to the torque transferred from the counter ferromagnetic electrode through the spin polarized current. The magnetization excitation was observed first in Co/Cu superlattices film with a nanometer size point contact injecting dc current in 1998 [43]. In the following year, the switching of the ferromagnetic layer by dc current was experimentally measured in Co/Cu/Co sandwich structure [44] and in tunneling junction with epitaxial manganite thin films [45]. Due to its promising application for the MRAM, the STT switching was studied based on various GMR and MTJ devices, including multilayer GMR devices with different ferromagnetic material [46], sandwich structure GMR with perpendicular anisotropy [47-48], MTJs with amorphous AlOx barrier [49-50] and MgO barrier based high TMR MTJs with in-plane [51-52] and perpendicular anisotropy [53]. Figure 1-9 (a) and (b) show examples of magnetic field and DC current driven magnetic free layer switching measured from the same MgO based MTJ device. Different from the conventional field driven magnetoresistance hysteresis loop, shown in Figure 1-9 (a), the current driven magnetoresistance hysteresis loop is measured under sweeping DC current through the MTJ stack as shown in Figure 1-9 (b).

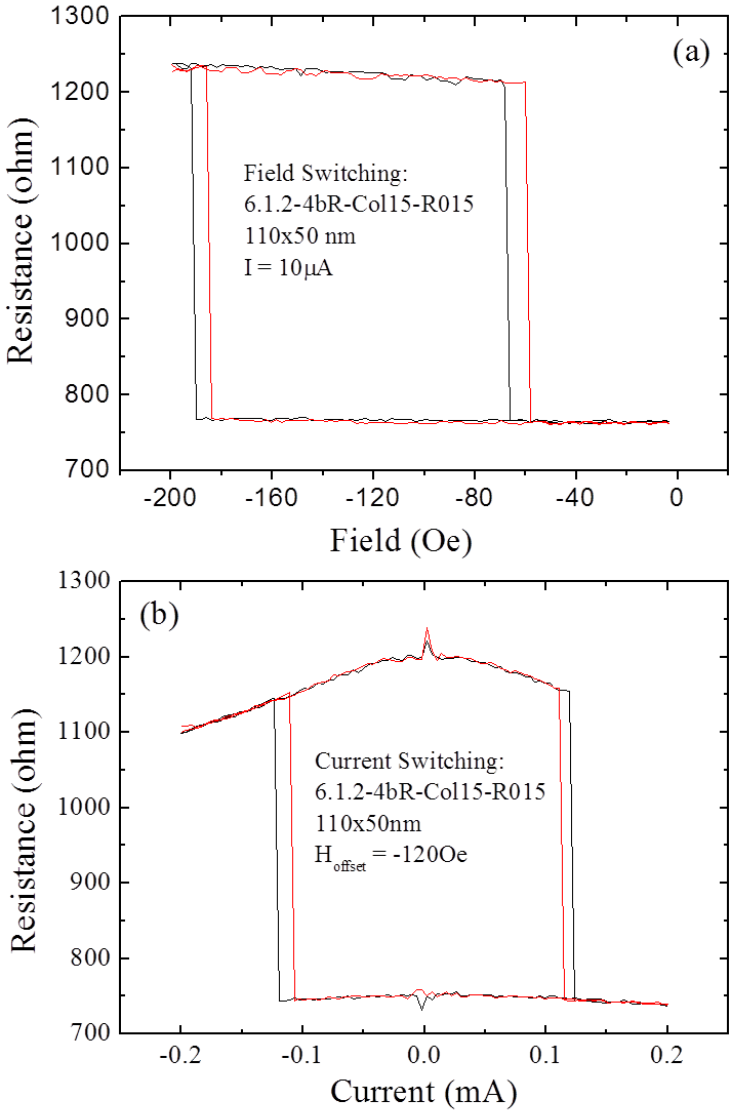


Figure 1-9 (a) MTJ free layer switched by the external magnetic field. (b) MTJ free layer switched by the DC current perpendicular to the sandwich structured magnetic thin films.

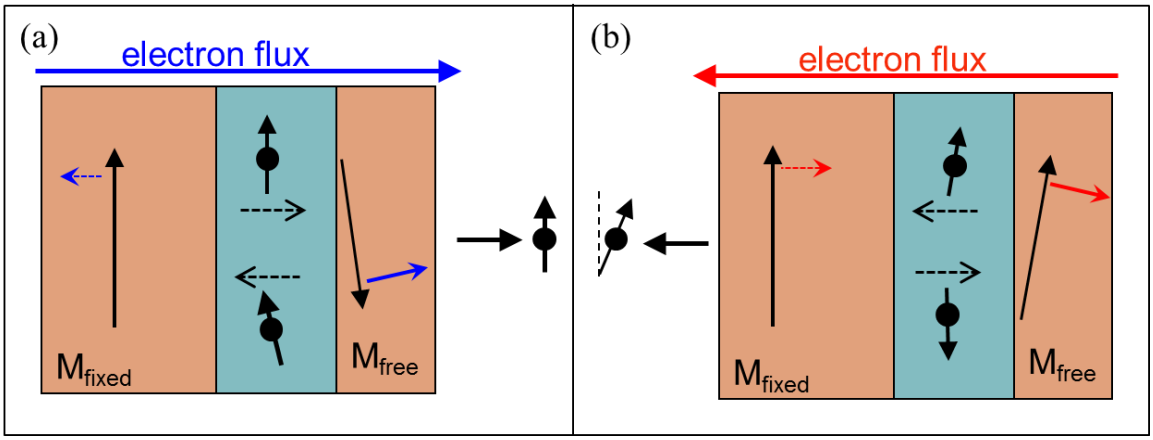


Figure 1-10 Spin transfer torque in ferromagnetic/non-magnetic/ferromagnetic sandwich structure with the electron flux (a) from fixed layer to free layer (b) from free layer to fixed layer.

Figure 1-10 generally describes the magnetization switching in the ferromagnetic/non-magnetic/ferromagnetic sandwich structure including the GMR-SV and MTJ. Here, it is assumed that one ferromagnetic layer is stiffer than another layer, as fixed layer and free layer respectively. When the electron flux flows from the fixed layer to the free layer, shown in Figure 1-10 (a), it is polarized by the fixed layer. The majority spin of the polarized electron flux follows the same direction of the fixed layer magnetization. When the polarized electron flux travels to the free layer, it tends to align with the local moment of the free layer magnetization and creates a torque on free layer. Meanwhile, the reflected electrons, from free layer to the fixed layer, carrier the moment opposite to the free layer magnetization and generate a torque on the fixed layer. Since the fixed layer is stiffer, the free layer will be switched and aligned along the fixed layer magnetization direction when the current is large enough. So the electron flux from the fixed layer to the

free layer, defined as positive current, will align the free layer parallel to the fixed layer. When the electron flux travels from the free layer to the fixed layer, the torque on fixed layer tends to rotate the fixed layer towards the free layer direction and the reflected electron into the free layer pulls the free layer away from the fixed layer, as shown in Figure 1-10 (b). So the negative current, electron traveling from the free layer to the fixed layer, will switch the free layer anti-parallel to the fixed layer. The free layer magnetization precession and switching can be described by the Landau-Lifshitz-Gilbert (LLG) equation with spin transfer torque terms [41, 54-56]:

$$\frac{d\vec{m}}{dt} = -\gamma\vec{m} \times \vec{H}_{eff} + \alpha\vec{m} \times \frac{d\vec{m}}{dt} - a_j\vec{m} \times (\vec{m} \times \vec{p}) - b_j(\vec{m} \times \vec{p}) \quad \text{Eq. 1-8}$$

In this equation, the $\vec{m}$ is the unit vector of the free layer's magnetization direction. On the right hand side of the equation, the first term is the precession term which keeps the magnetization precession around the effective field ($\vec{H}_{eff}$). Here, $\gamma$ is the gyromagnetic ratio. The second term is the damping term which tends to align the free layer magnetization along the effective field. Here, $\alpha$ is the Gilbert damping constant. The third term is the STT term which describes the magnetization switching by the polarized current. In this STT term, the $\vec{p}$ is the unit vector representing the magnetization direction of the reference layer or fixed layer in Figure 1-10, and the $a_j = (\hbar\gamma JP)/(M_s t_{FL} e)$. So the magnitude of the STT on the free layer is proportional to current density J, the spin polarization ratio P of the reference layer and the sinusoidal of the angle between the free layer and reference layer magnetization. The fourth term is the field like STT [54] or perpendicular STT term as $b_j = \xi a_j$ [56] which follows or opposes to the precession term.

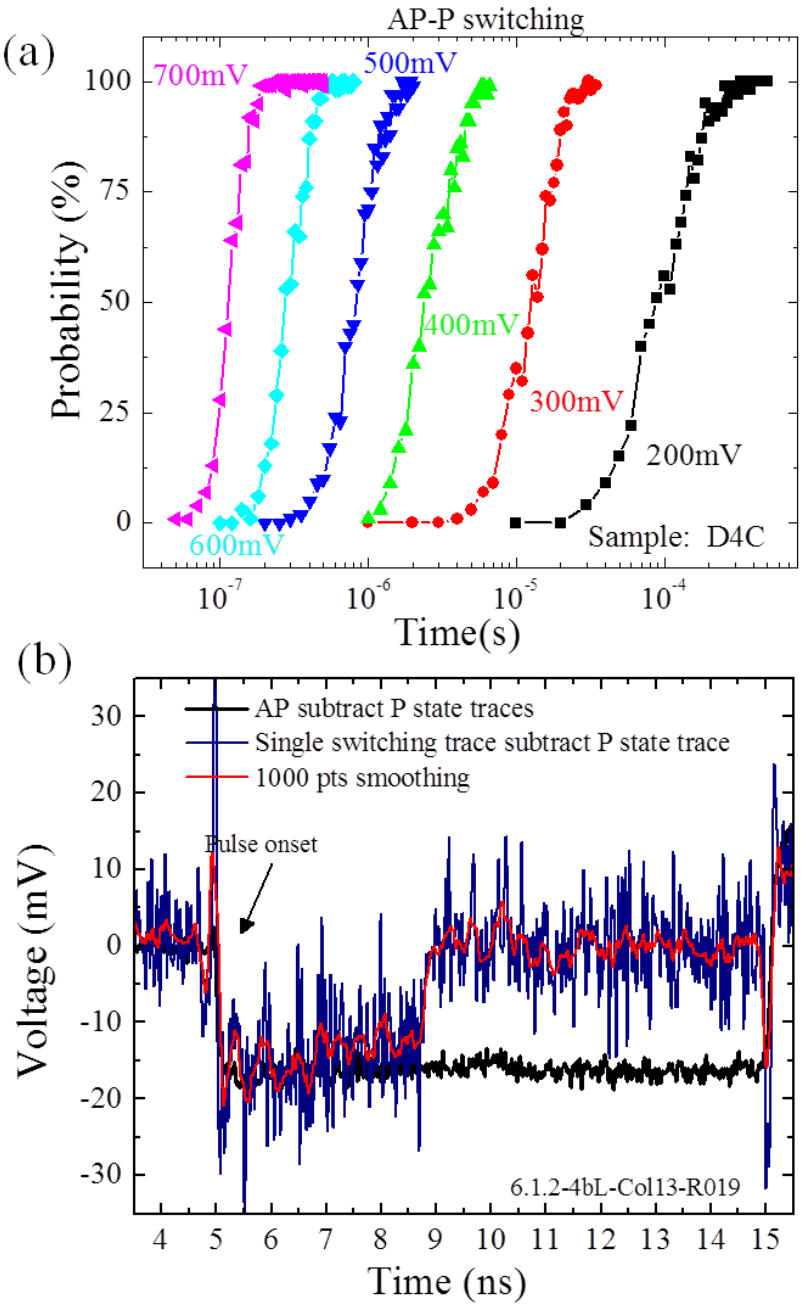


Figure 1-11 (a) Switching probability increase with time (pulse width) at different applied voltage. (b) The voltage response of real time free layer switching.

This perpendicular STT term $b_j$ is suggested to be very small in the metallic spin valve [57-59]. The STT $b_j$ term was measured and calculated in the magnetic tunnel junction based on various approaches which suggest that it starts to affect the switching on higher bias [56, 60-62].

Based on the fundamental studies on the STT switching [45, 63-65], intensive research and development work has been carried out by focusing on the critical challenges of STT-RAM application, such as the critical switching current density and switching speed. These research and development efforts include (1) material engineering which mainly focuses on the perpendicular anisotropy magnetic free layer development [47-48, 53, 66-69], (2) novel device designs such as dual sandwich structure [70-72], composite free layer [73-76] and additional perpendicular polarizer [77-81], and (3) advanced device characterization techniques [61-62, 64, 82-84] which provide the opportunity for device design ranking and device physics understanding. Figure 1-11 (a) gives an example of the switching probability measurement result from the MgO based MTJ with perpendicular CoFeB free layer and reference layer. At one applied voltage level, each data points represent the percentage of the completed switching from AP state to P state within a specific voltage pulse width. This statistic based measurement is widely used for STT switching study and STT RAM development. However, probability versus time curve doesn't represent the actual switching. Figure 1-11 (b) shows an example of a real time free layer switching measurement result. This measurement is based on the real time pulse response to the impedance change during the switching. The real time measurement provides more detail on the switching process [85-86]. Additional to the MTJ development for STT switching, the downstream COMS (Complementary metal–oxide–

semiconductor) integration and capability demonstration are very important. Figure 1-12 shows the first demonstration of the intergraded 4kbit 1-Transistor 1-MTJ STT-RAM [87] . The downstream STT-RAM integration and demonstration are more focused on metrics such as scalability, error rate and reliability [88-94]. In this dissertation, the spin transfer torque induced switching time distribution in the MgO based MTJ will be discussed in chapter 6.

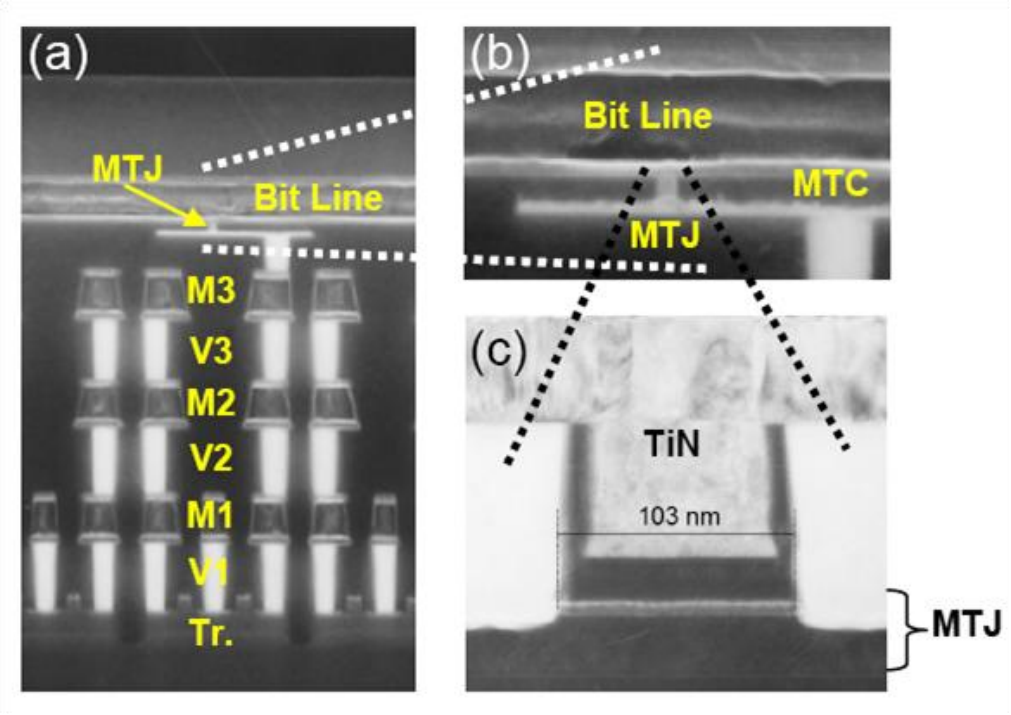


Figure 1-12 TEM image of the intergraded 1-Transistor 1-MTJ STT-RAM [87].

## 1.3 Spin torque oscillation

### 1.3.1 Spin torque oscillation

The studies of the spin transfer toque induced magnetic switching have drawn intensive attention because of the promising application for STT-RAM. However, based on the original theoretical prediction, the spin transfer torque is also able to drive the magnet into certain types of oscillation modes [41-42]. The traditional current-voltage (I-V) measurement provides indirect evidence of possible magnetic dynamic states induced by spin transfer torque in both multilayer GMR and sandwich structure GMR devices [43, 95-98]. Figure 1-13 (a) gives a typical example of the I-V measurement showing a sudden resistance change under large current where oscillatory magnetic states might be happening [95]. The direct evidence of the spin transfer torque induced magnetization oscillation in a Co/Cu/Co GMR sandwich structure was first report in 2003 [99], as shown in Figure 1-13 (b). The dynamic electrical signal was measured by the spectrum analyzer with high bandwidth circuit. The detail of the frequency domain measurement will be introduced in chapter 2. The frequency domain characterization has been commonly used for most of the spin transfer torque induced oscillation studies. Furthermore, the high frequency magnetization oscillation was directly observed by the oscilloscope as a time domain voltage signal due to the magnetoresistance change, shown in Figure 1-13 (c) [82]. The time domain measurement provides extra information related to time resolved frequency and amplitude fluctuation of the spin transfer torque induced oscillation [85, 100-103]. The detail of the time domain testing will be introduced in chapter 2 as well.

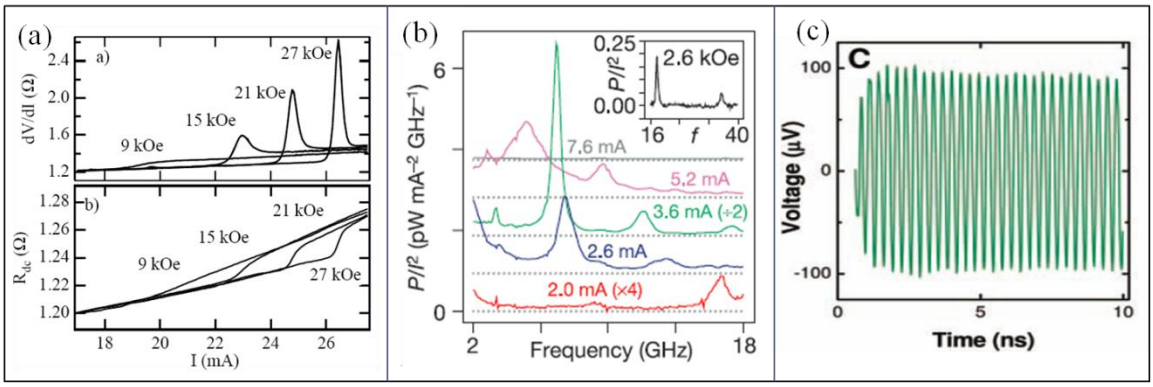


Figure 1-13 (a) Spin transfer toque stimulating magnetic dynamic states observed based on the resistance change under larege current and magnetic field [95]. (b) Directily electrical measurement of spin torque oscillation in frequency domain [99]. (c) Directily observation of the spin torque oscillation as a time domain voltage signal [82].

It is noticed that large magnetic fields and large dc currents were applied to generate the oscillation states of the magnetic free layer in those GMR devices shown in Figure 1-13. Based on the LLG equation with STT terms (Eq. 1-8), it is not surprised that magnetic field and dc current need to be tuned to have spin transfer torque minimizing the damping torque effect, by which the precessional states will be stabilized. In the conventional GMR or MTJ sandwich structure, it is assumed that (1) the free layer (FL) has an uniaxial anisotropy due to the ellipse shape, (2) the free layer is anti-parallel to the fixed layer (or pinned layer, PL), and (3) the electron flux passes the stack from fixed layer to free layer, shown in Figure 1-14 (a). In this case, the spin transfer torque tends to align the free layer with the fixed while the damping torque is pulling it back. The directions of the free layer, fixed layer, effective field, damping torque, precession torque and spin transfer toque are schematically drawn in Figure 1-14 (b). Ideally, the stable

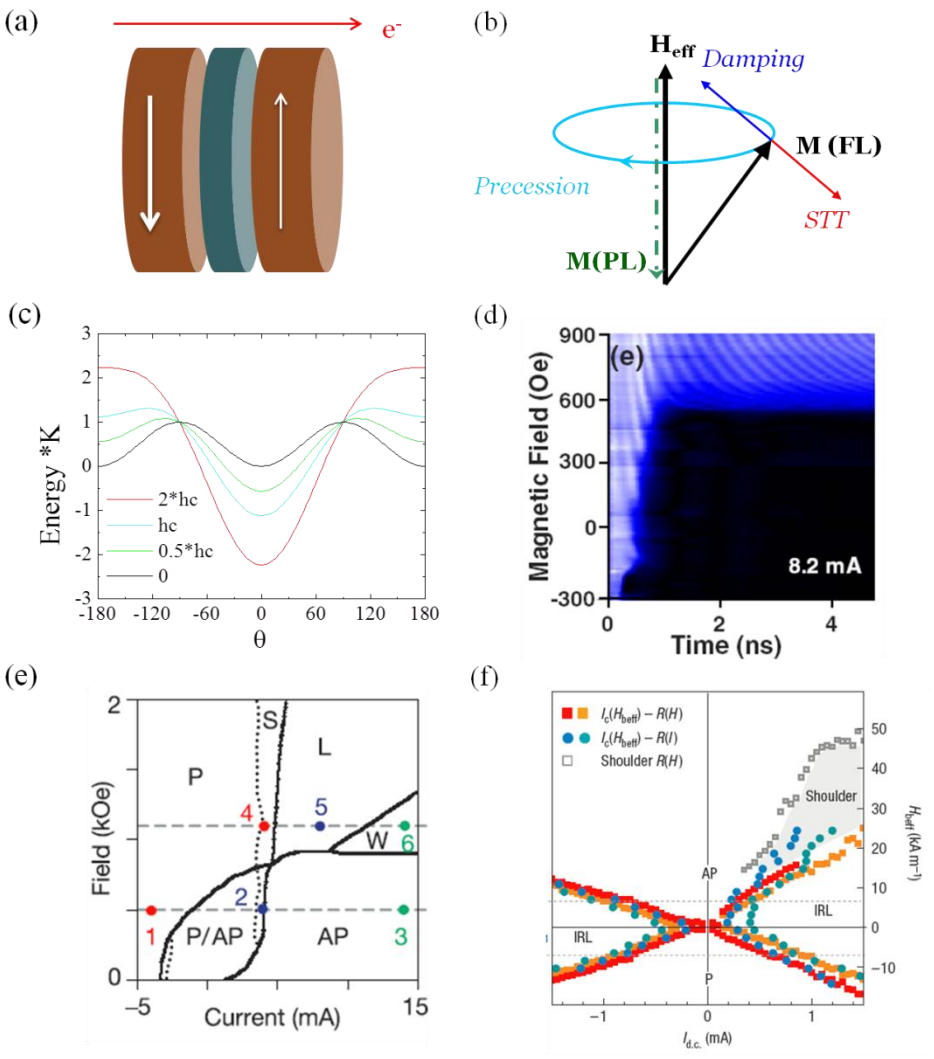


Figure 1-14 (a) Schematic showing electron flux flowing from fixed layer to free layer in typical magnetic sandwich structure. (b) Schematic drawing for the torques on the free layer. (c) Energy profile of the free layer with in-plane shape anasotropy and applied field along the easy aixs based on Stoner-Wohlfarth model (d) Free layer procession and switching under different magnetic field [85]. (e) The field-current phase diagram for free layer states in a conventional GMR device [99]. (f) The field-current phasie diangran for the free layer states in a conventional GMR device with an extra perpendicular polarizer [104].

precessional motion will be observed before the free layer switched to parallel state. However, the thermal fluctuation might be able to break the balance and bring the free layer to parallel or anti-parallel state. The reason for this is that the free layer has two energy minimum points due to the shape anisotropy, shown as the black curve in Figure 1-14 (c). One solution will be that using an external magnetic field to create only one energy minimum. With external fields applied along the easy axis, shown as the blue, green and red curves in Figure 1-14 (c), a global energy minimum is created and the energy well goes deeper. So the spin transfer torque can bring the free layer up from the lowest point (anti-parallel state) to higher energy states with a large dc current, where the stable oscillation states might exist. Meanwhile, the free layer can't be aligned with the fixed layer because the energy of the parallel state for free layer is much higher. Figure 1-14 (d) shows the experimental result of the free layer behavior under constant current and increased external fields [85]. The stable precession states are observed when the applied fields are greater than the coercivity, about 500 Oe in this case. A field-current phase diagram of the free layer's stable states was presented when the spin torque oscillation were first observed in frequency domain [99], shown in Figure 1-14 (e). The P and AP represent the stable parallel and anti-parallel states, respectively. The P/AP area is due to the hysteresis. When applied field is smaller than the coercivity, the small precessional states are reached before switching. When the applied field is larger than coercivity, the spin transfer torque can drive the free layer from small angle oscillation (S) to large angle oscillation (L) with increased current. It is noticed that there is no clear region in this phase diagram giving stable oscillation states at zero applied field. So, for potential application, it is critical to find an easy way to generate oscillation, especially to

avoid applying large external field. Based on the LLG equation with spin transfer torque term (Eq. 1-8), the polarized current actually can be tuned as a vector rather than just two polarity. The perpendicular polarizer, fixed layer with perpendicular anisotropy is proposed by simulation[105-106] and experimentally studied in a GMR device with an extra perpendicular polarizer [104], shown in Figure 1-14 (f). The field-current phase diagram shows the stable oscillation states exist around the area where external field is zero. In this dissertation, we'll discuss an alternative solution by tuning the in-plane polarizer direction in the MgO based MTJ device.

### 1.3.2 Key metrics: frequency, linewidth and power

The frequency of the spin torque oscillator is mainly determined by its ferromagnetic resonance (FMR) frequency and can be tuned by the external magnetic field and applied current. The FMR frequency can be described by the Kittel equation [107]:

$$f = \frac{\gamma}{2\pi}\sqrt{\left[H_x + \left(N_{yy} - N_{xx}\right) * 4\pi M_x\right] * \left[H_x + \left(N_{zz} - N_{xx}\right) * 4\pi M_x\right]} \qquad \text{Eq. 1-9}$$

Here, the magnetization is pointing at x axis and the precession angle is assumed to be small. $N_{xx}$, $N_{yy}$, and $N_{zz}$ are the demagnetizing factor. For a thin film with in-plane magnetization pointing along the x axis, the frequency can be writing as:

$$f = \frac{\gamma}{2\pi}\sqrt{H_x * \left(H_x + 4\pi M_x\right)} \qquad \text{Eq. 1-10}$$

by considering the out-of-plane demagnetizing factor close to 1 and the in-plane factors are small. Here, the x axis represents the in-plane magnetization direction which is also the direction of the external magnetic field. So, for the in-plane magnetization device, the oscillation frequency is mainly determined by the magnetization along oscillation axis under small magnetic field, and increases with the external magnetic field applied along

the same direction. For most of the in-plane magnetization spin torque oscillators, the devices are made as an ellipse to introduce shape anisotropy, which means $N_{yy} - N_{xx} > 0$ in Eq. 1-9. In this case, the FMR still can be observed without external field being applied. For a thin film with out-of-plane magnetization, the frequency can be written as:

$$f = \frac{\gamma}{2\pi} * (H_x - 4\pi M_x) \qquad \text{Eq. 1-11}$$

Here, the x axis points out-of-plane. And the magnetic field along the x axis $H_x$ could be the perpendicular anisotropy field and/or external magnetic field. So, in this case, the frequency also increases with the applied field. Figure 1-15 (a) shows the experimental and analytical calculation data of the oscillation frequency dependence on the applied field [108-109].

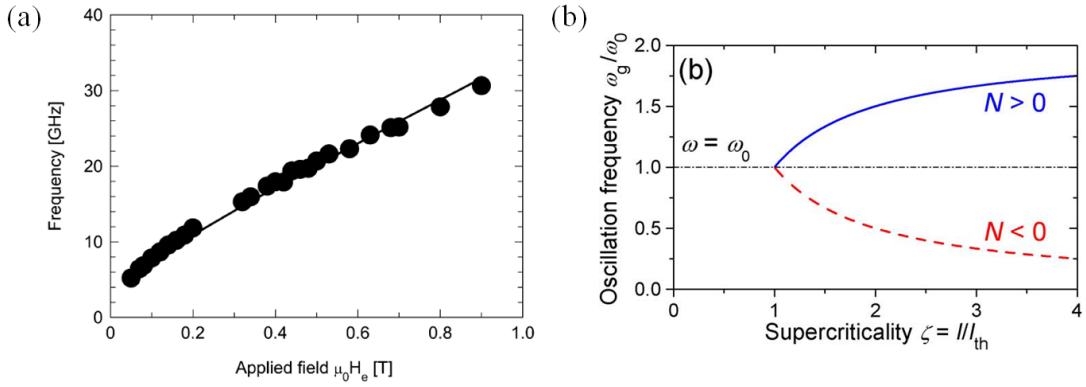


Figure 1-15 (a) Freuqnecy linearly increase with applied magnetic field [108-109]. (b) Freuqnecy blue shfit and red shift with increased current for perpendicular and in-plane magnetic free layer [110].

For both in-plane and out-of-plane oscillator, the frequency increases with the applied field. However, the frequency current dependence is very different. For the in-plane case, the precssion angle increases with the applied cuurent. So the magnetizaion projection

along the x direction is reduced and the frequency will drop based on Eq. 1-10. For the out-of-plane case, the oscillaiton angle also increases with the larger current which reduces $M_x$ . However, the total effective field is increased due to the reduced demagnetizing field and then frequecy increases. So the in-plane and out-of-plane oscilltor show frequency red shift and blue shift with an increased current, shown in Figure 1-15 (b) [110].

Spectral linewidth, as full width at half maximum (FWHM) of the power spectrum, is the key metric characterizing the quality of the oscillation. The linewidth of the spin torquen induced oscillation can be affected by several factors, such as temperature, applied current and external magnetic field. Figure 1-16 (a) shows the temperature dependence of the oscillation linewidth. The thermal fluctuation perturbs the trajectory of the free layer oscillation which leads to the phase and amplitude fluctuation [111-113]. The frequency fluctuation or hopping will also broaden the width significantly, especially the oscillation running under certain conditions where oscillation modes are switched

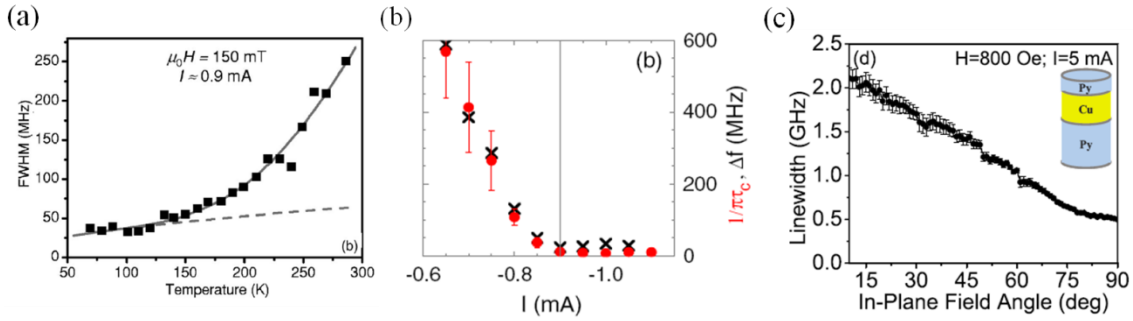


Figure 1-16 (a) Linewidth temperature dependence [111]. (b) Linewidth dc current dependence [100]. (c) Linewidth in-plane field angle dependence [114].

frequently [102]. Meanwhile, the temperature will also affect the magnetic properties, such as satuation magnetizaion. Figure 1-16 (b) shows that the linewidth linearly decreases with applied dc current. The FMR linewidth is also determined by the damping constant. Based on the LLG equeation with spin trasnfer torque terms (Eq. 1-8), the spin transfer torque reduces the damping when they are against each other. Since the spin transfer toque is tuned by the applied current, the linewidth can be written as [100, 115-116]:

$$\Delta f = \alpha * \frac{\gamma H_{eff}}{2\pi} - \frac{\sigma}{2\pi} * I \qquad \text{Eq. 1-12}$$

where, α is the damping constant and σ is related to spin torque efficiency. Eq. 1-12 is usually used to determine the transition from the FMR to the stable oscillation states [100, 115-116]. It is reported that the linewidth increases with the current after reaching the minimum points which could be due to the current heating, large angle shell shape oscillations or stochastic switching processes [113]. Figure 1-16 (c) shows the linewidth changes with the angle of the in-plane magnetic field. This is due to the more coherent oscillation at the angles close to the 90 degree [114]. In chapter 4 of this dissertation, we designed and demonstrated the low linewidth device having built-in 90 degree configuration.

Because the spin transfer torque oscillation is generated from a magnetoresistance sandwich structured device, and one the magnetic layer is oscillating. There are two outputs generated by it: (1) the AC magnetic field generated from the free magnetic layer and (2) the AC voltage signal due the MR change. Figure 1-17 shows several methods mainly to improve the AC voltage output of the spin torque oscillator. Since the AC voltage is determined by the MR change, the output power is significantly improved

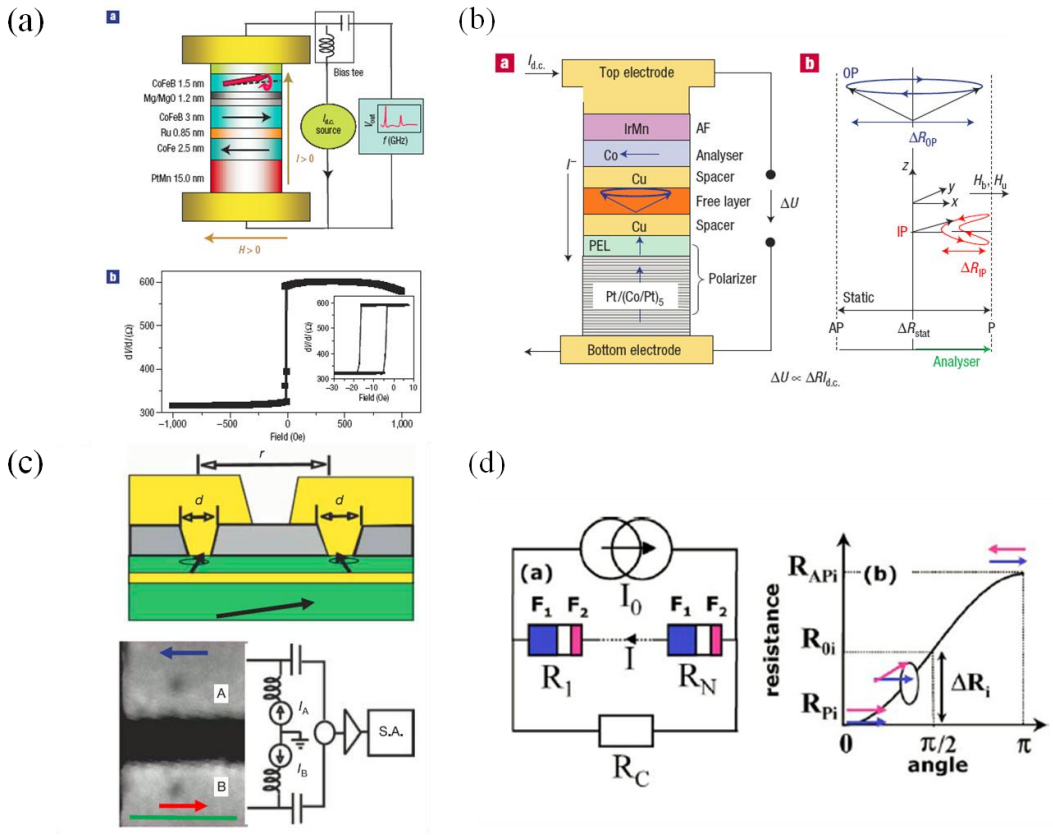


Figure 1-17 (a) High power output from MgO based MTJ spin torque oscillator due to high MR ratio [117]. (b) GMR-SV with an extra perpendicular polarizer giving higher power output due to large precession angel relative to the pinned analyzer layer [104]. (c) Enhanced power due to phase loking of two oscillators through spin-wave [118]. (d) phase locking through the ac current generated by the oscillators [119].

by high MR ration MTJ with MgO barrier [117, 120], shown in Figure 1-17 (a). Figure 1-17 (b) shows the GMR-SV with an extra perpendicular polarizer which improves the power by having the free layer precession axis perpendicular to the MR reference layer and taking advantage of more MR changes during the free layer oscillation [104]. This structure can also improve the AC magnetic field output and was first proposed and

suggested to be used as the writer in the magnetic recording heads [106, 121]. However, it could be very difficult to develop this structure in the MgO based MTJ due to the lattice matching discussed in the introduction of the MTJ. Phasing locking two oscillators through the spin-wave propagating in the continuous magnetic free layer gives significant output power gain [118, 122], shown in Figure 1-17 (c). However, this design does have critical requirements for material engineering, such as low damping and perpendicular free layer. Meanwhile the phase difference is very sensitive to the distance between the oscillators [123], which increases the challenge of device design and fabrication. An alternative phase locking solution was proposed, shown in Figure 1-17 (d). It is experimentally and theoretically proved that a strong external AC voltage source, with a frequency close to the oscillator frequency, can reduce the linewidth and improve the power [124-125]. So it was proposed and simulated that to have several oscillators being electrically connected and phase locked through the AC voltage generated by all oscillators [119, 126]. However, there are still several practical challenges, especially the material engineering and device fabrication. In this dissertation, we discussed and proposed an easier method to improve the AC voltage output in the MgO based MTJ in chapter 3 and chapter 4.

### 1.3.3 Potential applications

Several applications have been suggested based on the oscillation property of the MR devices. Figure 1-18 (a) shows the idea that using the spin torque oscillator as an AC magnetic field generator for the writer of the magnetic recording head, known as microwave assisted magnetic recording (MRAM) [121]. It is noticed that the structure of the oscillator is similar to the conventional reader structure, which potentially lower the

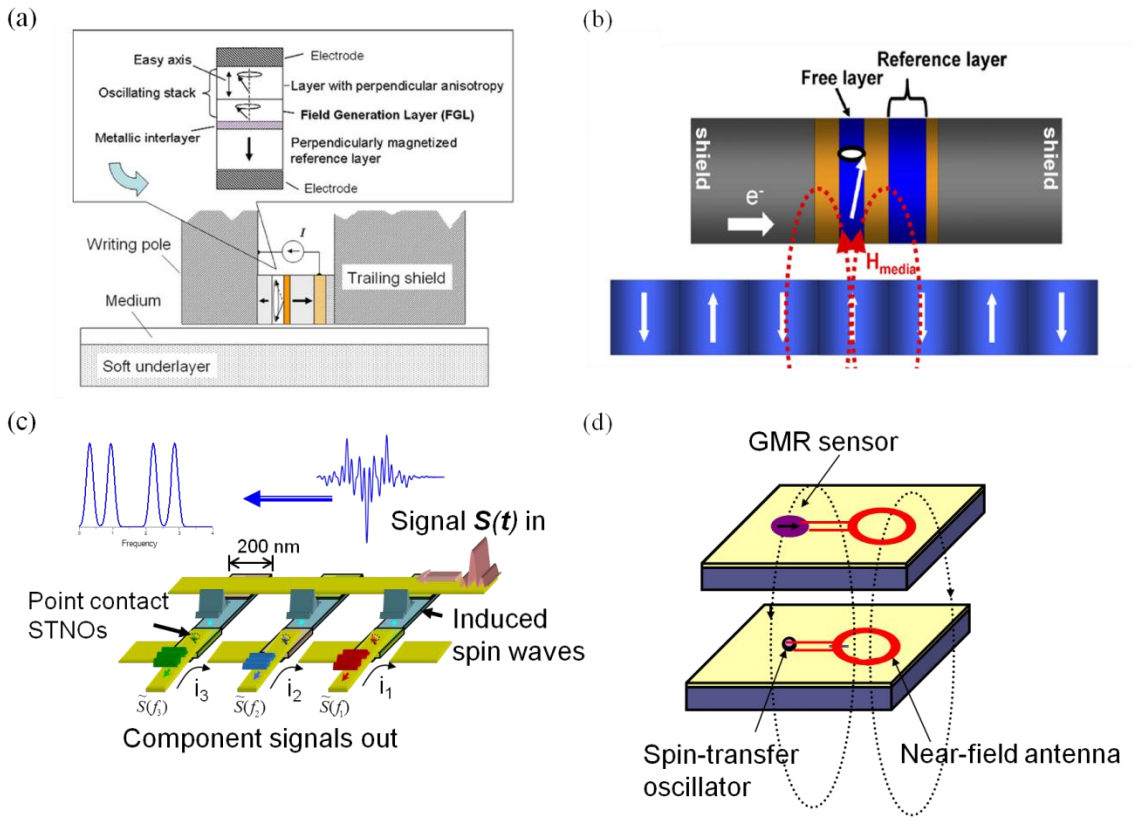


Figure 1-18 Protential applications for spin torque oscillatior: (a) microwave assistant magnetic recording [121] (b) reader sensor for hard disk drive [127] (c) high-density massively-parallel microwave signal processors [128] and (d) chip-to-chip micro-wireless communications.

barrier for the development and the integration of this device. Figure 1-18 (b) shows another potential application for magnetic recording head: reader sensor [127, 129]. As intruded in last section, the oscillation frequency of the free magnetic layer is proportional to the external magnetic field. So the oscillation device is able to response to the media field. Since the frequency of the spin torque oscillator is about several GHz, this reader potentially could be important for the high data rate recording. Figure 1-18 (c) shows a possible application which uses a set of spin torque oscillators with different

frequency to demodulate incoming signal [128]. However, no experimental demonstration or simulation has been done for this idea. Using the sub-micrometer size oscillator to build a chip-chip communication circuit is another potential application which still has been discussed as a general concept, shown in Figure 1-18 (d). These proposed applications are mainly studied by simulation with little experimental work. The reason might be due to the performance gap between the exciting device and application requirement, for example the output power and linewidth. In this dissertation, the improvements for the key oscillation metrics are focus of interest.

# Chapter 2. Device fabrication and characterization

In this chapter, the magnetic tunnel junction thin film fabrication, current perpendicular to plane device lithography and transport properties characterization method are introduced and discussed. The magnetron enhanced sputtering system is used for preparing the magnetic tunnel junction stacks which are characterized by thin film metrology tools such as vibrating sample magnetometer, atomic force microscope and x-ray diffractometer. In order to have the current perpendicularly flow through the magnetic tunnel junction, a set of lithography processes is involved. The electron beam lithography is mainly used to define the nanometer scale magnetic tunnel junction pillars. By having the photo lithography patterned electrodes, the transport properties can be measured based on the tunneling magnetoresistance. The resistance versus magnetic field or DC current hysteresis loops are characterized using standard current and voltage (I-V) measurement setup. The high frequency magnetic dynamic behavior requires analyzing the data collected by the broadband spectrum analyzer or the storage oscilloscope.

## 2.1 Magnetic tunnel junction wafer fabrication

### 2.1.1 Magnetic tunnel junction thin film stack overview

A conventional MgO barrier based magnetic tunnel junction thin film stack requires multiple metal and insulator layers to function as high tunneling magnetoresistance device. Figure 2-1 (a) shows a basic thin film structure on a silicon wafer. The bottom lead provides the electrical contact for the magnetic reference layer on the bottom side of

the tunneling barrier. The bottom lead has to be thick enough to avoid high resistance and to tolerance the over etching (ion milling) during the lithography process. Meanwhile, the roughness of the bottom lead has to be controlled since the MgO barrier is less than 2 nm and the thickness of the magnetic layers at both sides of the MgO barrier are also thin, less than 3 nm. The antiferromagnetic (AFM) layer (PtMn or IrMn) is deposit to pin the magnetic pinned layer CoFe on top of it. The magnetic pinned layer, thin Ru layer and the magnetic reference layer CoFeB are known as the synthetic antiferromagnetic (SAF) layers. The antiferromagnetic coupling through the Ru stabilizes the magnetic reference layer and then avoids switching under small magnetic field. Another advantage of the SAF layers is to break the texture from PtMn AFM layer in order to have an amorphous CoFeB reference layer. In this case, the MgO barrier can be grown on amorphous CoFeB reference layer in the textured [0 0 1] orientation. The MgO barrier and two magnetic layers, reference layer and free layer, create the basic magnetic tunnel junction shown as the layers between arrows in Figure 2-1(b). At the top the sandwich structure, a metal capping layer is needed to protect the magnetic free layer. The wafers are prepared by the magnetron sputtering system: Shamrock as shown in Figure 2-2. The system includes three chambers as Load Lock, Transfer Chamber and Main Chamber. In the main chamber, five DC sputter guns support the metal deposit and one RF sputter gun is used for MgO barrier deposit. The ion etching can clean the wafer before the deposit if needed. After being prepared by the sputtering system, the wafer has to be annealed under the magnetic field. The annealing process has to be done in order to achieve two purposes.

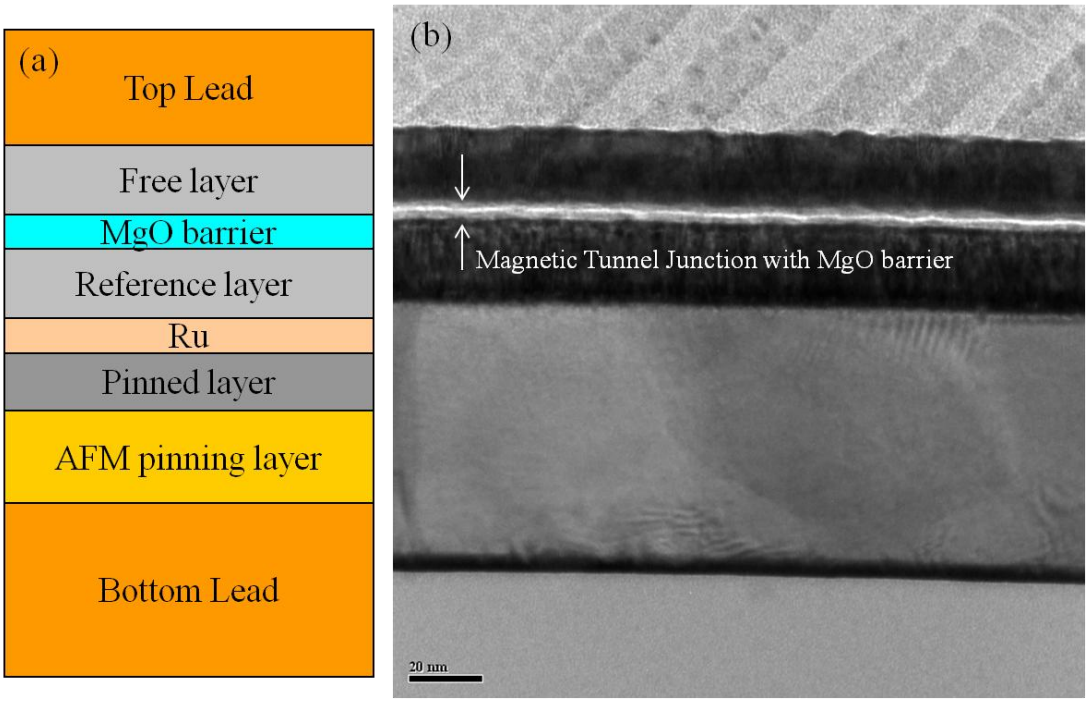


Figure 2-1 (a) The schematic structure of the magnetic tunnel junction wafer. (b) The TEM cross section of the actual wafer with magnetic tunnel junction stack.

First, the pinning direction has to be defined by the magnetic field during the annealing process. For this purpose, the temperature has to be high enough to reach the blocking temperature of the AFM layer and the magnetic field has to be large enough to saturate CoFe pinned layer especially during the cooling. Second, the MgO barrier and the magnetic layers on both side can form the [0 0 1] texture during the annealing. For this purpose, a higher temperature, such as 400 ºC, will be better for MgO crystallization. However, the high temperature can cause the diffusion of the metal layers especially for the AFM material. The annealing process used for wafer is at 300 ºC under 1 Tesla field for 2 hours.

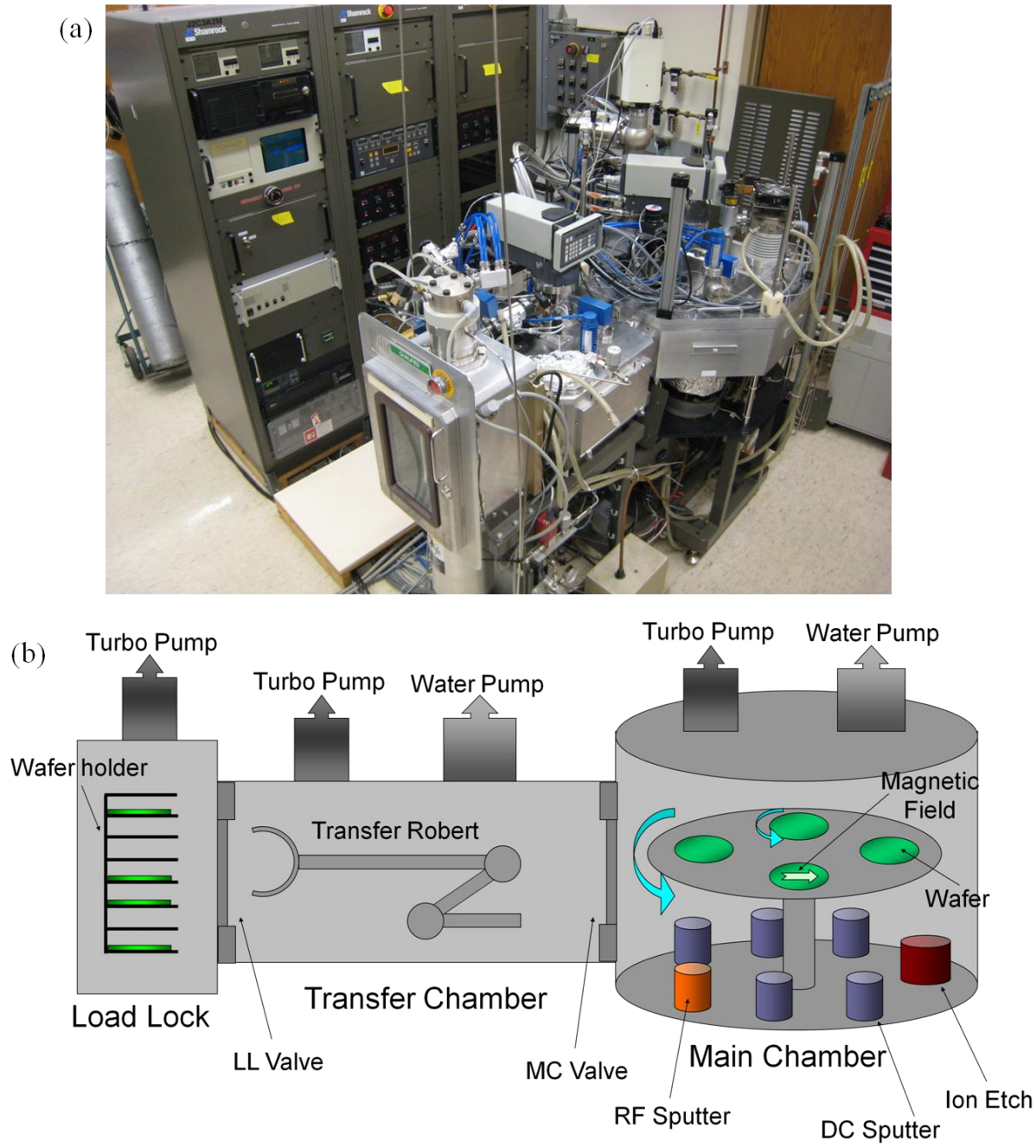


Figure 2-2 (a) Shamrock magnetron sputtering system. (b) The sputter system structure.

### 2.1.2 Film characterization

The film has to be characterized at each critical step during the deposit process, such as roughness, AFM texture, barrier crystal structure and the magnetic properties. In this subsection, the related thin film characterization during the MgO based MTJ device development are introduced.

As mentioned in the last subsection, the bottom lead thickness and roughness are important for the device fabrication process and the quality of the thin layers of the tunnel junction. Figure 2-3 shows the atomic force microscope image of the bottom lead. The basic structure of the bottom lead is Ta/[Al/Cu]n/Al/Ta based on previous study [130]. The Cu layer is inserted to the thick Al layer to break the crystal structure and improve the roughness. Based on this structure, samples with different sputtering condition are prepared and tested by atomic force microscope. Under the same file structure, the roughness is very similar from sample to sample with slightly different sputter condition. Figure 2-3(a) and (b) are the atomic force microscope images of sample #126 (Ta 2nm/[Al 15nm/Cu 3nm]$_3$/Al 15nm/Ta 3nm) and #127(Ta 2nm/[Al 10nm/Cu 3nm]$_5$/Al 5nm/Ta 3nm). The roughness is 0.267 nm for sample # 126 and 0.247 nm for sample #127.

A MTJ film stack should include anti-ferromagnetic layer, pinned layer, reference layer and free layer. As discussed in the last subsection, the free layer has to be switched under small magnetic field without the reference layer and the pinned layer being switched. Figure 2-4 shows the magnetic properties of free layer (FL), reference layer (RL) and pinned layer (PL) under high and low magnetic field measured by vibrating sample magnetometer. The sample structure is as follows: bottom lead 780/Ru 30/IrMn

100/CoFe 25/Ru 8/CoFeB 30/ MgO 15/ CoFeB 30/Ru 30/Ta 100/Ru 70 (unit in Å). As shown in Figure 2-4(a), under a large negative field (-5000 Oe), all three magnetic layers are saturated along the negative field. With field sweeping from -5000 Oe to 0 Oe, the pinned layer switched back to the pinning direction. With the field crossing the zero field, the free layer switched under a small magnetic field. At +5000 Oe three magnetic layers are aligned again by having the reference layer switched. Here, both pinned layer and the reference layer switch under higher field due to the ferromagnetic coupling from the AFM layer and the SAF coupling through the Ru layer, respectively. Figure 2-4(b) shows the free layer switching under lower magnetic field with a stable reference layer. The shift of the free layer hysteresis loop is due to the weak coupling between the free layer and the reference layer.

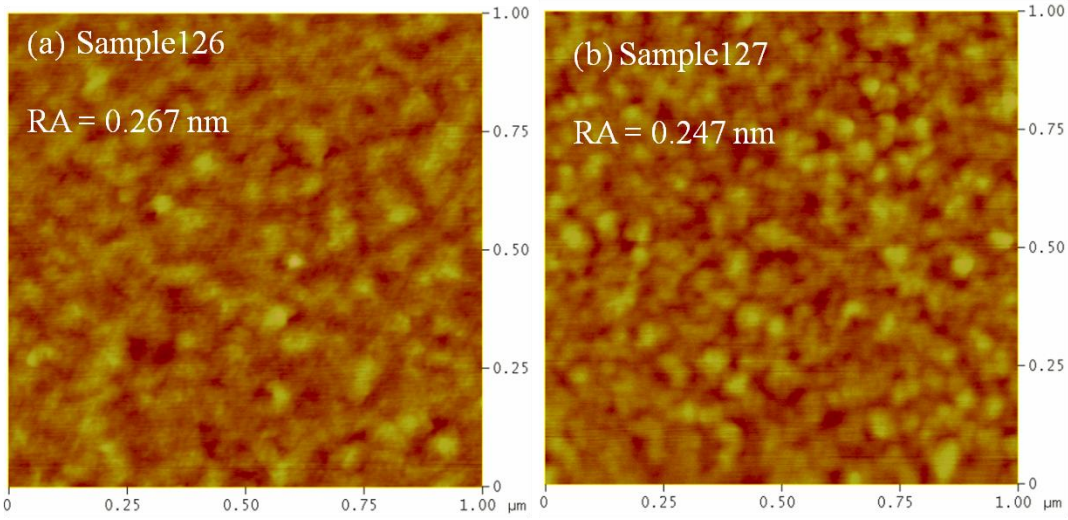


Figure 2-3 Atomic force microscope images (1µm by 1µm) and measured roughness of bottom electrode sample (a) #126 and (b) #127

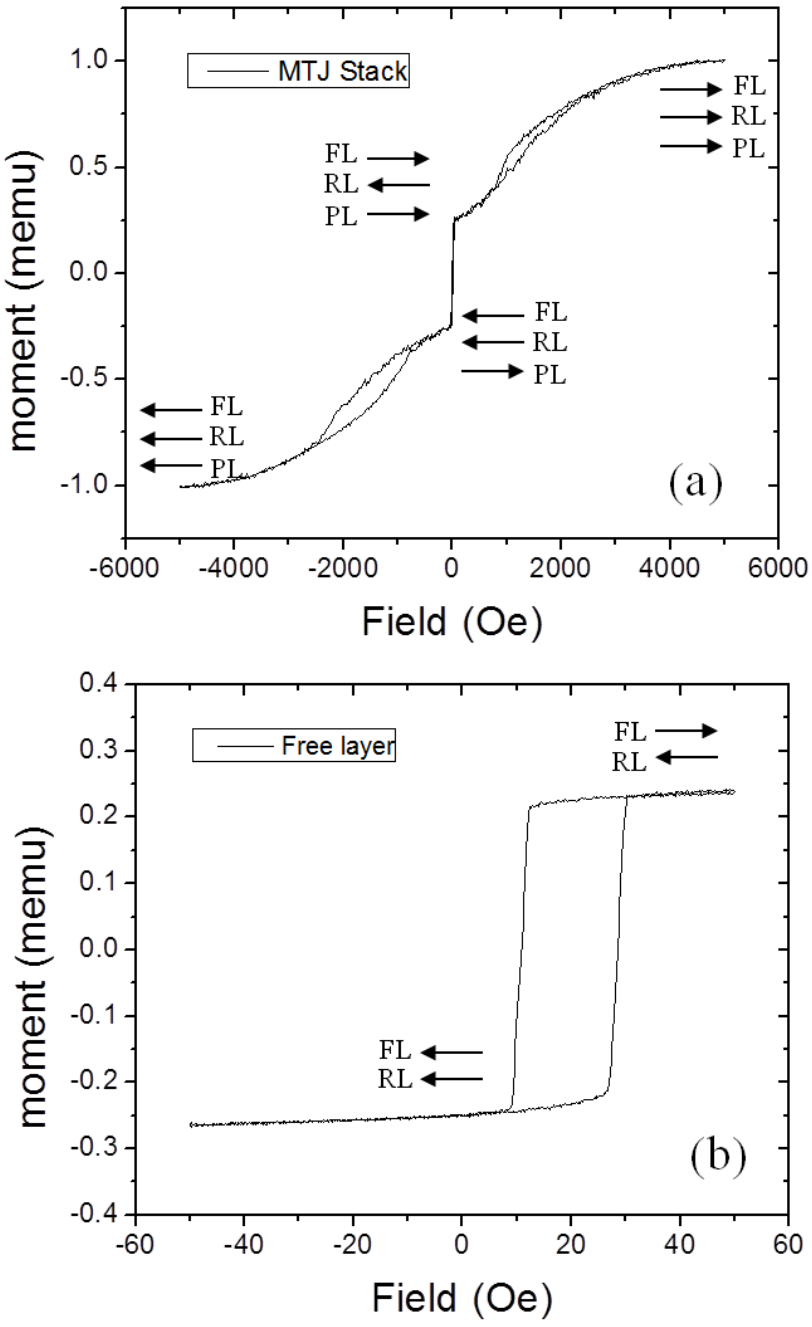


Figure 2-4 Vibrating sample magnetometer result of (a) the response of MTJ full stack under high field and (b) the free layer response to the low magnetic field.

In order to have high TMR ratio, the MgO barrier has to be deposit as [0 0 1] texture. The seed layer is very important for the deposition of the MgO layer. In the case of MTJ device, the seed layer is CoFeB reference layer which needs to be deposit as amorphous. Figure 2-5 (a) shows the x-ray diffraction meter result of a 6 nm MgO layer deposit on the 3 nm amorphous CoFeB layer. The peak represents the MgO [0 0 1] texture. Figure 2-5 (b) gives a cross section image of MgO layer taken by the transmission electron microscopy showing the crystallized MgO barrier.

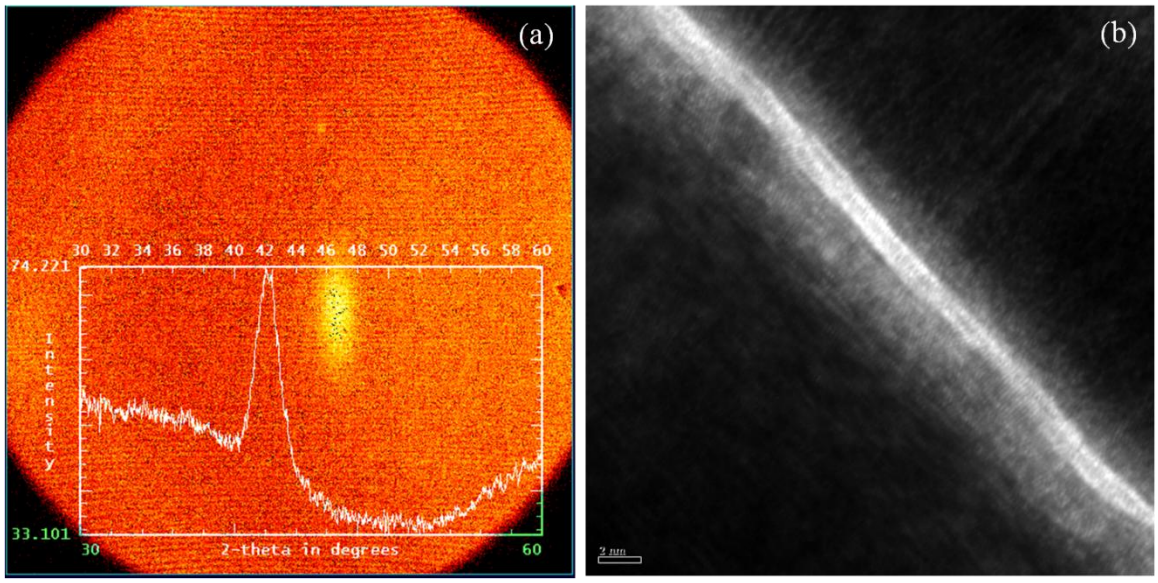


Figure 2-5 (a) X-ray diffraction meter and (b) transmission electron microscopy image for the MgO barrier

The vibrating sample magnetometer test is done in the Institute for Rock Magnetism (IRM), University of Minnesota. The atomic microscopy test, the X-ray diffraction meter test and the transmission electron microscopy are done in the Characterization Facility, University of Minnesota.

## 2.2 Nanometer scale spin transfer torque device lithography

### 2.2.1 Mask design and lithography process overview

In order to have the current tunneling from one magnetic layer to another through the barrier, the film stack has to be patterned by lithography processes to have the MTJ pillar with separated bottom lead and top lead. Figure 2-6 shows typical cross section image of a current perpendicular to plane MTJ device. The MTJ nanometer scale pillar is surrounded by the SiO2 insulator to make sure the current flow from one lead to another

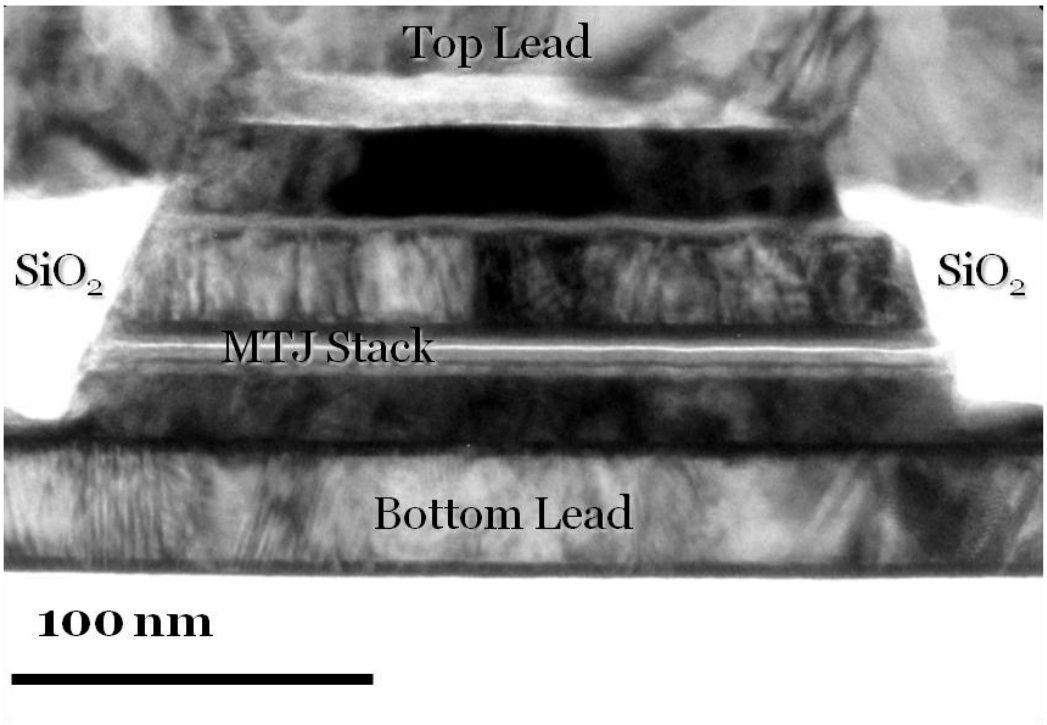


Figure 2-6 Transmission electron microscopy cross section image of a current perpendicular to plane MTJ device [130].

by tunneling trough the barrier. Because the MTJ stack deposition is based on the sputter technique and the device needs to be sub micrometer size, the device fabrication is designed based on the top-down technique, mainly including bottom lead definition/milling, MTJ pillar definition/milling, via open and top lead definition/deposit. The MTJ pillar fabrication is the only step which requires the electron beam to define the nanometer scale pattern. Other leads related process can be done by photolithography.

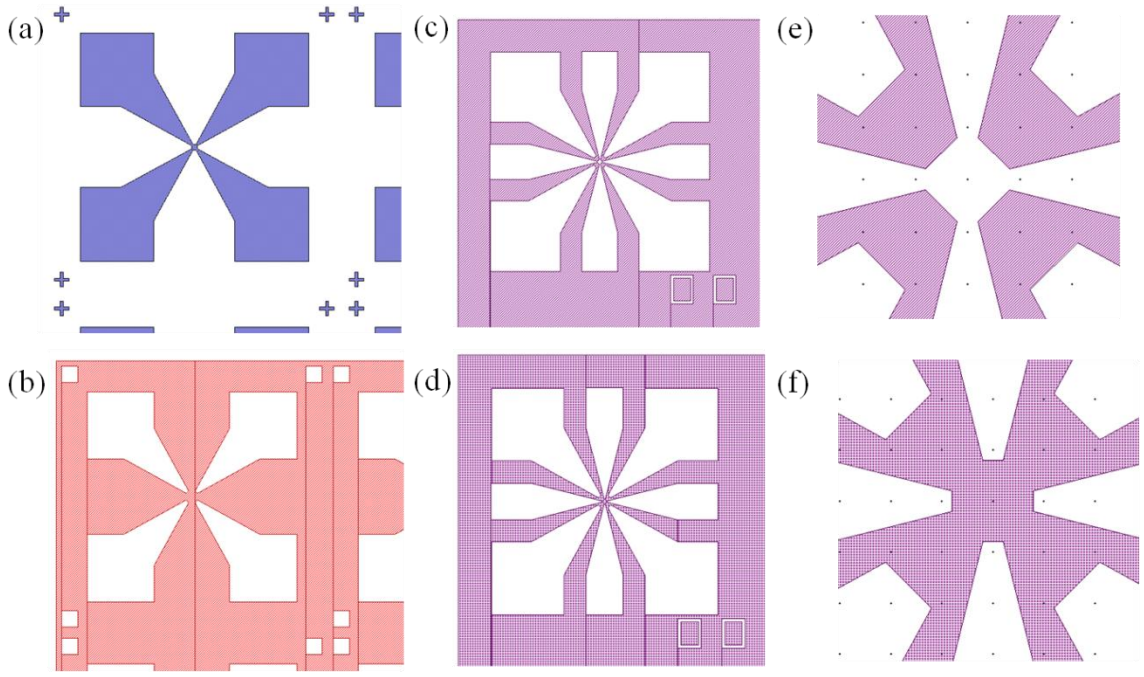


Figure 2-7 Designed masks for the photolithography process: (a) bright field bottom leads etching mask; (b) dark field bottom leads via open mask; (c) dark field top and bottom leads deposit mask with connected four top contact pads; (d) dark field top and bottom leads deposit mask with separated four top contact pads; (e) and (f) are the center zoom in for (c) and (d) respectively.

Figure 2-7 shows the set of the coplanar waveguide masks for bottom and top leads patterning. Figure 2-7 (a) shows the bottom leads pattern. Four big pads at each corner are the contact pads for probing. The leads get narrower to the center where the MTJ device will be located. The crosses surrounding the bottom leads pattern is the alignment marks for the electron beam local alignment process. Figure 2-7 (b) is the mask for the bottom leads via open. Figure 2-7 (c) with a zoom in drawing (e) is one of the final top-bottom leads deposit mask. For this mask, the four top contact pads are connected. So it is equivalent to use any one for probing. It can support multi-probing for special measurement, such as 4-wire IV measurement and transmission coefficient measurement. Figure 2-7 (d) with a zoom in drawing (f) is another type of top-bottom leads deposit mask, where four pads are not connected to the device area. This mask can be used to control multiple devices individually for any special application. Extra electron beam process is necessary to connect the tips of the top leads and the specific devices. The step by step process will be introduced in the next sub section based on these mask design. There are two sets of these masks for 4 inch wafer and 2x2mm chip respectively.

### 2.2.2 Nanometer scale device fabrication by electron beam lithography

The nanometer scale MTJ pillar fabrication is the most important step in this top-down device process. The nanometer scale pillar can be defined by electron beam (e-beam) lithography by using two different types of e-beam resist, positive and negative. The related following processes are also different for making the MJT pillar which makes both of them have their own advantages and disadvantages.

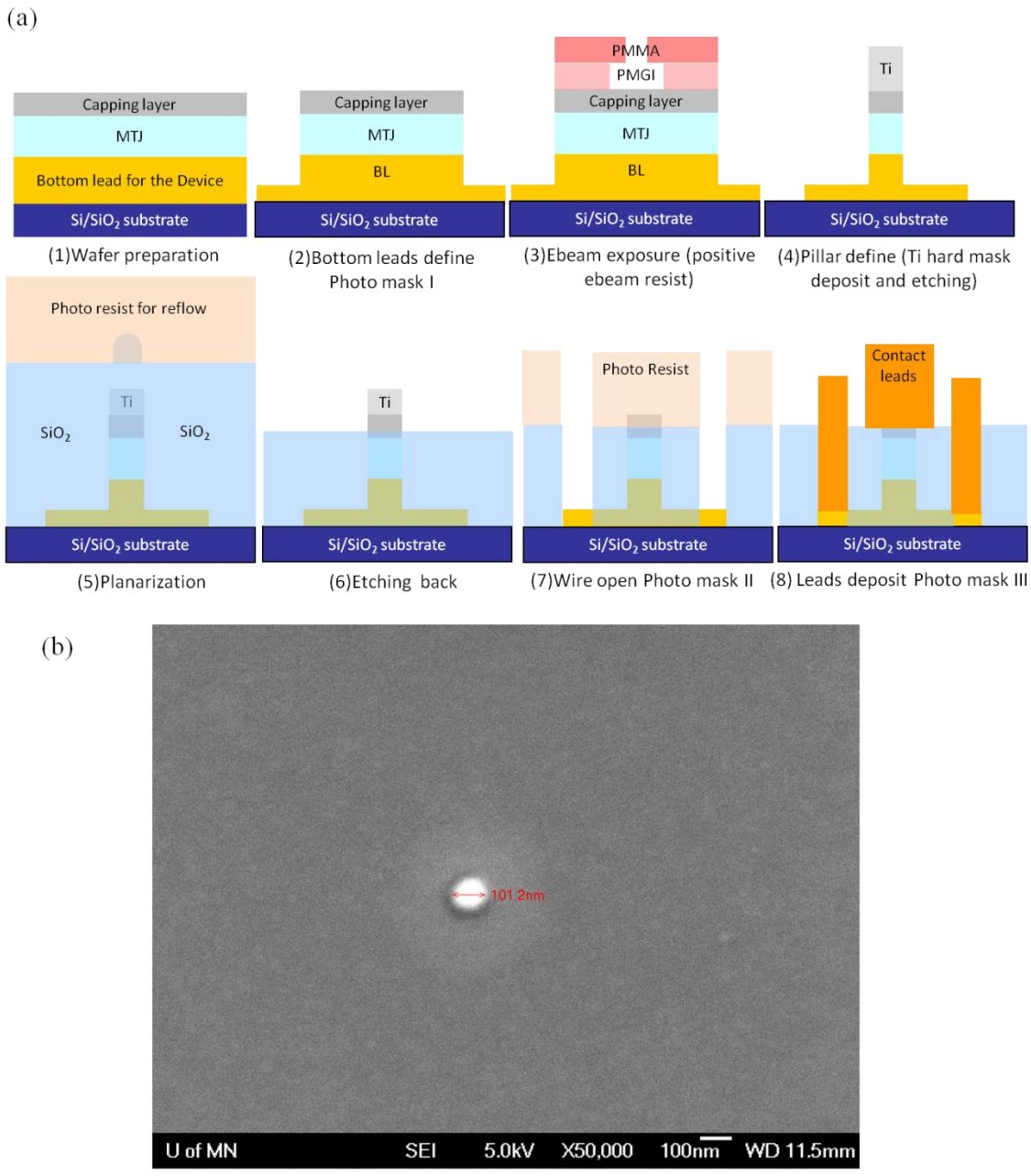


Figure 2-8 (a) Process detail by using the positive e-beam resist for MTJ pillar fabrication

(b) SEM image of the Ti hard mask

Figure 2-8 (a) shows the schematic drawings of the device cross section view based on the e-beam lithography process using positive resists. The step-by-step process is described as follows. (1) The fabrication process starts with a wafer with all the thin film layers deposit including the bottom lead, MTJ and a capping layer on top. (2) The bottom lead is defined by the bright field bottom lead photo mask I (Figure 2-7 (a)) followed by an ion mill etching process. (3) The bi-layer positive e-beam resist is used for the lift-off process. The bottom PMGI resist needs to be developed more than the top PMMA resist to have an undercut for the hard mask Ti deposit and lift-off. The Ti hard mask is deposit by the electron beam evaporation system with a lift-off dome. However, the PMGI undercut shouldn't be developed too much to cause collapse of the PMMA. (4) Due to the low ion milling rate, Ti is used as hard mask for the pillar etching process, shown in Figure 2-8 (b). The milling process includes a high angle (perpendicular to film plane) etching to reduce the shadow effect and a low angle etching to clean the re-deposition at the end. (5) SiO2 insulator has to be coated right after the etching process to cover the MTJ pillar. The plasma-enhanced chemical vapor deposition (PECVD) is used for this step to cover the MTJ pillar as well as the hard mask. The topography of the SiO2 will roughly follow the pillar, which means that etching the SiO2 to expose the contact will also expose the tunneling barrier. So photo resist, with similar etching rate to the SiO2, must be coated and planarized through the low temperature bake process. (6) The reactive-ion etching of the planarization process only etches the photo resist at the beginning. Then the etch remove the photo resist and SiO2 at the same time with same etching rate until the top contact (hard mask or capping layer) of the MTJ pillar exposed. The thickness of the residual resist/SiO2 is monitored by ellipsometer to make sure the

contact is exposed but the tunneling junction is not. Since the planarization process is not a perfect uniform process cross the wafer, the capping layer needs to be thick enough to have certain tolerance to expose most of top contact. However, the thick capping layer will make the ion milled MTJ pillar larger than hard mask size due to the etching shadow effect. (7) The rest of the processes are making contact pads for the MTJ pillar. The bottom lead is covered by the SiO2 by end of the planarization process. So a dark field mask (Figure 2-7 (b)) is used for the bottom lead via open. The SiO2 is etched away by the reactive-ion etching which barely etches the metal. (8) Both bottom lead and top lead are deposit by through a dark field mask (Figure 2-7 (c)) with a lift-off process. The detail process steps and conditions are listed in appendix. Among all the process steps, the biggest concern will be the etching back control due to the non-uniform cross the wafer.

Figure 2-9 (a) give an alternative way to pattern the MTJ pillar by using the negative e-beam resist. (1) The process starts with the same wafer with thin capping layer different from the thick capping layer in the positive e-beam process for the etching back tolerance. (2) The bottom lead is patterned with same mask. (3) For the negative e-beam resist, single layer resist works as etching mask to define the MTJ pillar after the exposure and develop processes. The MTJ pillar etching process should be as quick as possible to prevent the negative resist getting too hard to remove. So the capping layer should be kept as thin as possible. (4) In this SiO2 insulator deposit step, the electron beam evaporation system with lift-dome in order to make the lift-off process easier. (5) The lift-off step can be hard if the negative resist turn hard by ion milling or the SiO2 covered

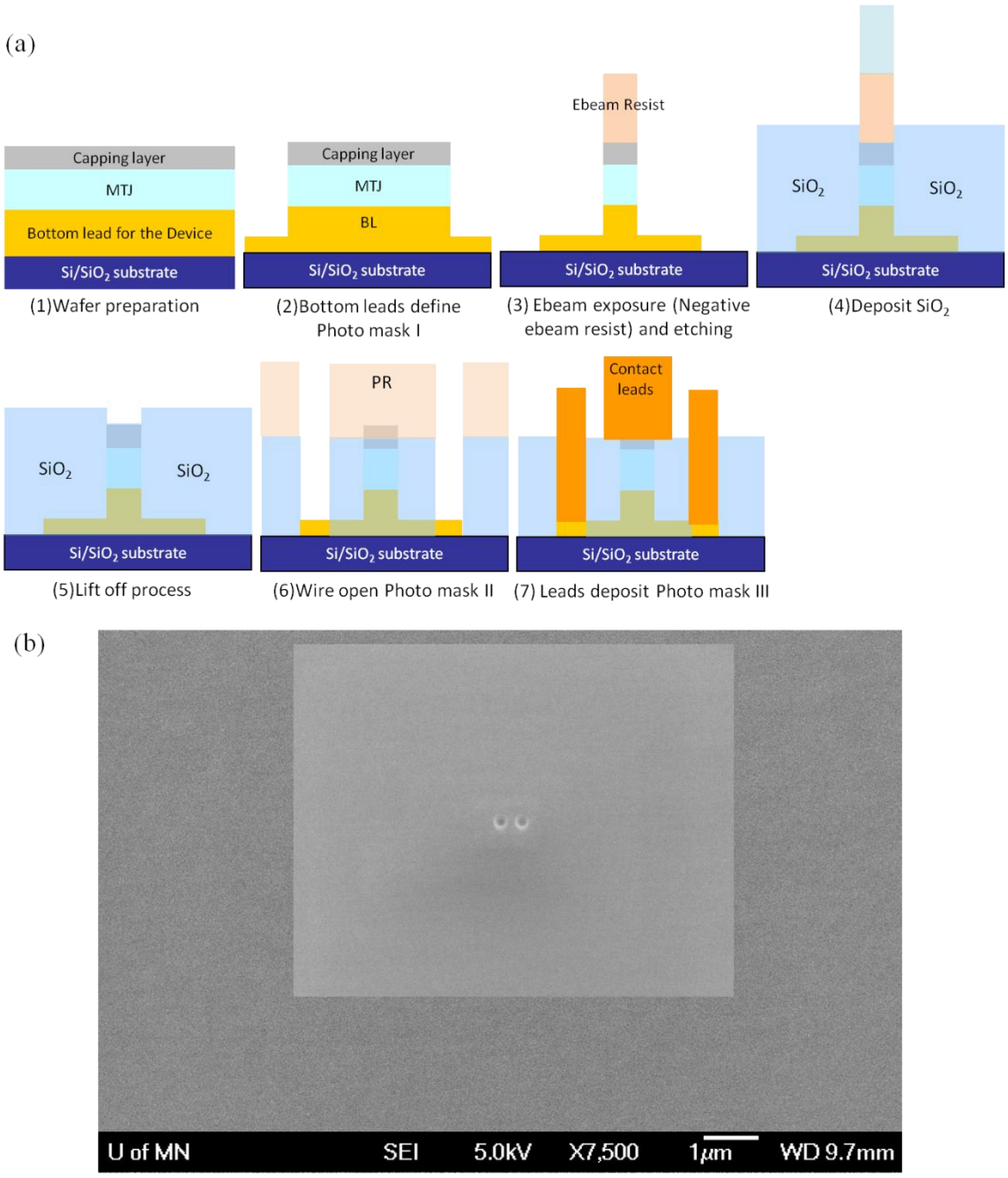


Figure 2-9 (a) Process detail by using the negative e-beam resist for MTJ pillar fabrication (b) SEM image of top contacts after lift-off process.

the side wall of the e-beam resist. The heated N-Methyl-2-pyrrolidone (NMP) is used for the negative e-beam resist lift-off process. Ultrasonic the NMP bath will be necessary most of the time and foam brush might need if the lift-off is difficult in some area. (6) The bottom lead via open and (7) the top/bottom leads deposit are same as the previous description in the positive e-beam resist process. The lift-off is the most critical step in the MTJ pillar process using negative e-beam resist. Two negative e-beam resists, NEB31-A3 and MaN2403, are compared based on 100nm diameter shown in Table 2-1.

| Resist | NEB31-A3 | MaN2403 |
|---|---|---|
| Aspect ratio (thickness : size) | ~ 3:1 | ~ 6:1 |
| DOSE | ~ 80 | ~ 450 |
| Stability | HDMS | good |
| Remove after ion-milling | good | good |
| Lift-off after depositing SiO2 by electron beam evaporation | good | doable |
| Lift-off after ion-milling and depositing SiO2 by electron beam evaporation | doable | doable |
| Lift-off after ion-milling and depositing SiO2 by PECVD | bad | bad |

Table 2-1 Compare of NEB31-3A and MaN2403 negative e-beam resist

MaN2403 has higher aspect ratio, higher dose and better adhesion. Higher aspect ratio is better in the case of making MTJ pillars by etching and lift-off. Thicker resist allows thick SiO2 covering the MTJ pillar. For the same pattern wrote by e-beam with same resolution, resist with higher dose should use higher beam current. Because each MTJ pillar has to be patterned in a 3x3 $\mu m^2$ area in the center of the bottom lead pattern, Figure 2-7 (a), and there are hundreds of them cross one wafer. Three global alignment marks only leads the beam to where individual bottom lead pattern is. The beam still has to rely on local marks, shown as the crosses at the corners of Figure 2-7 (a). The high beam current provide better image of the marks for each alignment. If the process only

requires remove the resist after etching (ion milling), both NEB-31A and MaN2403 work well. The NEB-31A works slightly better for the lift-off process without any etching prior to it. However, the MTJ device pattern requires both etching and lift-off. In this case, either NEB-31A or MaN2403 is not very easy at the lift-off step but both of them are doable. Overall, the MaN2403 shows advantages on the resist height, the beam current choose and the resist coating stability, with similar difficulty on lift-off step compared with the NEB-31A.

Figure 2-10 shows the image of the finished devices on wafer. Each device has four bottom lead contact pads shown at four corners in Figure 2-10 (b), and the top lead contact pads are in between. This configuration can fit 4 broadband Ground-Signal-Ground (GSG) RF probes at same time if necessary. Usually, one GSG probe will be used for the measurement with 2 ground pins on the bottom lead pads and one signal pin on the top lead pad. GSG probes with pitch size between 160 μm and 150 μm can fit the photolithography patterned pads.

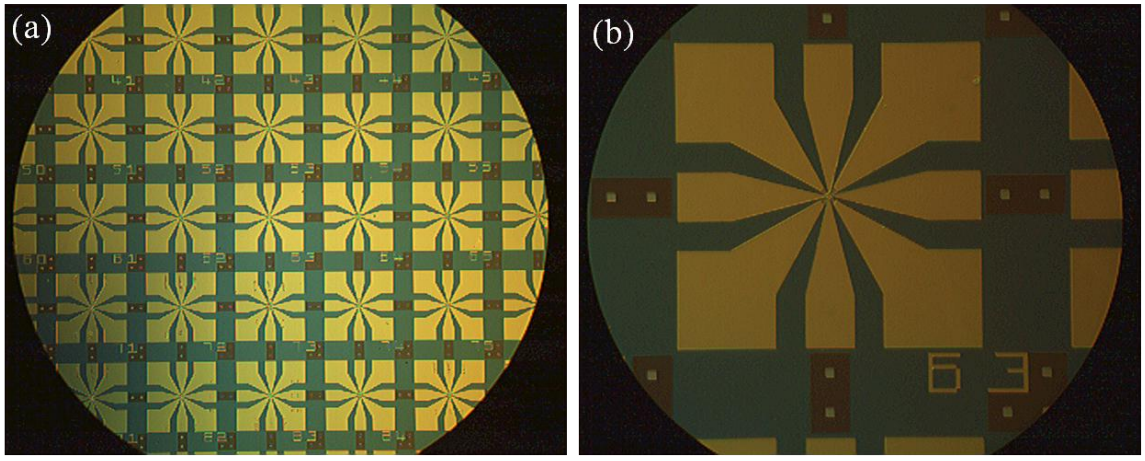


Figure 2-10 (a) Finished devices on wafer (b) zoom in to one device with top and bottom lead contact pads.

## 2.3 High frequency magnetic dynamic behavior characterization

### 2.3.1 Electrical signal measurement introduction

The magnetic dynamic behavior characterization for the device is a magnetoresistance based electrical signal measurement. So the measurement system is mainly built based on electrical components suitable for high frequency capabilities listed in Table 2-2. The ground-signal-ground (GSG) probes are used to connect the devoice contact pad to the 2.92mm SMA cable (18GHz) based measurement circuits. The GSG probes pitch size must fit the pitch size of the lithography pattern. The connect for the GSG probe is usually K-type (40GHz) which is electrically and physically suitable for the SMA cable when the interested band is below 18GHz, however, one K-type to SMA adapter is suggested to protect the K-type connector from physical damage if any stress will be applied to the connection. Bias-T is the key RF passive component to separate the DC current and high frequency AC signal. It includes three ports as DC, AC and DC+AC. The DC port can pass the dc current which is supplied by a current source. The AC port only passes the signal with frequency between 80kHz/10kHz and 16GHz/40GHz to the spectrum analyzer or oscilloscope. The DC+AC port goes to the device under test. If the signal amplitude/power is too low, one or more amplifiers can be added between the bias-T and spectrum analyzer or oscilloscope. Detail model and specification of the electrical test components are listed in Table 2-2.

| Equipment | Model | Function |
|---|---|---|
| Probe | Cascade GSG | Pick up signal from CPW contact pads, up to 40GHz |
| SMA cable | Picosecond Pulse Lab | DC-18GHz |
| Bias Tee | Picosecond Pulse Lab 5541A/5542 | Separate DC and AC signal with 80kHz – 16GHz (5541A) or 10kHz – 50GHz (5542) |
| Amplifier | Picosecond Pulse Lab 5867 | Provide 15dB gain for signal from 10kHz to 15GHz |
| Source Meter | Keithly 2400 | DC current source and voltage meter |
| Spectrum Analyzer | HP8593A | Detect power with frequency range 9kHz to 22GHz and power range -110dBm to 30dBm (50 ohm Load) |
| Oscilloscope | Tektronix DPO72004C | Record the signal by 50GS/s sampling rate (20GHz band, 50 ohm load) |

Table 2-2 Electrical components for the high frequency measurement

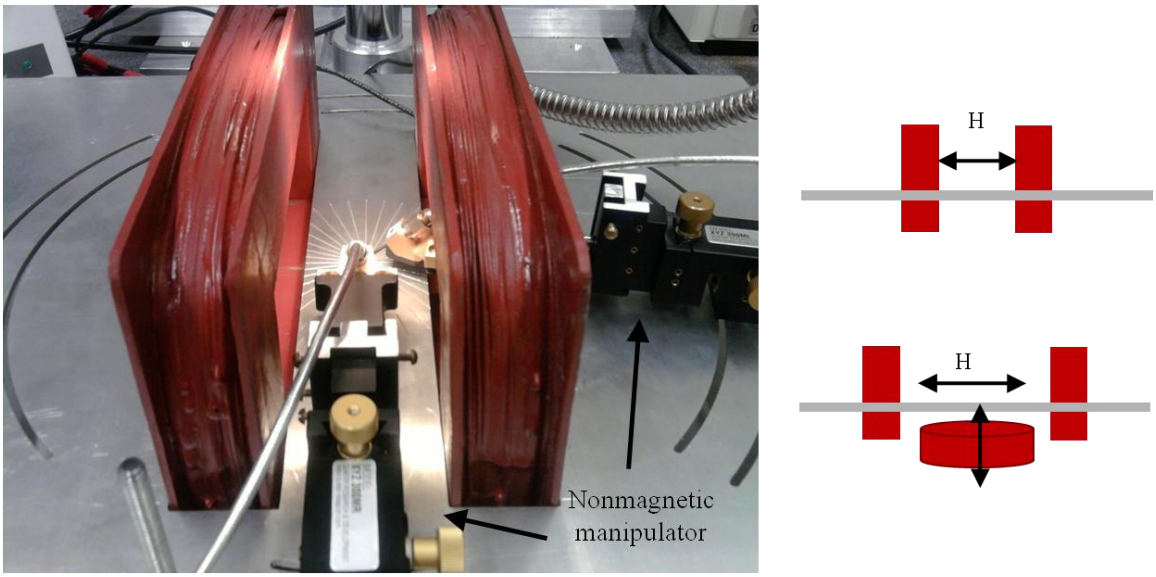


Figure 2-11 Measurement Stage with low in-plane magnetic field

Besides the electrical part, the measurement also needs controllable magnetic field. Two measurement stages are built to meet the different field magnitude and direction requirements. Figure 2-11 shows the low field stage with a pair of magnetic coil which can support in-plane field up to 800 Oe with a pair of ion core underneath the metal plate. By using another metal plate with larger coil gap, one more single coil can be added in to the stage to provide the perpendicular magnetic field. As shown in the figure, the nonmagnetic probe manipulators are mounted on the metal plate to control the probes. The tracks under the probe manipulators will let the probe rotate with the device to allow in-plane magnetic field with different angles to be applied. Figure 2-12 shows the high field stage with a water cool electrical magnet. With the space for the alumina bar, the maximum magnitude of magnetic field is 5000 Oe. Two nonmagnetic probe manipulators are mounted on the alumina bar which can be rotated by the wheel on one end to have the field applied any angle between in-plane and perpendicular to the device film. The sample holder, small circle piece in the center of the bar, can also rotate in small angle in the limitation of the contact pad probing. The probing can be difficulty on this high field state because the rotation of the bar can move the contact.

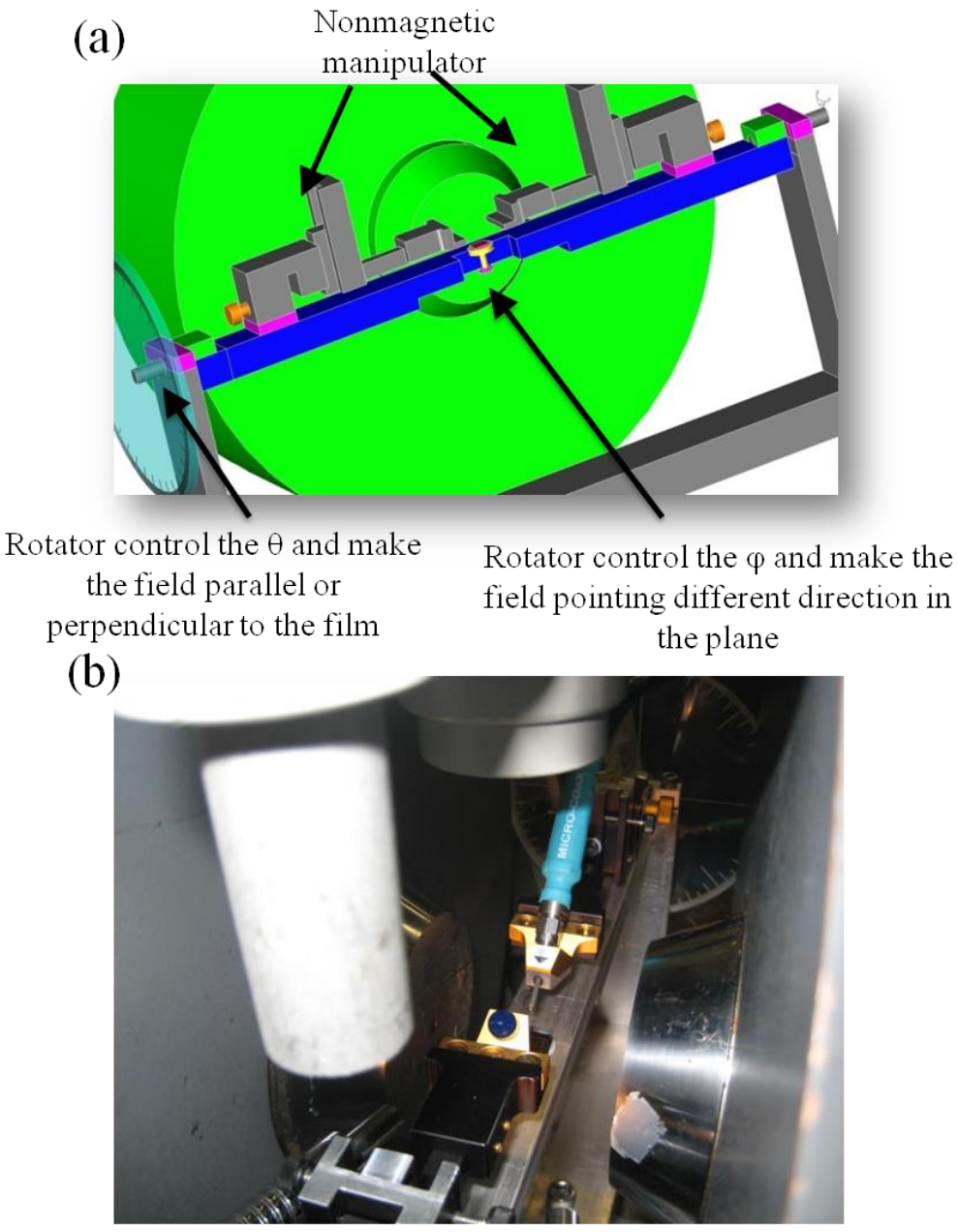


Figure 2-12 Measurement stage with high perpendicular magnetic field capability

### 2.3.2 Frequency domain oscillation signal measurement

The frequency domain measurement is often used to measure the spin torque oscillation. The test electrical setup is shown in Figure 2-13 (a). The device under test is connected to the AC+DC port of Bias-T by a SMA coaxial cable to make sure that the DC current can be sent in to the device and the AC oscillation signal can be transferred out of the device. The DC source-meter is connected to the DC port of Bias-T and the spectrum analyzer is connected to the AC port of Bias-T. When the current source drives the device and excites the spin torque oscillation, the spectrum analyzer collects the AC signal amplified by the broadband amplifier. A typical power spectrum is shown in Figure 2-13 (b). The raw data points collected by the spectrum analyzer are the power at each specified frequency with certain bandwidth known as resolution band width (RBW). The frequency sweep range (span) should cover interested band. Span should be chosen smaller than maximum data point multiple RBW. So power has to be divided by the set RBW and normalized by the amplifier's gain. The data points can be fit by the Lorentz function to find out the key parameters as frequency, peak amplitude and full width at half maximum (FWHM, or linewidth). The current and applied field dependences of these key metrics describe the spin torque oscillation behavior of each specific device.

However, the reflection between the MTJ device and the amplifier in the measurement circuit can affect the power spectrum and further affect the fitting parameter. All the passive and active RF components are schematically shown in Figure 2-14 (a). By changing the cable length, the reflected signal passes different length and shows different delay time to the original signal. So the modulation on the power spectrum will sequentially change with the length of the cable between two reflection points. The

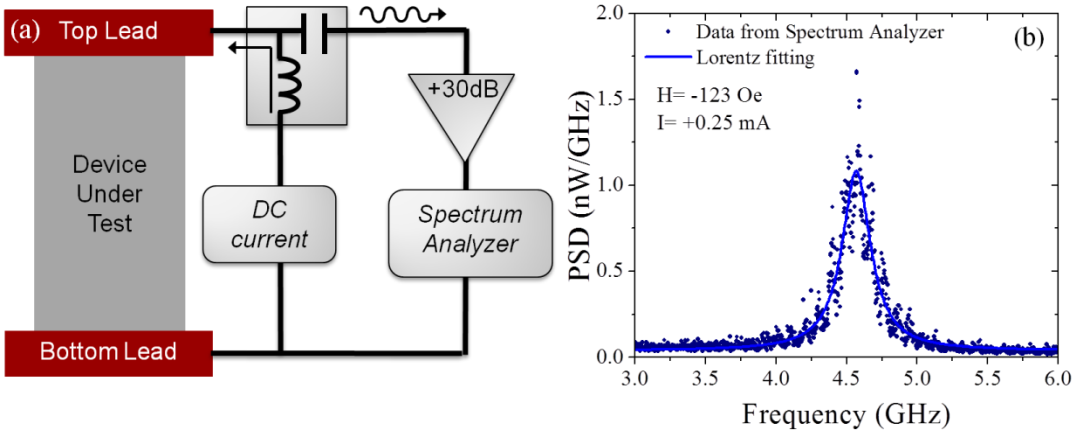


Figure 2-13 (a) The electrical setup of the frequency domain measurement. (b) The measured power spectrum.

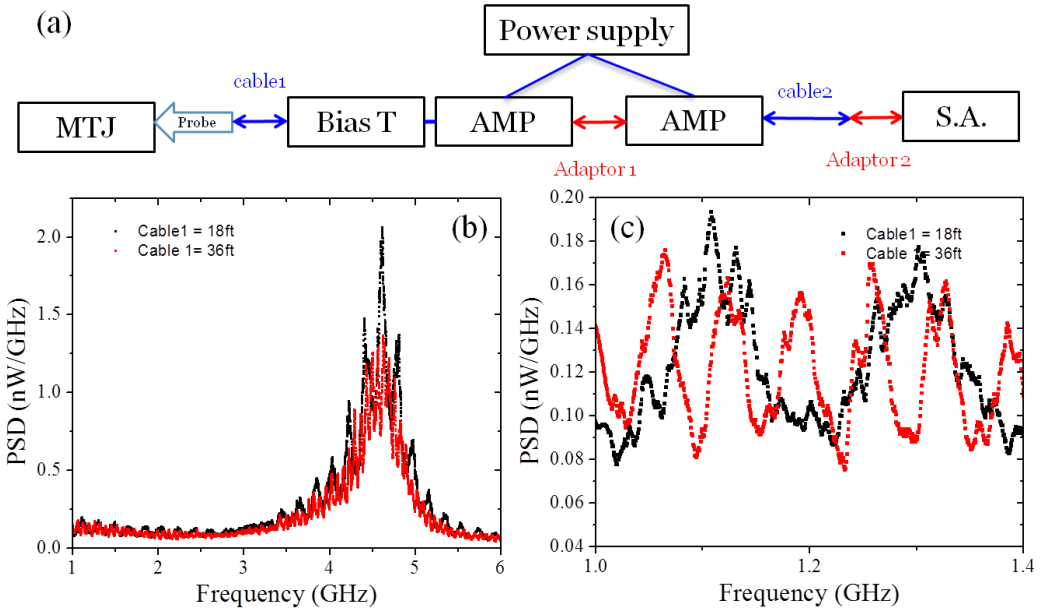


Figure 2-14 (a) AC signal path from the device to the spectrum analyzer. (b) Typical STO power spectra with the effect of reflection. (c) A zoom in view of the power spectra.

reflection is most likely to be between the MTJ device, due to the high resistance with typical value about several hundred ohm, and the amplifier which is the only active RF components in the signal path. Figure 2-14 (b) shows two different spectra using 18 feet and 36 feet cable for cable1 respectively. By zooming in the spectra shown in Figure 2-14 (c), the modulation period is about 200 MHz for 18 feet cable. In other words, the reflection signal is about 5ns late, which is about the time for the signal pass 18 feet twice. When the cable1 is switched to a 36 feet cable, the modulation period is shortened and which means the reflection signal travels longer. By changing the cable2 between the amplifier and spectrum analyzer, no similar behavior is observed.

There are several RF passive devices which can be added to reduce the reflection effect in the circuit, shown in Figure 2-15 (a). The high pass filter can be added to reduce the noise which is mainly lower than 1 GHz. So the filter is good for reduce the noise reflection by reducing the lower frequency noise to the amplifier. Besides the noise, the signal still reflects between the MTJ device and amplifier. The isolator works like a diode within certain frequency band, which means that the isolator can block the reflected STO signal if the signal is in the isolator working range. For both the filter and the isolator, one specific model only supports certain frequency band width. So this limits the study if the STO signal frequency drifts with the external test condition such as current, magnitude and angle of the applied field. The attenuate actually can be used to reduce the effect of the reflection. The original signal and noise are going to travel through the attenuate once while the reflected part will pass twice. So, by using a 3dB or 6dB attenuator, the reflection effect in the circuit can be reduced without any frequency band concern since the attenuator works for broadband.

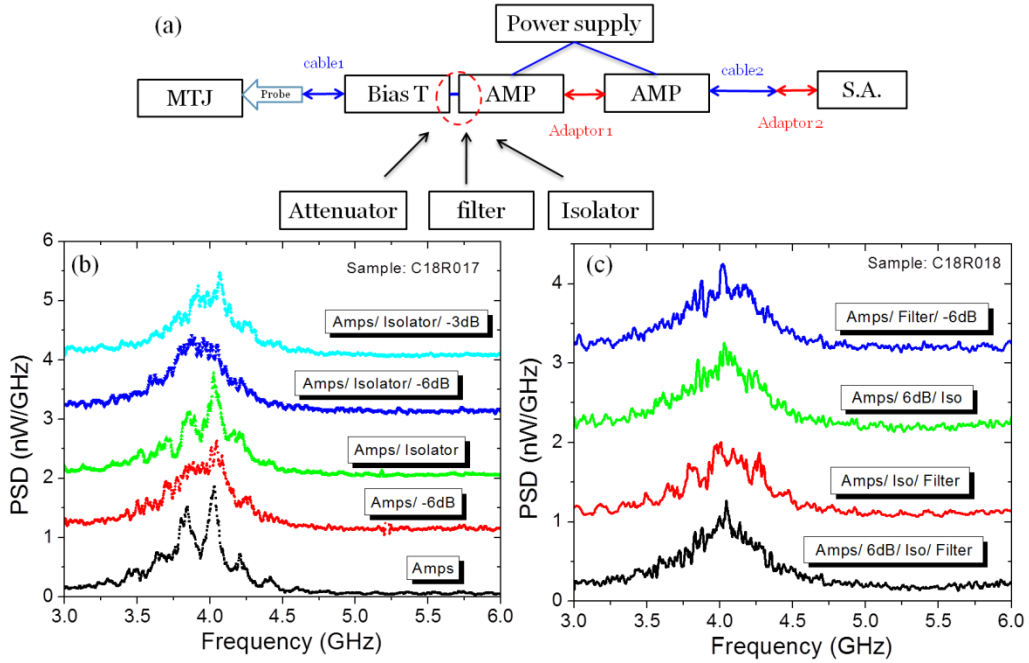


Figure 2-15 (a) The testing circuit setup for reducing the reflection. (b), (c) Power spectra with difference circuit setups.

### 2.3.3 Time domain oscillation signal measurement

The time domain measurement relays on the storage oscilloscope to collect the real time domain STO signal. The testing circuit is very similar to the frequency domain testing. The only difference is to use a storage oscilloscope to replace the spectrum analyzer, as shown in Figure 2-16 (a). The storage oscilloscope has to have higher bandwidth limit than the signal to be measured. Here, the bandwidth for the oscilloscope is 20GHz which is much higher than the typical STO frequencies we studied. The sample rate for the oscilloscope is 50 Giga samples per second which is more than two times higher than the typical STO frequencies. Figure 2-16 (b) shows a typical processed STO signal waveform, and the dots are the sampled voltage points depended on the sampling rate.

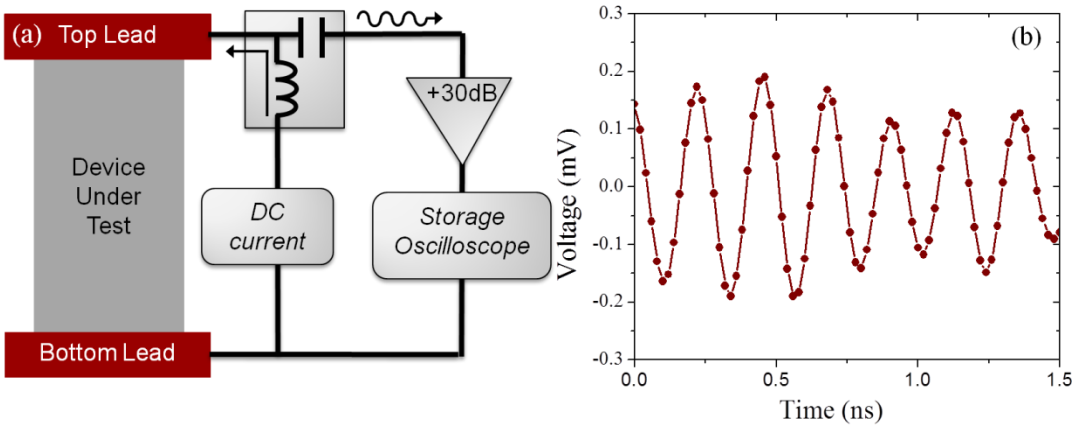


Figure 2-16 (a) The electrical setup of the time domain measurement. (b) The real time signal waveform.

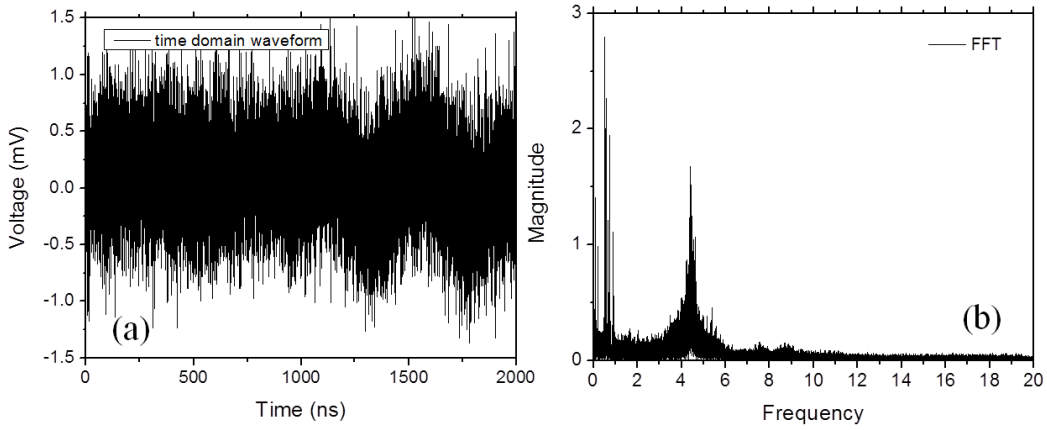


Figure 2-17 (a) The raw waveform collected by oscilloscope. (b) The FFT of the raw waveform.

The raw waveform collected by the oscilloscope includes noise with different frequencies. The raw waveform and the FFT, normalized by the amplifiers' gain, are shown in Figure 2-17. The STO signal is around 4 GHz and the noise is less than 1GHz. So a FFT band pass or high pass filter needs to be applied to the raw waveform. Figure 2-18 shows the waveforms before and after the FFT filter. The result indicates that the FFT

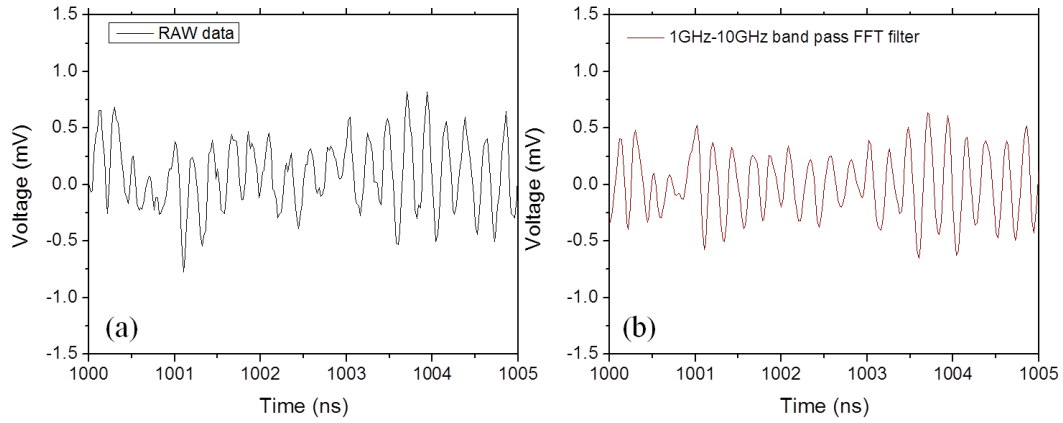


Figure 2-18 (a) The raw waveform and (b) the waveform after the band pass FFT filter.

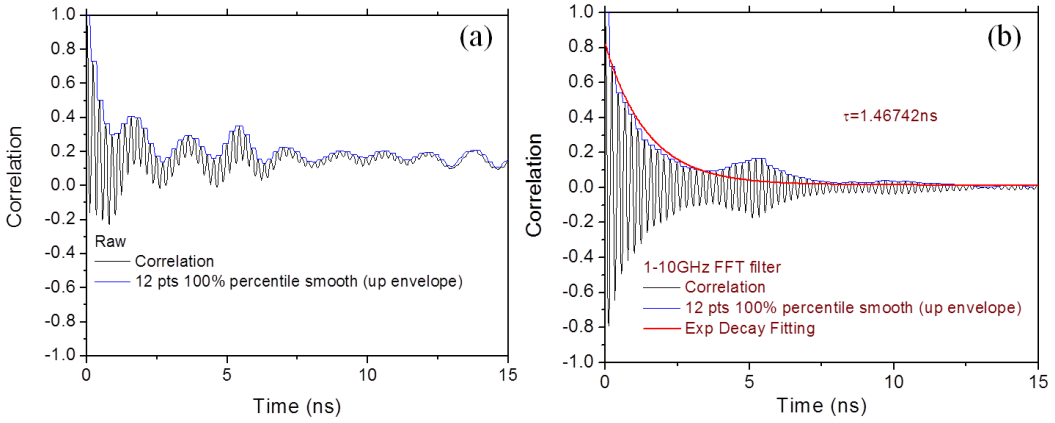


Figure 2-19 (a) The self-correlation of the raw waveform and (b) the self-correlation of the waveform with FFT filter.

filer doesn't change the waveform of the STO signal too much. The FFT filter doesn't change the frequency of the STO signal either. However, the filtered waveform helps to find out the other two key parameters, power and linewidth, to characterize the STO signal. The STO frequency domain power spectrum density shows a Lorentz line shape which means that the autocorrelation function of the real time signal decays exponentially. The decay time constant $\tau_c$ represents the linewidth of the Lorentz function as $\Delta f = 1/\pi\tau_c$. So it is important to find out the decay time constant for the real time waveform of the STO signal. Figure 2-19 (a) and (b) show the autocorrelation results of the real time signal without and with the FFT filter. Both autocorrelation functions show oscillation with decayed upper and lower envelopes. The faster oscillation from the autocorrelation function is due to the STO signal which should show the same frequency, about 4.2 GHz in this case. For the autocorrelation function of the waveform without the FFT filter, the envelopes look like being modulated by a slow oscillation which is actually the noise from the lower band shown in Figure 2-17 (b). After the low frequency band noise being filtered, both upper and lower envelopes of the autocorrelation function give clear exponential decay behavior, as shown in Figure 2-19 (b). The upper envelope of the autocorrelation function can be found by using 100% percentile smooth. The smooth point is determined by the sample rate and the frequency of the STO signal. For example, the 12 point percentile smooth is used based on the 50G sample per second and 4.2 GHz signal. Therefore, the envelope is able to be fit by the exponential decay function to determine the decay time constant. The bumpers at 5 ns, in Figure 2-19 (b), indicate the reflection travelling time in the circuit as discussed in last section.

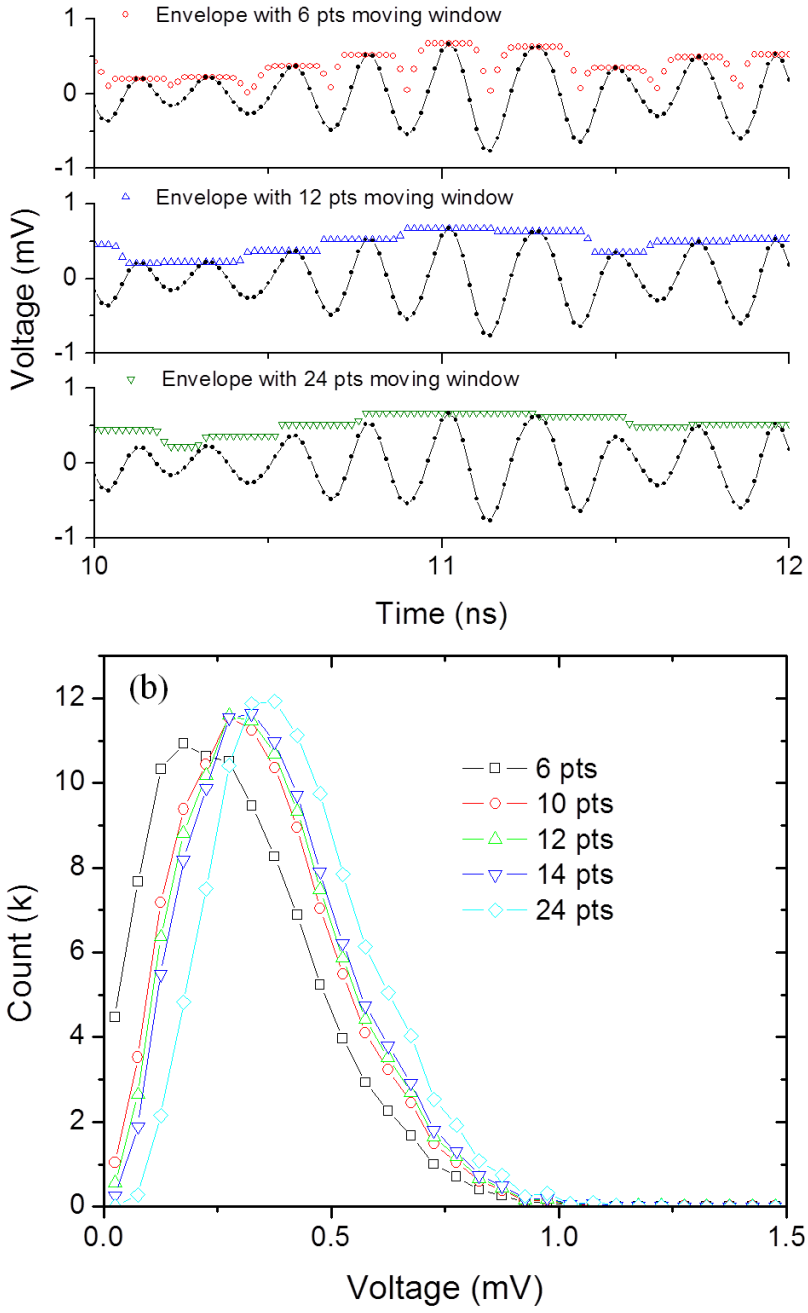


Figure 2-20 (a) The envelope of the STO signal waveform and (b) the peak amplitude distribution by using the percentile smooth with different points.

For the time domain signal, the peak to peak amplitude is the metric needs to be measured to characterize the magnitude of the STO signal. Taking the envelope of the real time waveform can measure the peak amplitude of each oscillation period, show in Figure 2-20 (a). The peak amplitude gives a distribution as show in Figure 2-20 (b). The 100% percentile smooth is used here for the waveform upper peak amplitude and 0% percentile smooth is applied for the lower envelope. The smooth points have to be close to the data points each oscillation period contains which can be estimated by the sampling rate divided by the STO signal.

# Chapter 3. Spin toque oscillator polarizer angle dependence

In this chapter, the power angular dependence of spin torque oscillation is systematically investigated in dual MgO based magnetic tunnel junctions (MTJs) with tilted polarizer angles controlled by lithography technology. The power increasing with the tilted angle is experimentally proved by analyzing the power spectra data. The power spectral density efficiency at the main peak is 2-3 times (for 30° tilted polarizer MTJ) and 5-6 times (for 60° tilted polarizer MTJ) larger than that in the conventional MTJ with the free layer and pinned layer being parallel. In additional, the power efficiency increases with the applied current at different tilted polarizer angle also qualitatively fits the precession angle power dependence.

## 3.1 Introduction

As being discussion in chapter 1, studies have been focused on several key engineering challenges, such as high power, narrow line width, and tunable frequency and oscillation operation conditions due to its potential applications. It has been clear theoretically and experimentally that the spin torque depends on the angle between two sandwiched ferromagnets with a non-magnetic spacer layer [131-132]. Furthermore the out-of-plane field angular dependence has been introduced to understand the GMR-SV spin torque oscillator with in-plane magnetization for both ferromagnetic layers [133-134]. Recently a planar GMR-SV oscillator with a perpendicular polarizer has been theoretically

suggested [106] and experimentally demonstrated [104] as a bias-field-free STO candidate. The out-of-plane angle dependence of tilted polarizer has been theoretically studied to optimize the oscillator [135]. So far, there is no experimental report on any bias-field-free STO with angular dependent polarizer, e.g. tuning the magnetization of the polarizer layer without using any external field. To our best knowledge, one of main obstacles for this is to find a proper way to make such a device.

In this work, we report our first time effort to fabricate bias-field-free STOs with angular dependent polarizer directly by Electron Beam Lithography and magnetic field post-annealing. In-plane MgO based MTJs are used. The easy axis direction of the free layer is fixed by following the long axis of the patterned elliptical shaped device. The angle between the free layer and polarizer layer is adjusted by post-annealing the devices in magnetic field with different direction referring to the long axis of the free layer. By collecting and analyzing the power spectra data, we experimentally show that the power of the fabricated STOs increase with the tilted polarizer angle. Furthermore, the experimental current-power relation is found to qualitatively follow the analytical precession angle-power relation at different tilted angle. The result is well predicted by the time resolved sinusoid MR expression, which is written as a function of the tilted angle and precession angle.

## 3.2 Experiment: device description and power spectra measurement

As a nano-scale device, the free layer of STOs can be considered as a micro-spin with two lowest energy potentials along the easy axis defined by the in-plane shape anisotropy, as shown in Figure 3-1(a). When the free layer oscillates, with the precession angel δ, at the bottom of the energy potential, the power will mainly depend on the resistance change. The cosinoidal MR curves shift with the tilted angle φ (between pinned layer and free layer easy axis) providing an increasing curvature corresponding to the lowest energy potential as shown in Figure 3-1(a). This implies that the power of STOs should be roughly proportional to $\sin^2\varphi$. The time resolved MR can be written as:$R(t) = R_P + \Delta R * [1 - \cos(\varphi + \delta \sin \omega t)]/2$, where $\Delta R = R_{AP} - R_P$, $R_{AP}$ and $R_P$ are the anti-parallel and parallel resistance, respectively. The power of the fundamental harmonic oscillation can be expressed [99, 117]:

$$P(\omega_0) \propto \left(\frac{J_1(\delta)\sin\varphi}{\Delta - J_0(\delta)\cos\varphi}\right)^2 \; and \; \Delta = \frac{R_{AP} + R_P}{R_{AP} - R_P}$$

Figure 3-1(b) shows the power increase with the precession angle (δ) at different tilted angles (φ). It is noticed that the power increasing rate is higher for the large tilted angle whenthe driving current increases. The inset of Figure 3-1(b) shows the tilted angle dependence at different constant precession angle, which are consistent with the deduction from Figure 3-1(a).

The MgO-based MTJ stack, as shown in Figure 3-2(a), was deposited as: seed layer/PtMn (20) /$Co_{70}Fe_{30}$ (2.5) /Ru (0.85) /$Co_{40}Fe_{40}B_{20}$ (2.4) /MgO (0.82) /$Co_{60}Fe_{20}B_{20}$

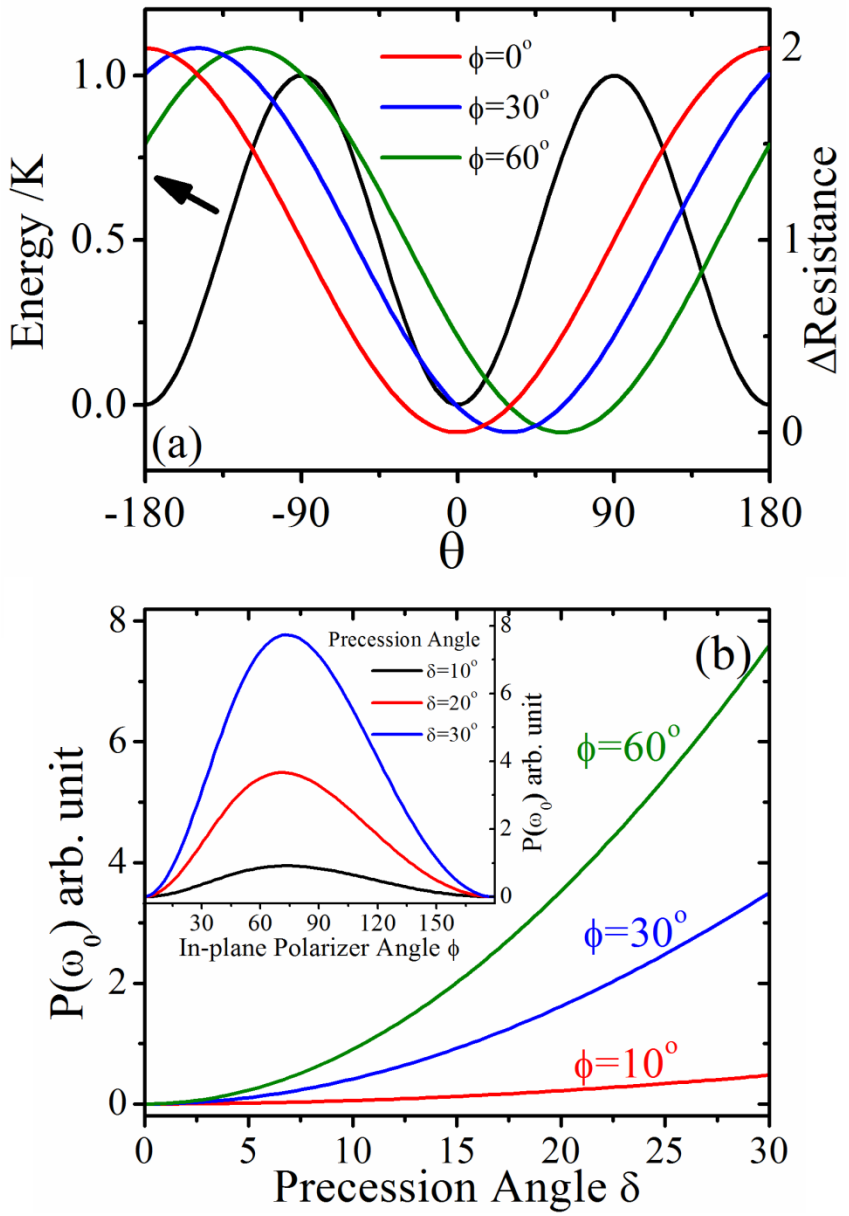


Figure 3-1(a) The energy potential of the free layer based on the Stoner-Wohlfarth model (black curve) and the magnetoresistance-angle relation with different angular polarizer, θ is the angle between the easy axis and the free layer magnetization. (b) The power of first harmonic change with the in-plane precession angle δ with different tilted polarizer angle φ, (inset) and change with the in-plane tilted polarizer angle φ.

(2.0) /MgO (0.91) /$Co_{40}Fe_{40}B_{20}$ (2.4)/PtMn (20)/ capping layer, where the thicknesses in parentheses are in nm. The samples were annealed at 300°C under 1 Tesla field for 2 hours. The MTJs were patterned as 210nm×70nm ellipse with the long axis 0°, 30° and 60° referring to the pinning direction, schematically shown inside the Figure 3-2(b). The MR of 0°, 30° and 60° tilted polarizer MTJs are 15.5%, 14% and 16% with the resistance change of 99 ohms, 90 ohms and 82 ohms, respectively. The coercive field of the MTJs with 0°, 30° and 60° tilted polarizer are 55 Oe, 37 Oe and 62 Oe, respectively. The current induced oscillation data was measured at center of the hysteresis loops. So it is necessary to find out the switching current for each device to determine the applied current range to induce the oscillation before switching. With the small offset field, as -7 Oe, -37 Oe and -30 Oe, applied on the 0°, 30° and 60° tilted polarizer MTJs to center the loops at the high resistance states, the switching current densities from anti-parallel to parallel are $3.29\times10^6$ A/cm$^2$ (0.38mA) and $4.16\times10^6$ A/cm$^2$ (0.48mA) for the 0°, 30° tilted polarizer MTJs, respectively, and the switching current is larger than $6.06\times10^6$ A/cm$^2$ (0.7mA) for the 60° tilted polarizer MTJ. A schematic of the measurement set-up is shown in Figure 3-2(a), and the positive current is defined as the current flow from the top to the bottom. The oscillation signal form the MTJs was detected by the microwave probe and then amplified by +30dB after the dc component was blocked by the bias tee. The typical power spectral data at 0.3mA are shown in Figure 3-2(b) normalized by the amplifier gain, and with the background subtracted. The solid curve shows a Lorentzian fitting of the data, which will be used for showing the subsequent experimental results in this dissertation.

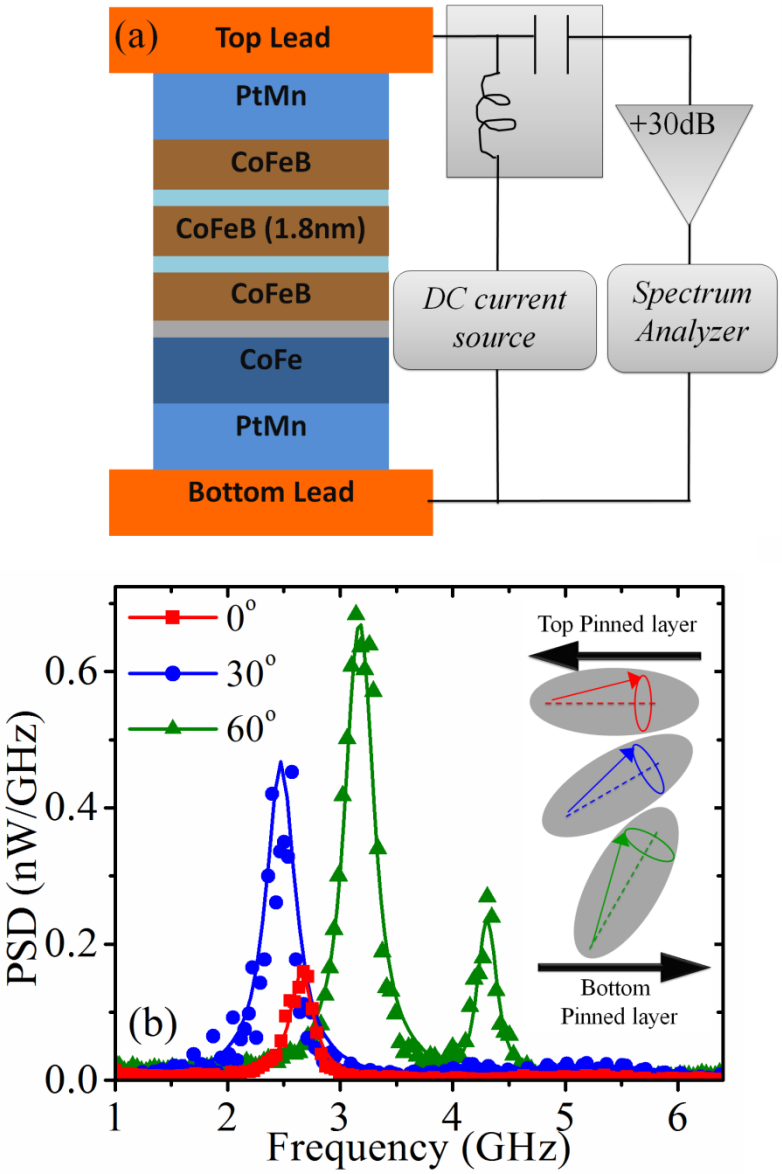


Figure 3-2 (a) Spectrum measurement set-up and spin torque oscillator layer structure. (b) Typical power spectrum with Lorentzian fitting of in-plane angular polarizer fabricated by the electron beam lithography, I=0.3 mA.

## 3.3 Result discussion: spin torque oscillation power angle dependence

Figure 3-3(a) shows the power spectrum under different dc currents. For the 0° polarizer MTJ, the exciting current for the spin oscillation is applied from 0.1 mA to 0.35 mA before reaching its critical switching current 0.38 mA. The power spectral density at the peak increases from 0.0117 nW/GHz to 0.229 nW/GHz due to the increase of the current. For the 30° tilted polarizer MTJ, the peak value of the power spectrum increases from 0.0413 nW/GHz to 0.915 nW/GHz, which is 4 times larger than the maximum peak value of the 0° tilted polarizer MTJ. Since the 60° tilted polarizer MTJ shows a much larger critical switching current compared to the 0° and 30° tilted polarizer MTJs, the dc current can be applied until 0.7mA with the main peak PSD value as 3.90 nW/GHz, which is about 17 and 4 times larger than that of the 0° and 30° tilted polarizer MTJs, respectively. The power spectrum of this 60° tilted polarizer MTJ shows two peaks, which can be tentatively understood by considering the oscillation of the weakly-pinned top layer for this specific sample. In Figure 3-3(b), the frequency decreases with the applied current due to the increase of the precession angle. For the 0° tilted polarizer MTJ, the peak frequency decreases (red-shift) from 2.7 GHz to 2.6 GHz as the current increases from 0.1mA to 0.35mA. The frequency change is 0.13GHz for the 30° tilted polarizer MTJ from 2.56 GHz at I=0.1 mA to 2.43 GHz at I=0.4 mA. For the main peak of the 60° tilted polarizer MTJ, the frequency shows about 0.11 GHz red-shift with the current increasing from 0.1 mA to 0.6 mA. The small red-shift of each sample suggests a small precession angle of the spin torque oscillation and the peak frequency value follows the Kittel

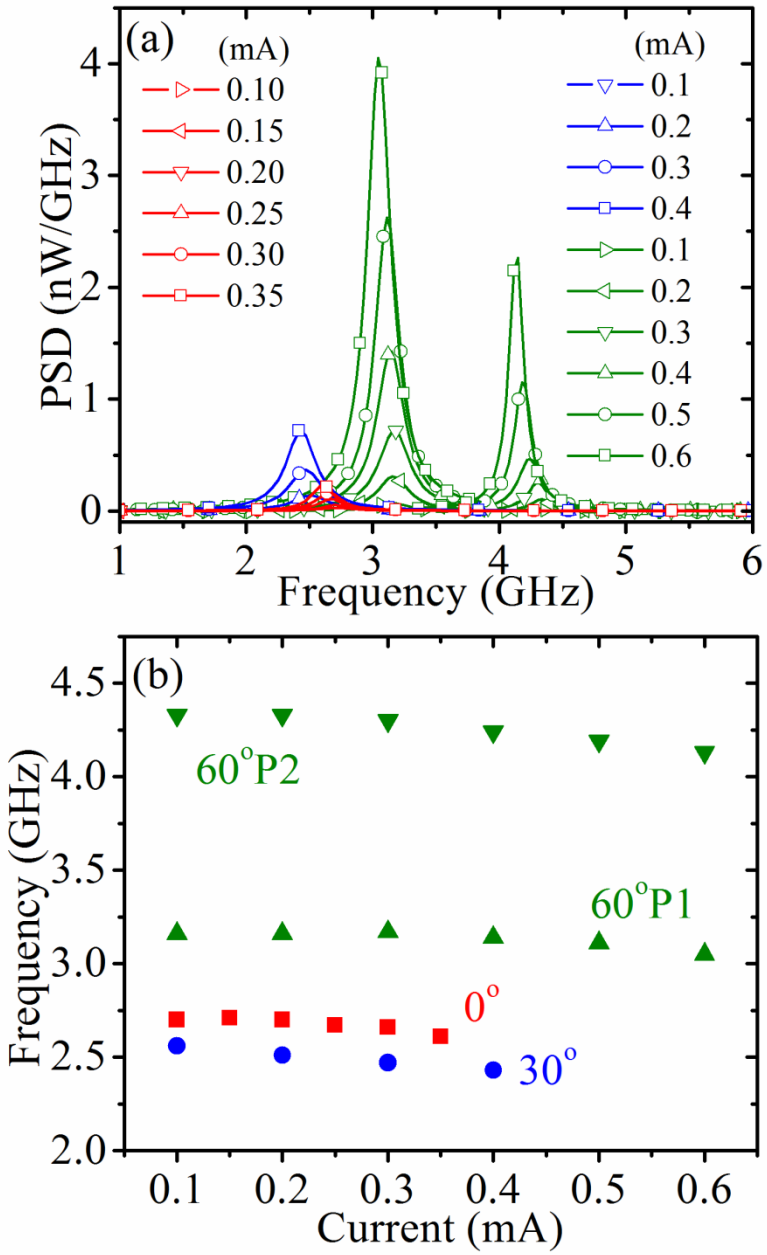


Figure 3-3 (a) The power spectral density of in-plane tilted polarizer angle φ=0° (red), φ=30° (blue) and φ=60° (green) under increasing dc current before switching. (b) The peak frequency change with the current for each angular polarizer. The P1 and P2 represent the first peak and the second peak of the 60° tilted polarizer spectrum respectively.

equation for the small angle precession by considering the coercive field originating from the in-plane anisotropy. So the 30° tilted polarizer MTJ shows the lowest frequency with the smallest coercive field while the 60° tilted polarizer MTJ has the highest frequency.

The power spectral density peak value is plotted versus the applied current in the Figure 3-4(a). The PSD is shown in the log scale since the power increase with the square of the current. The maximum power from the 60° tilted polarizer MTJ is much larger than that of the 0° tilted polarizer MTJ. For the 60° tilted polarizer MTJ, the P1 represents the main peak, which follows the Kittel equation and indicates the oscillation of the free layer. The P2 is named as the second peak which is tentatively considered as the oscillation of the weakly-pinned top layer. Just comparing the main peaks from the oscillation of the free layer, the power spectral density increases with the tilted polarizer angle as shown in Figure 3-4(a). Especially for the 60° tilted polarizer MTJ, the STO exciting current can be extended to a large value[136] to generate higher power compared with the 0° tilted polarizer MTJ that has the similar coercive field. The Figure 3-4(b) shows the power spectral density efficiency of MTJs with different tilted polarized angle. The power spectral density efficiency increases with the applied current due to the increase of the precession angle, which also causes the decrease of the frequency with the applied current as shown in Figure 3-3(b). The trends of the power efficiency with the current are quite different. The 0° polarizer MTJ shows a relevantly flat slop compared to the 60° tilted polarizer MTJ. This trend qualitatively follows the precession angle-power dependence at different tilted angle as discussed in Figure 3-1(b).

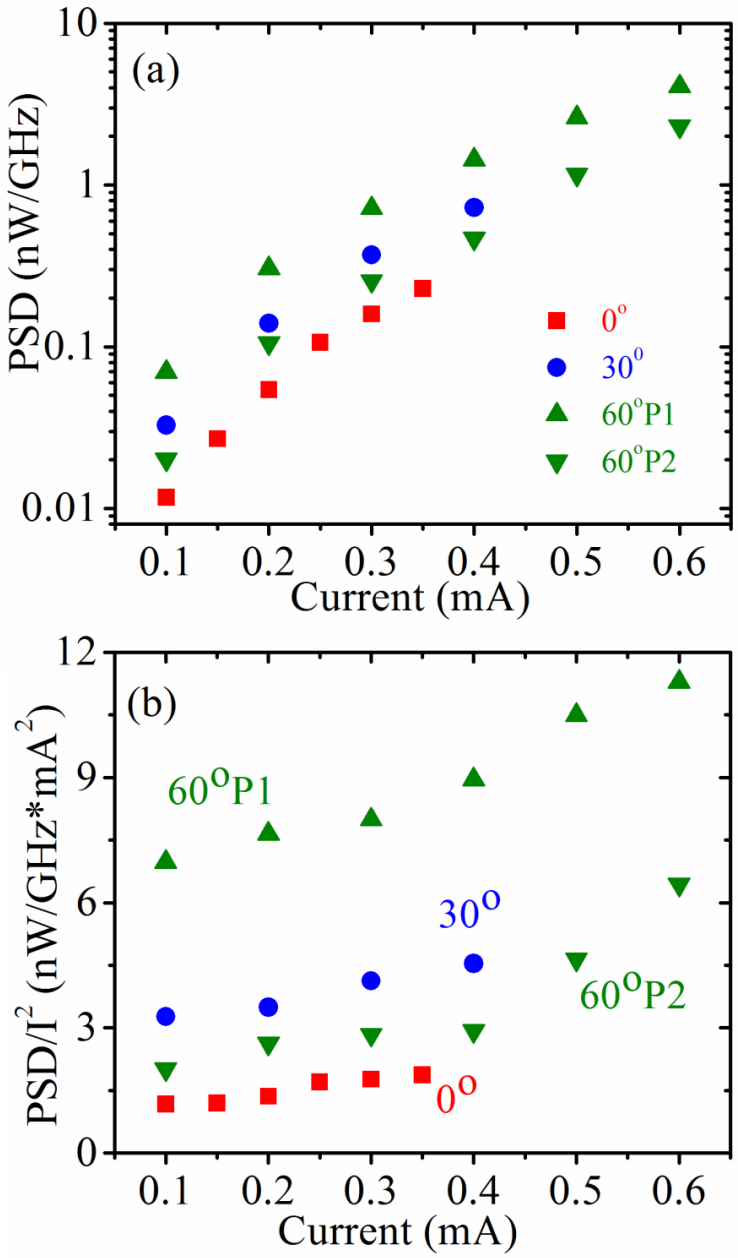


Figure 3-4 The peak value of (a) the PSD and (b) the PSD efficiency of in-plane tilted polarizer angle φ=0° (red), φ=30° (blue) and φ=60° (green) increase with the current.

## 3.4 Summary

In conclusion, we have fabricated bias-field-free STO devices with angular dependent polarizer directly by Electron Beam Lithography and magnetic field post-annealing. We have studied the power of the STO fundamental harmonics as a function of the tilted angle and precession angle. We demonstrated that the STO power increased tremendously with the tilted polarizer angle. In addition, we find that the STO power efficiency trends can be qualitatively fitted with the precession angle power dependence at different tilted polarizer. The current dependence data for each tilted polarizer reveals a potential solution for extending the operating current. Work in this chapter was published on Journal Applied Physics 109, 07C714 (2011) [137].

# Chapter 4. Spin torque oscillator: high power output, low critical current and non-external field

In this chapter, the microwave power and the critical current of spin torque oscillator (STO) devices with a built-in hard axis polarizer have been studied. This design allows for an external-field-free STO. The time domain oscillation signals give direct evidence of higher output from the hard axis polarizer STO, which agrees with spectroscopic results. The hard axis polarizer STO generates a higher power because of the larger slope of the magnetoresistance-angle curve at the lowest energy potential. Furthermore, the hard axis polarizer STO shows a low critical current indicating the large spin torque effect when two magnetic layers are in the 90° configuration.

## 4.1 Introduction

As we already discussed, research on STOs has been focused on several key issues, such as improving the power, narrowing the linewidth, and tuning the frequency through materials engineering and understanding of the fundamental physics. In STT devices, the spin torque vector depends strongly on the angle between the magnetizations of two magnetic layers controlled by the in-plane magnetic field [131]. For STOs, the out-of-plane angle dependence has been theoretically [138] and experimentally [133-134] studied by applying an external field with a perpendicular component, focusing on the

oscillation threshold condition and frequency response. The in-plane angle dependence shows linewidth variations as the applied field is rotated from easy axis to hard axis [114]. However, in this thesis study, an external-field-free STO with higher power and lower critical current will be provided by a large built-in polarizer angle, defined as the angle between the easy axis of the magnetic free layer and the axis of the fixed/polarizer layers in the equilibrium state.

In this chapter, the hard axis polarizer STO (90° built-in polarizer angle) and the traditional easy axis polarizer STO (0° built-in polarizer angle) are developed through lithography and post-annealing of an MgO-based MTJ stack. Both spectroscopic analysis and time-resolved data show a higher power measured from the hard axis polarizer STO. The correlation time at different driving currents demonstrates a lower critical current for the hard axis polarizer STO.

## 4.2 Experiment setup: device annealing and time resolved oscillation measurement

The layer structure of the MTJ is shown in Figure 4-1 (d), as follows: seed layer/PtMn (15) /$Co_{70}Fe_{30}$ (2.5) /Ru (0.85) /$Co_{40}Fe_{40}B_{20}$ (2.4) /MgO (0.9) /$Co_{60}Fe_{20}B_{20}$ (1.8) /capping layer, where the thicknesses in parentheses are in nm. The wafer was annealed at 300°C in a 1 Tesla magnetic field for 2 hours. The STOs were patterned by electron beam lithography into 165nm×65 nm ellipses with the long axis along the annealing direction. This annealing process leads to traditional memory type MTJs with the polarizer along the free layer easy axis, defined as easy axis polarizer STO in this letter. This sample

presents typical easy and hard axis loops as shown in Figure 4-1 (b). The MR ratio for this sample is about 139%. Another set of the samples from the same wafer were annealed at 300°C in a 5000 Oersted in-plane magnetic field along the short axis of the ellipses. After annealing, the easy axis (red solid curve) and hard axis (blue dashed curve) loops are shown in Figure 4-1(a) while a typical easy axis loop before annealing is shown as the black dash-dot curve. This annealing process made sensor type MTJs with the polarizer along the hard axis of the free layer, defined as hard axis polarizer STO in this letter. Figure 4-1(c) shows the fitted spectra of both hard axis polarizer (blue solid curve) and easy axis polarizer (red dashed curve) STOs, normalized by the amplifier gain. Due to the different magnetization configurations of the polarizer layers, the two spectra show remarkably different output power with similar frequency and linewidth. The power spectra and time domain measurement setups are shown in Figure 4-1(d), and the positive current is defined from top to the bottom. The signals from the MTJs were transferred by the microwave probe and then amplified by +30 dB with the dc component being filtered by a bias tee. The 50 ohm coupled HP 8593A series spectrum analyzer and Tektronix DPO72004B digital oscilloscope were used to collect the microwave signals at room temperature.

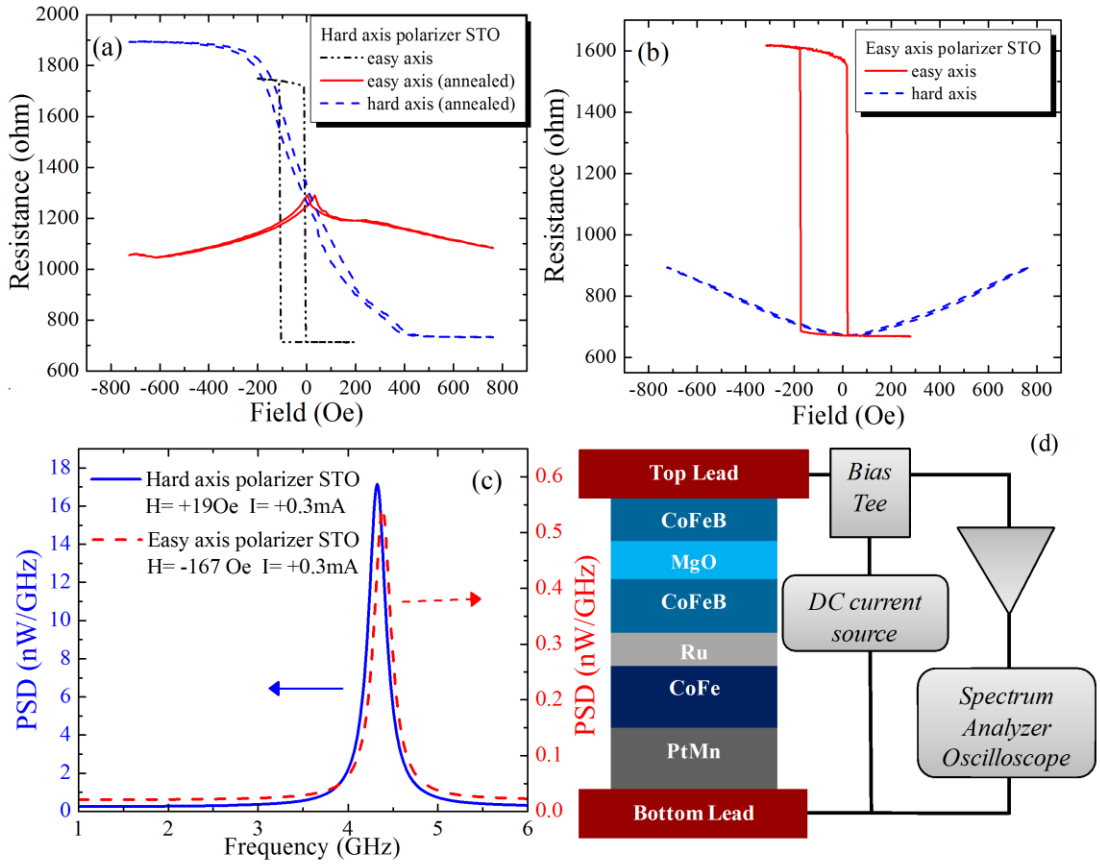


Figure 4-1 (a) The hysteresis loops of the hard-axis polarizer STO. The black dash-dot curve is the easy axis loop before annealing the sample. The red solid curve and blue dashed curve are the easy and hard axis loops respectively after annealing. (b) The hysteresis loops of the easy axis polarizer STO. The red solid curve represents the easy axis loop, while the blue dashed one is the hard axis loop. (c) A fit of the typical power spectra of the hard axis polarizer STO (blue solid curve) and easy axis polarizer STO (red dashed curve). (d) A schematic of the layer structure of both STOs along with the setup for frequency and time domain measurement.

## 4.3 Result discussion: high power, low critical current and non-external field oscillator

The field-dependence was measured with magnetic fields applied along the easy axis and is shown in Figure 4-2(a) and (b) for the hard and easy axis polarizer STOs, respectively. In Figure 4-2(a) and (b), the blue dots show the frequency field-dependence and the red triangles represent the power spectral density (PSD) peak value under dc driving currents I= +0.3 mA (solid) and I= -0.3 mA (hollow). For the hard axis polarizer STO, the highest power with the lowest frequency was observed near zero external fields. Due to the increase of the total effective field, the frequency increases and the PSD peak value decreases with the external field along the easy axis direction. This trend was observed for both positive and negative currents. Due to the reduction of the polarization ratio under a positive bias-voltage on the bottom polarizer layer [55], lower power and higher frequency were observed under negative current, shown in Figure 4-2(a) as hollow red triangles and hollow blue circles. However, for the easy axis polarizer STO, the positive or negative current forces the free layer to be either parallel or anti-parallel to the easy axis polarizer layer. In this case the free layer will prefer to remain in an equilibrium state rather than oscillate unless an external field is applied to prevent the rotation of the easy axis magnetization. In Figure 4-2(b), the spin torque oscillation occurs under two conditions: (1) when applied field drives the free layer to P state ($H_0$ > -100 Oe) and current drives it to AP state (negative current), (2) when the applied field drives the free

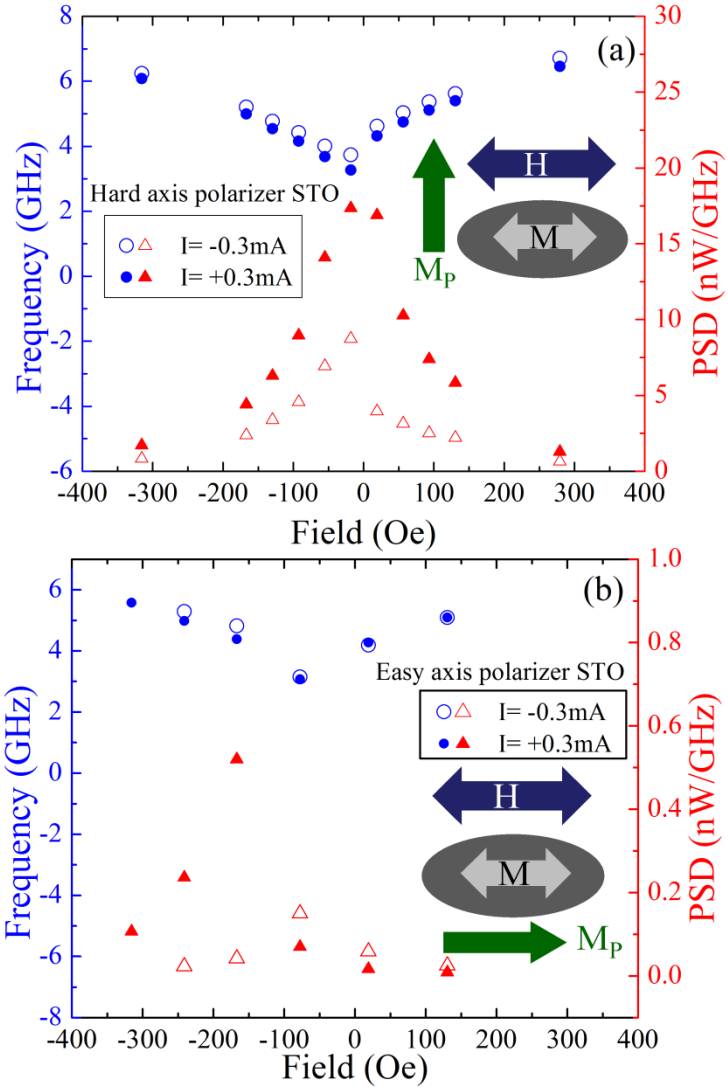


Figure 4-2 Frequency and power spectral density (PSD) as functions of the external fields along the easy axis for both (a) hard axis polarizer STO and (b) easy axis polarizer STO. The solid and hollow blue circles denote the frequency values for I = +0.3 mA and I = -0.3 mA dc current. The solid and hollow red triangles denote the peak value of power spectral density at I = +0.3 mA and I = -0.3 mA dc current.

layer to AP state ($H_0$ < -100 Oe) and current drives it to P state (positive current). The signals can be considered as thermally excited ferromagnetic resonance (TE-FMR) for the other two conditions: (1) positive current applied to P state and (2) negative current applied to AP state. This is because the ordinary Landau–Lifshitz–Gilbert damping vector introduced by field and the STT vector due to the current point in the same direction. The field-dependence data for both STOs therefore suggest that the hard axis polarizer STO gives a more predictable range of fields for spin torque oscillation.

The oscillation signals for the easy axis polarizer STO show a maximum peak value of 0.54 nW/GHz at 4.38 GHz with H = -167 Oe and I = +0.3 mA. However, the signal from the hard axis polarizer STO, with H = +19 Oe and I= +0.3 mA, shows 17.4 nW/GHz as the PSD peak value at 4.2 GHz. The power spectra of these two signals are shown in Figure 4-1 (c). Their real time traces are shown in Figure 4-3(a) correspondingly. The data were collected by a digital oscilloscope with a 50 Gs/s sampling rate and normalized with the respect of the 30 dB gain. A FFT band pass filter (2 GHz - 8 GHz) was applied to the collected traces. Figure 4-3 (b) and (c) show the amplitude envelope histograms of the hard and easy axis polarizer STOs, respectively. The upper and lower envelopes show similar distribution and the same absolute mean value, as expected for both the hard and easy axis polarizer STOs. The mean voltage output of the hard axis polarizer STO is $\pm$0.34 mV while the easy axis polarizer STO generates an average $\pm$0.077 mV output. The amplitude difference shows that the voltage output from the hard axis polarizer STO is higher than the one from the easy axis polarizer STO.

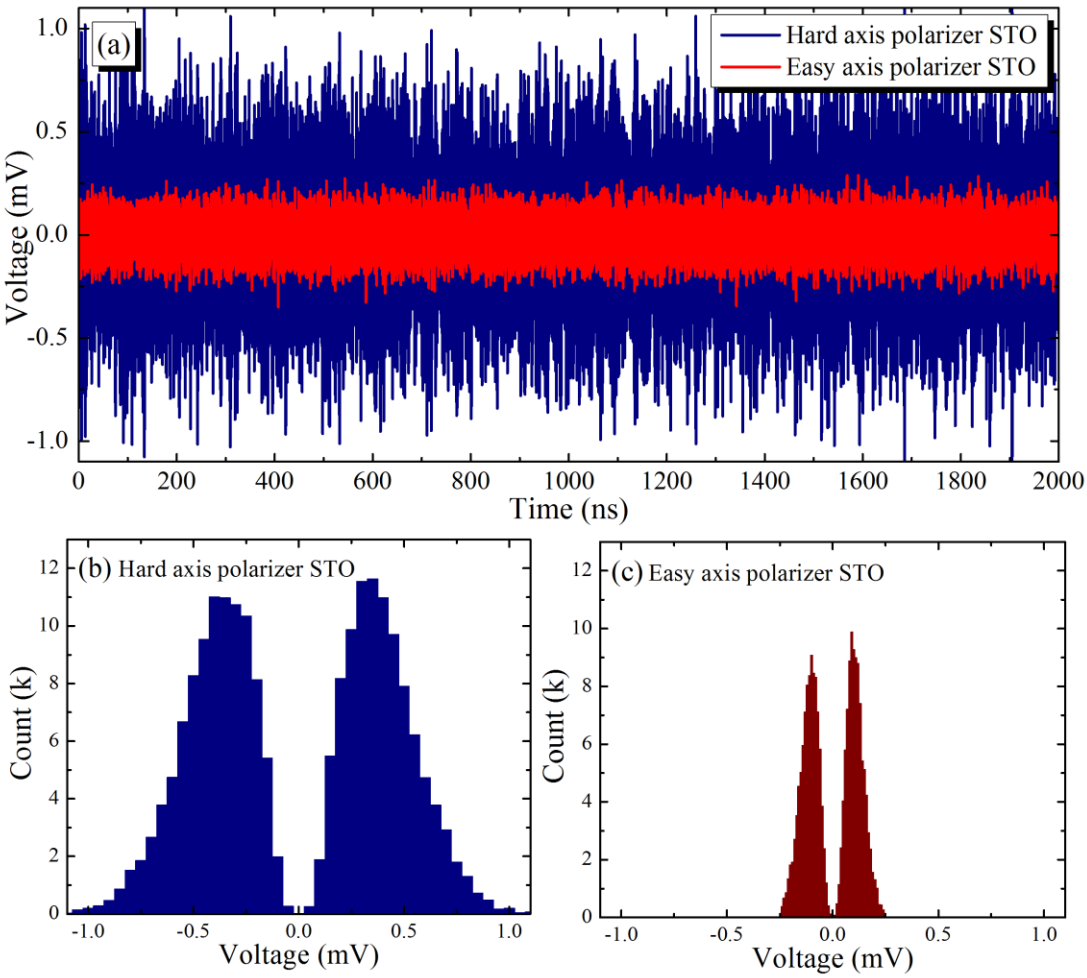


Figure 4-3 (a) The blue and red curves show real time traces of the output of the hard axis polarizer STO (with H = +19 Oe and I = +0.3 mA) and easy axis polarizer STO (with H = -167 Oe and I = +0.3 mA). Histograms of the positive and negative signal envelopes of (b) hard axis polarizer STO and (c) easy axis polarizer STO.

The current-dependences of both hard and easy axis polarizer STOs were analyzed at the external fields used for the data in Figure 4-1(c) and Figure 4-3(a) and (b). The envelope of the waveform autocorrelation function decays with a time constant $\tau_c$, which can be used to determine the linewidth as $\Delta f = 1/\pi\tau_c$. For the easy axis polarizer STO shown in Figure 4-4(b), the linewidth decreases with the current and levels off for currents above +0.3 mA. The free layer is switched with the current greater than +0.4 mA. The linear decrease of the linewidth suggests the transition from a thermally excited ferromagnetic resonance to a relatively stable oscillation due to the larger spin torque effect at larger injection dc currents. A linear fit is shown as the red solid line in Figure 4-4(b). The extrapolation of the linear fit to zero current gives an intrinsic linewidth, about 1.7 GHz, indicating a damping constant of about 0.04 for an Ms of 1200 emu/cc. The higher damping constant might be introduced by the inhomogeneous magnetization in the nano-scale ellipsoid and the edge roughness caused during the etching process. However, the linewidth current-dependence curve of the hard axis polarizer STO shows a very different trend, shown in Figure 4-4(a). By assuming the similar damping constant for both STOs, the blue dashed line can be considered as the linear region of the hard axis polarizer STO. The critical current is less than +0.1 mA, resulting from the large spin torque effect with the 90° magnetic configuration between the free and polarizer layers in the magnetic tunnel junction. The increase of the linewidth at high current is due to heating which introduces more amplitude and phase noise.

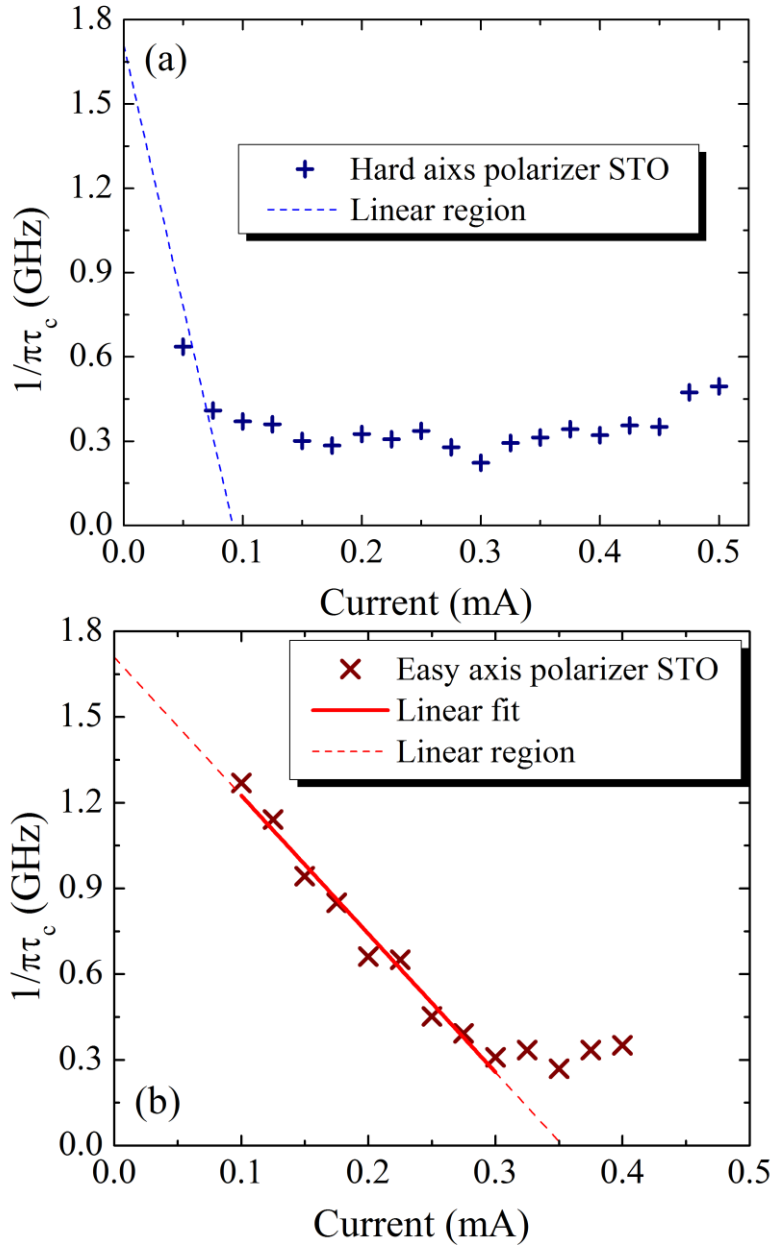


Figure 4-4 The linewidth, as measured by the inverse of the correlation decay time constant, as a function of the external dc current for (a) the hard axis polarizer STO and (b) the easy axis polarizer STO.

## 4.4 Summary

In summary, we have fabricated an external-field-free STO with a hard axis polarizer having a 90 degree configuration relative to the easy axis of the free layer by using both lithography and post-growth annealing processes. We have observed a much higher microwave output from the hard axis polarizer STO as measured by both the time-domain voltage signal and spectroscopic power. Furthermore, the hard axis polarizer STO shows a lower critical current, due to much more efficient spin torque in the 90 degree configuration of the free and polarizer magnetic layers. Work in this chapter was published on Applied Physics Letter 100, 032405 (2012) [139].

# Chapter 5. STO modes in dual magnetic tunneling junction with single free layer

In this chapter, two coexisting spin torque oscillation (STO) modes in dual magnetic tunnel junctions (MTJs) with MgO barriers are observed by measuring the field-dependent power spectra. The frequency-field relation of the main STO mode is found to follow the Kittel equation at both positive and negative fields applied along the easy axis, which is consistent with spin torque oscillation of the magnetic free layer between the two MgO barriers. The second oscillation mode shows a different frequency-field relation for positive and negative applied fields, which is tentatively understood by considering the oscillation of the weakly-pinned top layer.

## 5.1 Introduction

A great deal of attention has been paid to the key engineering challenges, such as increasing output power, reducing the line width, and also broadband tuning of the oscillation frequency. Meanwhile, understanding the spin oscillation modes and their relationship to the micromagnetic configuration and layer structure of a particular device is also critical. For example, the inhomogeneous magnetic configuration of an STO device due to geometric confinement is expected to influence its spin dynamics [140]. This effect has been observed in power spectrum measurements on MgO-barrier magnetic tunnel junctions (MTJs) [117], [141], which show a double-mode structure similar to that seen in ferromagnetic resonance measurements on simple nanomagnet

arrays [142]. On the other hand, most functional STO devices have a more complicated layer structure, and their dynamical properties can be influenced by coupling between different magnetic layers. Several coupling mechanisms have been explored, such as 1) the RKKY interlayer exchange, as in a typical synthetic anti-ferromagnetic (SAF) pinned layer [143-144] of a GMR spin-valve or MTJ spin torque oscillator; 2) the dipolar interactions in a ferromagnet/normal metal/ferromagnet sandwich structure [145], and 3) the dynamic exchange coupling due to spin pumping [146].

In this chapter, the STO modes in a dual MTJ with MgO barriers are studied experimentally by analyzing its power spectra at different applied fields and bias currents. Two different oscillation modes showing different field and frequency dependences are observed due to the unique layer structure. Oscillations of both the free layer and the weakly-pinned top layer, in combination with some coupling between them, are necessary to explain the observed results.

## 5.2 Experiment: device description and measurement

The layer structure of the dual MTJ is as follows: seed layer/PtMn (20) /$Co_{70}Fe_{30}$ (2.5) /Ru (0.85) /$Co_{40}Fe_{40}B_{20}$ (2.4) /MgO (0.82) /$Co_{60}Fe_{20}B_{20}$ (2.0) /MgO (0.8) /$Co_{40}Fe_{40}B_{20}$ (2.4)/PtMn (20)/ capping layer, where the thicknesses in parentheses are in nm. In order that the two pinned layers produce similar spin transfer torques acting on the middle free layer, they are required to have opposite magnetizations. To provide the two different pinning directions, we incorporate the bottom pinning layer into a SAF. After the sample is annealed at 300°C in a 1 Tesla magnetic field for 2 hours, the top $Co_{40}Fe_{40}B_{20}$ layer

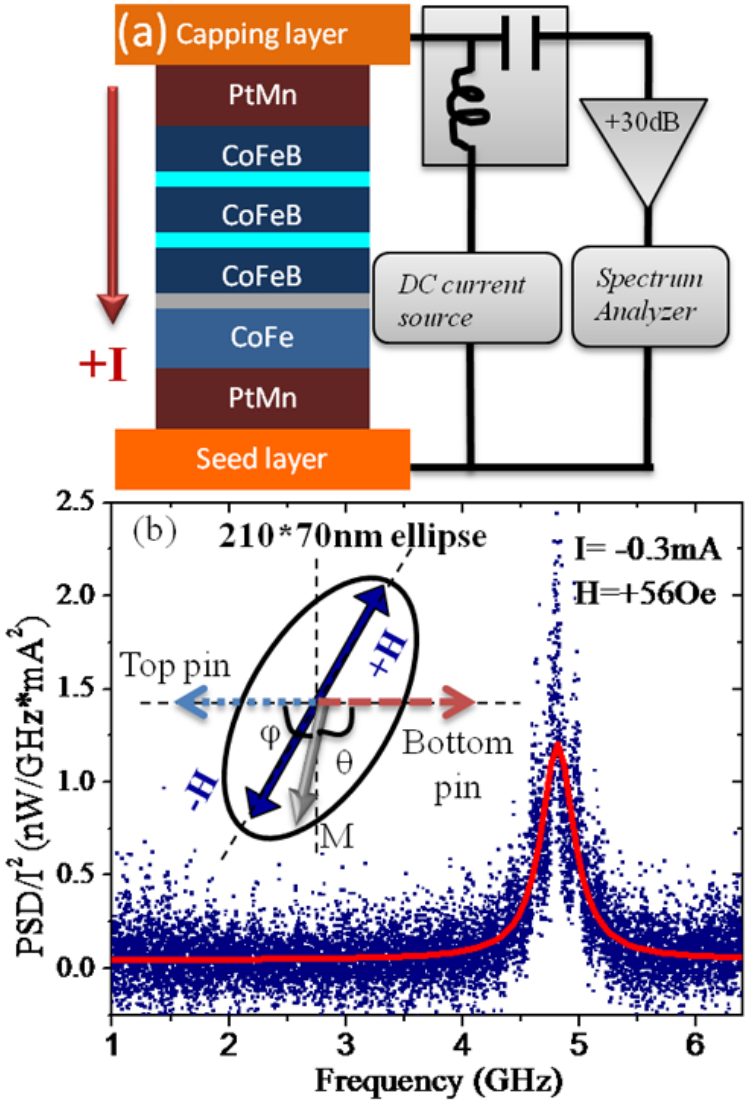


Figure 5-1(a) A schematic of the layer structure of the dual MTJ (see text for an identification of all layers) along with the power spectrum measurement setup. (b) A typical power spectrum with Lorentzian fitting (red line). The inset of (b) shows the geometrical relationships between the shape anisotropy easy axis, the external field, and the top and bottom pinning directions.

points to the left while the bottom $Co_{40}Fe_{40}B_{20}$ pinned layer points to the right, as indicated in Figure 5-1(b). The dual MTJ wafer was patterned by the electron beam lithography into 210 × 70 nm ellipses, with the major axis of each ellipse 60° away from the pinning direction. A hysteresis loop, measured with the applied field along the major axis, is shown in Figure 5-3(c), in which the field directions correspond to those defined in Figure 5-1(b). Although the dual pinned structure with opposite pinning directions is designed to increase the spin transfer torque, the tunneling magnetoresistance ratio (TMR) from the top and bottom junctions will cancel each other if they are completely symmetric. We therefore designed the two junctions with slightly different MgO thicknesses. The resulting dual MTJ shows a net TMR of 16%, with the resistance changing from 512 to 594 Ohm at the center of the hysteresis loop, at which the applied field is -30 Oe. The coercive field is 60 Oe. The power spectrum measurement setup is shown in Figure 5-1(a), which indicates the sign convention for the applied current. All measurements were carried out at room temperature. The oscillation signal from the dual MTJ was collected by a microwave probe and then amplified by +30 dB after removing the dc component with a bias tee. A typical power spectrum, normalized by the amplifier gain, and with the zero-bias background subtracted, is shown in Figure 5-1(b). The solid curve shows a Lorentzian fit of the raw data, and similar fits will be used for showing the subsequent experimental results in this paper.

## 5.3 Result and Discussion: field dependence

The power spectra data were measured with applied field from -687 Oe to 650 Oe. Results for the cases with ±0.3mA ($J=\pm 2.6\times10^{6}$ A/cm$^2$) dc current of are shown in Figure

5-2(a)-(d). For the data shown in Figure 5-2(a), the field was increased from -92 Oe to -687 Oe in steps of 75 Oe at a constant dc current of -0.3 mA. Two modes are observed in the spectra. The frequency of the main peak (larger amplitude at low fields, identified with red arrows) has a field dependence which follows the Kittel equation, as shown by the fits in Figure 5-3(a) and (b), which shows the observed mode frequencies as a function of magnetic field. The frequency of the second peak (identified with blue arrows) shows a very different field dependence, and this mode actually crosses through the main mode as the magnetic field is varied. Similar frequency-field behavior is also observed for +0.3 mA dc current at negative fields, as shown in Figure 5-2(c). For positive fields, the data for which are shown in Figure 5-2(b) and (d), the field dependence of the frequency for the main mode is essentially identical to that observed in negative fields. The second peak, however, is more prominent at larger positive fields, although it was not resolved in low fields. The frequency-field relations for the spectra in Figure 5-2 are plotted in Figure 5-3(a) and (b) for I=+0.3mA and I=-0.3mA with the full width at half-maximum (FWHM) shown as the error bars. For the purposes of discussion, we will consider five different magnetic field regimes, labeled in all panels of Figure 5-3, and we will make several assumptions: (1) the bottom layer is strongly pinned along the direction of the red dashed arrows in Figure 5-3(c); (2) the top layer, for which the orientation is shown as the light blue dotted arrows in Figure 5-3(c), is weakly pinned, with an easy axis between the pinning direction of the bottom layer and the long axis of ellipse; and (3) there is some dipolar coupling between the free layer and the top layer. $\theta$ is defined as the angle between the free layer and the bottom pinned layer, while $\varphi$ is the angle between

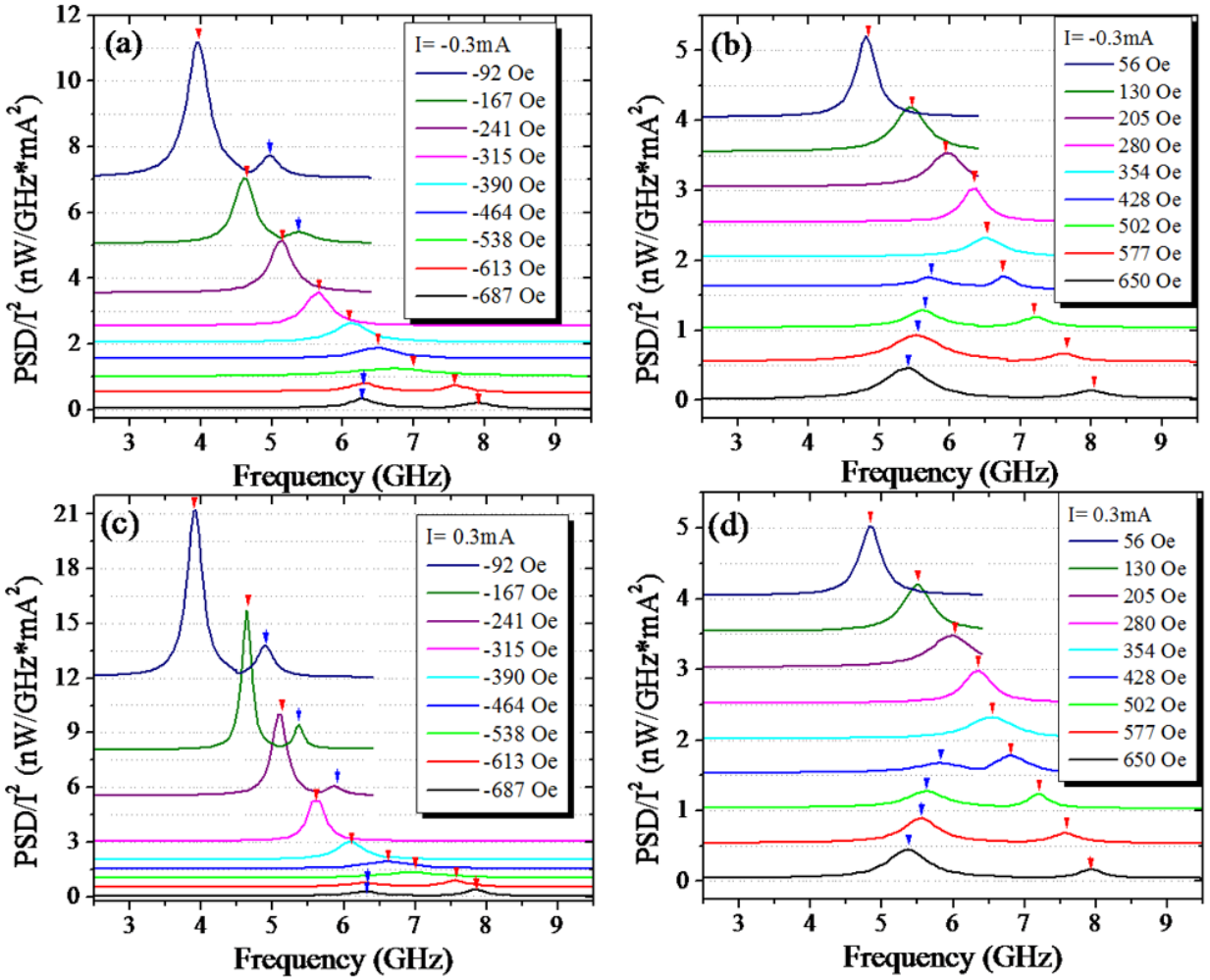


Figure 5-2 The power spectra of the dual MTJ STO device with (a) I=-0.3mA, negative external field, (b) I=-0.3mA, positive external field, (c) I=0.3mA, negative external field and (d) I=0.3mA, positive external field. The convention for the magnetic field direction is shown in Figure 5-1(b).

the free layer and the top layer, as shown in Figure 5-1(b). In the quasi-parallel (quasi-P) state (regions I-II), $\theta$ is between 0 and $\pi/2$, and this corresponds to the low resistance state. In the quasi anti-parallel (quasi-AP) state (regions III-V) $\theta$ is between $\pi/2$ and $\pi$, and this corresponds to the high resistance state.

For the quasi-P state, the increase of resistance with the applied field along the easy axis can be explained by the coherent rotation of the free layer, as shown schematically in regions I and II of Figure 5-3(c). At zero field, the free layer is pulled away from the easy axis by the dipolar field of the top layer. As the field increases, both the free layer and the weakly-pinned top layer rotate towards the magnetic field as shown in regions I and II of Figure 5-3(c). In this case, $\theta$ increases towards 60° (the angle between the applied and pinning fields) while $\varphi$ decreases towards $\pi/2$. This is consistent with the increase of the resistance with increasing field in the quasi-P state. This hypothesized field dependence of the orientations also explains the observed decrease of the frequency of the $2^{nd}$ mode in this regime, since it is being rotated away from its own easy axis. This is similar to the case of ferromagnetic resonance of a uniaxial system for fields applied along the hard axis. We also emphasize that as $\varphi$ approaches $\pi/2$, the spectral power of the $2^{nd}$ mode should increase, as is observed experimentally in Figure 5-2(b) and (d).

For the quasi-AP state, regions III-V of Figure 5-3(c), the resistance increases at low fields due to the rotation of the free layer, and then saturates in region IV when the free layer is completely aligned. At higher fields, the resistance decreases slightly because the top layer rotates towards the field, reducing the total resistance. In this quasi-AP state, the angle between the top layer and the field is small, which is why no significant decrease of

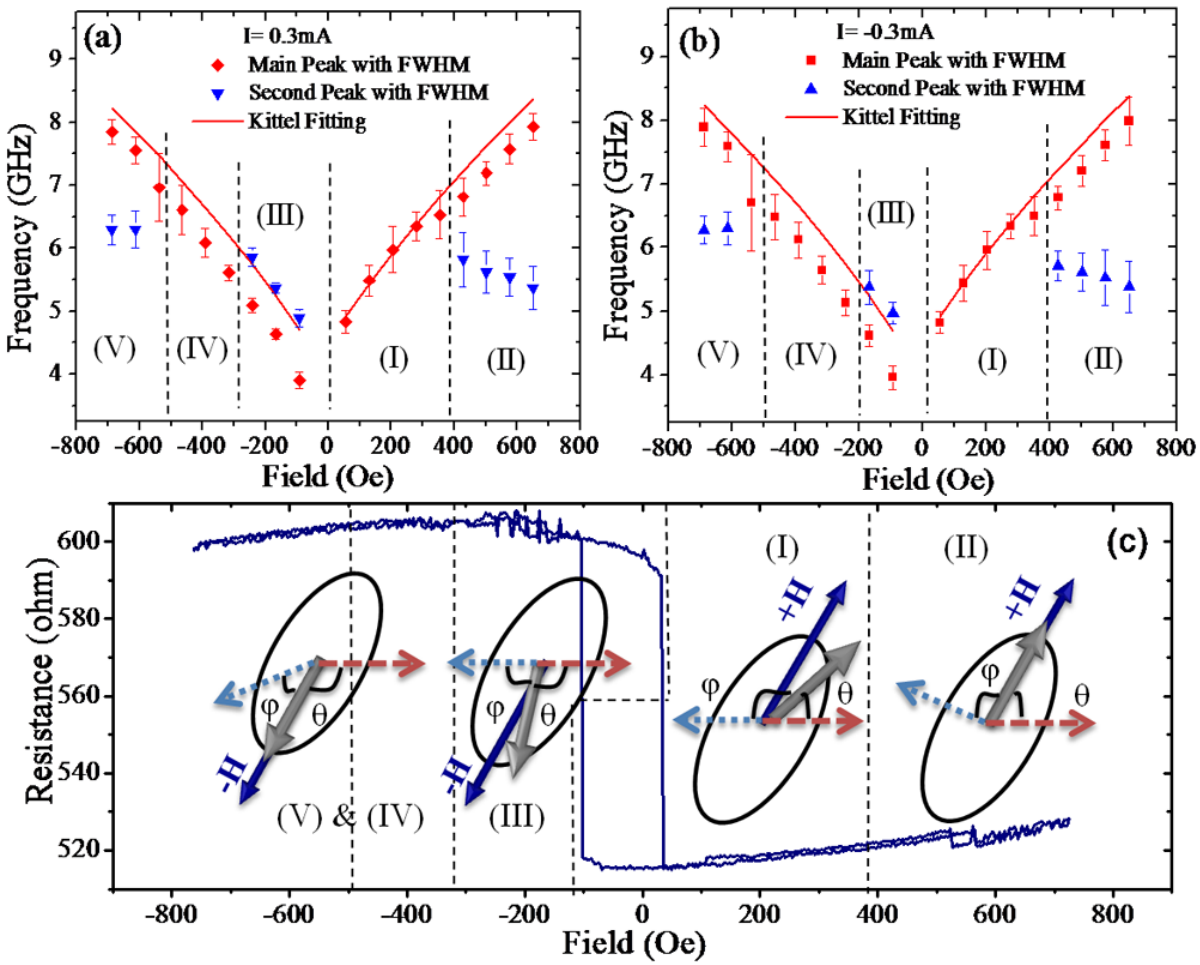


Figure 5-3 Frequency as a function of magnetic field for both m odes for dc currents of (a) I = +0.3mA and (b) I = -0.3mA. (c) The hysteresis loop as a function of the field applied along the easy axis, which is the major axis of the ellipse. The insets show the hypothesized magnetization configurations in each layer for the five different field regimes. The solid blue arrow indicates the direction of the magnetic field. The gray arrow indicates the orientation of the free layer. The red dashed and light blue dotted arrows indicate the orientations of the bottom layer, which is strongly pinned, and the top layer, which is weakly pinned.

the frequency is observed in high fields. More quantitative discussion, including micromagnetic simulation, is required to confirm this proposed model. In particular, we have not addressed the possibility that a non-uniform magnetization configuration in the free layer could be responsible for the second mode.

## 5.4 Summary

In summary, we have studied the spin torque oscillation modes of a dual MTJ with MgO barriers. We have observed two distinct modes, the frequencies of which cross with applied field. Although one of the modes appears to be the ordinary Kittel mode of the free layer, the other shows markedly different dependences for opposite directions of the applied field. This leads us to propose that the second mode is due to oscillation of the top layer, which is not strongly pinned. Work in this chapter was published on Journal Applied Physics 109, 07D307 (2011) [147].

# Chapter 6. Switching Time Distribution in Magnetic Tunnel Junction by Single-Shot Time Domain Analysis

In this chapter, the distribution of the switching time in magnetic tunnel junctions has been experimentally investigated for the precessional switching regime. The switching time variation coefficient, defined as the switching time distribution divided by the mean of the switching time, was found to be a constant, 0.38, for both parallel to anti-parallel and anti-parallel to parallel switching in the precessional switching regime. The mean and distribution of the switching time were characterized by collecting and analyzing single-shot time domain switching events within 10 ns under different pulse amplitudes. The real time switching events and switching probabilities were mapped in a voltage-time phase diagram.

## 6.1 Introduction

Spin transfer torque as been studied intensively in the graint magnetoresistance spin valve (GMR-SV) and magnetic tunneling junction (MTJ) due to its promising applications such as non-volatile STT random access memory (STT-RAM). The cirtical current required for the switching of the magnetic free layer in the MTJ and GMR-SV devices has been a key research topic since the STT magnetizaion swithing was first demostrated by Tsoi er al., [43] Myers et al. [44] and Sun [45]. The microspin model [63]

suggested that enforcing of the switching time reduction would result to an excessive current for the switching. Studies of the the switching probability supported this inverse relation between the switching cirtical current and switching time, and it is also obseved that the switching currents distributed at the same switching time or pulse width [64]-[148]. Furthermore, the switching time distribution was experimentally studied by X. Wang et al. in millisecond regime, showing that the swithcing time variation coefficient, defined as the ratio between the distribution and the mean value of the switching time, was a constant, one [149]. Micromagnetic modeling suggested that the switching time variation coefficient started to decrease from one, when the switching happened faster than millisecond [149-150]. However, there is no experiemntal report so far on the switching time variation coefficient when the switching is approching to the precessional switching regime in which magnetization switching happens in nanosecond time-scaled. In this work, we have experimentally investigated the switching time variation coefficient in the processional switching regime uisng MTJs with MgO barrier. We found it approaches to a constant, 0.38, for both anti-parallel (AP) to parallel (P) and P to AP switching.

## 6.2 Experiment: device description and single-shot time domain switching measurement

The device structure is shown in Fig. 1(a), as follows: seed layer/PtMn (15) /$Co_{70}Fe_{30}$ (2.5) /Ru (0.85) /$Co_{40}Fe_{40}B_{20}$ (2.4) /MgO (0.9) /$Co_{20}Fe_{60}B_{20}$ (1.8) /capping layer, where the thicknesses in parentheses are in nm. The film was annealed at 300°C in a 1 Tesla in-

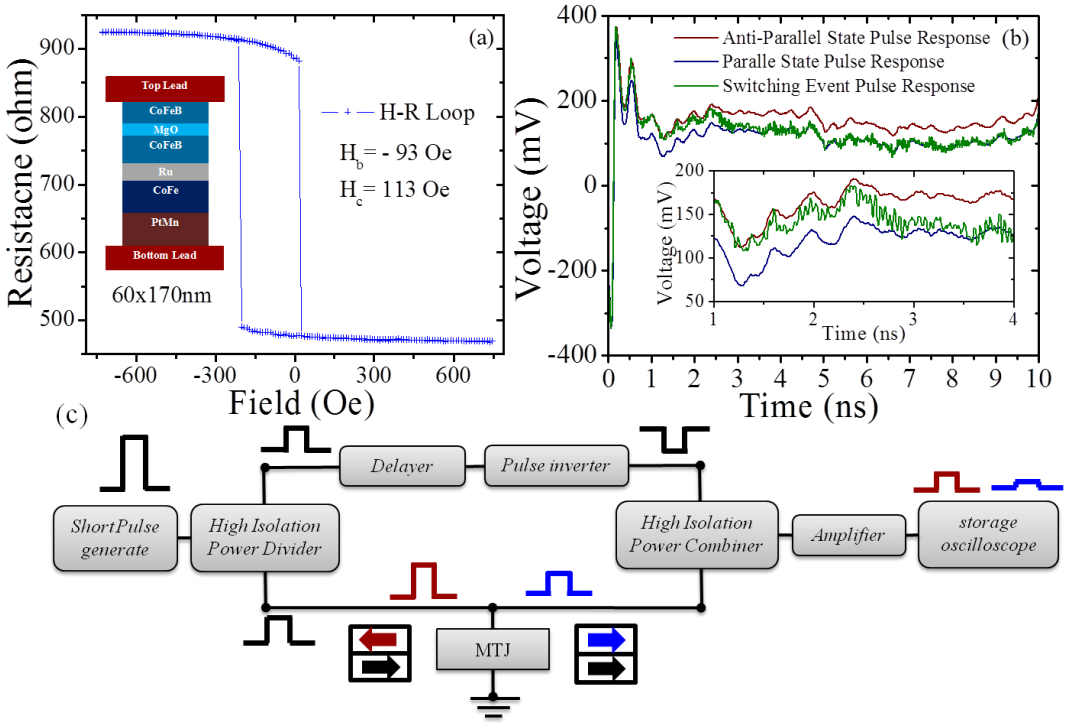


Figure 6-1 (a) The resistance-field hysteresis loop with the magnetic field along the easy axis. (b) The schematic of the measurement circuit and setup. (c) The time-resolved pulse responses of the magnetic tunneling junction at anti-parallel state (red line), at parallel state (blue line) and during the single-shot switching (green line).

plane magnetic field for 2 hours. The elliptic pillars were patterned by the electron beam lithography process into 170 × 60 $nm^2$ with the long axis along the annealing direction. A typical resistance-field hysteresis loop is shown in Figure 6-1 (a), with tunneling magnetoresistance ratio (TMR) about 88%, coercivity $H_c$=113 Oe and offset field $H_{off}$=-93 Oe. Both AP to P and P to AP switching behavior were tested under an applied field (-93 Oe) to center the loop. A single-shot time-domain measurement method [83-84, 86, 151] was adopted in this work. Our single-shot time domain measurement setup is shown

in Figure 6-1 (b). A 10 ns pulse was sent by the pulse generator and split into two pulses by a high isolation power divider. One pulse $V_0$ was sent to the MTJ and another identical pulse was flipped by a pulse inverter as Vr. The pulse response from the MTJ is $V(t)=V_0*\tau(t)$, where $\tau(t)=(1-50/(2*R(t)+50))$ is the transmission coefficient. The resistance of the MTJ, R(t), is in the range of 480 Ω (P state) and 904 Ω (AP state). Therefore the transmission coefficient τ(t) is between 0.9505 (P state) and 0.9731 (AP state), which is very close to 1. The small change of τ(t) between P and AP states can only provide a small variation of the pulse response V(t) comparing to the input pulse $V_0$. In order to improve the voltage resolution, an inverse constant pulse Vr was subtracted from V(t) by a high isolation power combiner. The pulse delayer aligns the phase difference between the Vr and V(t). The small variation of the pulse response between the P and AP states, therefore, can be amplified (+18dB) and detected by the storage oscilloscope with 50Gs/s sampling rate at room temperature. Figure 6-1 (c) shows a typical dynamic trace collected by the storage oscilloscope during the AP to P switching (green, $V_S$) under +344 mV pulse amplitude on MTJ. As references, the static traces for stable AP (red, $V_{AP}$) and P (blue, $V_P$) states are 100 times averaged traces at ±600 Oe magnetic fields and +344 mV pulse amplitude. The dynamic trace was normalized by $(V_S-V_P)/(V_{AP}-V_P)$ and the middle point was collected as the switching time for each single shot pulse. For statistical analysis, 1000 dynamic traces were collected at the same pulse amplitude to find the switching probability, switching time distribution and switching time variation coefficient.

## 6.3 Result and discussion: switching time distribution and variation coefficient

By cumulatively counting the switching events by a 200 picoseconds time step for each applied voltage, the voltage-time phase diagrams for cumulative switching events (switching probabilities) of both AP to P and P to AP are shown in Fig. 2(a) and 2(b), respectively. In Figure 6-2 the blue represents P state and the red denotes AP state. The triangles indicate the 50% switching probability points under different pulse voltages. These points were fit by the switching voltage versus time inverse function (dash line) to find the critical switching voltages according to the micro spin model [63]. The critical switching current densities for both AP to P and P to AP switching were determined as $J_0^{AP-P}$= $2.3\times10^6 A/cm^2$ and $J_0^{P-AP}$= $-5.2\times10^6 A/cm^2$ based on the tested device size and resistances at AP and P states. Furthermore, the voltage-time phase diagrams for switching events of both AP to P and P to AP were mapped by directly counting the switching events at a 200 picoseconds time step for each applied voltages, as shown in Figure 6-3 (a) and (b). This mapping not only gives the voltage distribution of the switching events, but also shows the time distribution of the switching events. It is noticed that the switching events show a wide distribution in the low voltage regime while a narrow distribution in the high voltage regime. Since the switching voltage is inversely proportional to the mean switching time, the switching time distribution is believe to decrease with the switching time in the precessional switching regime.

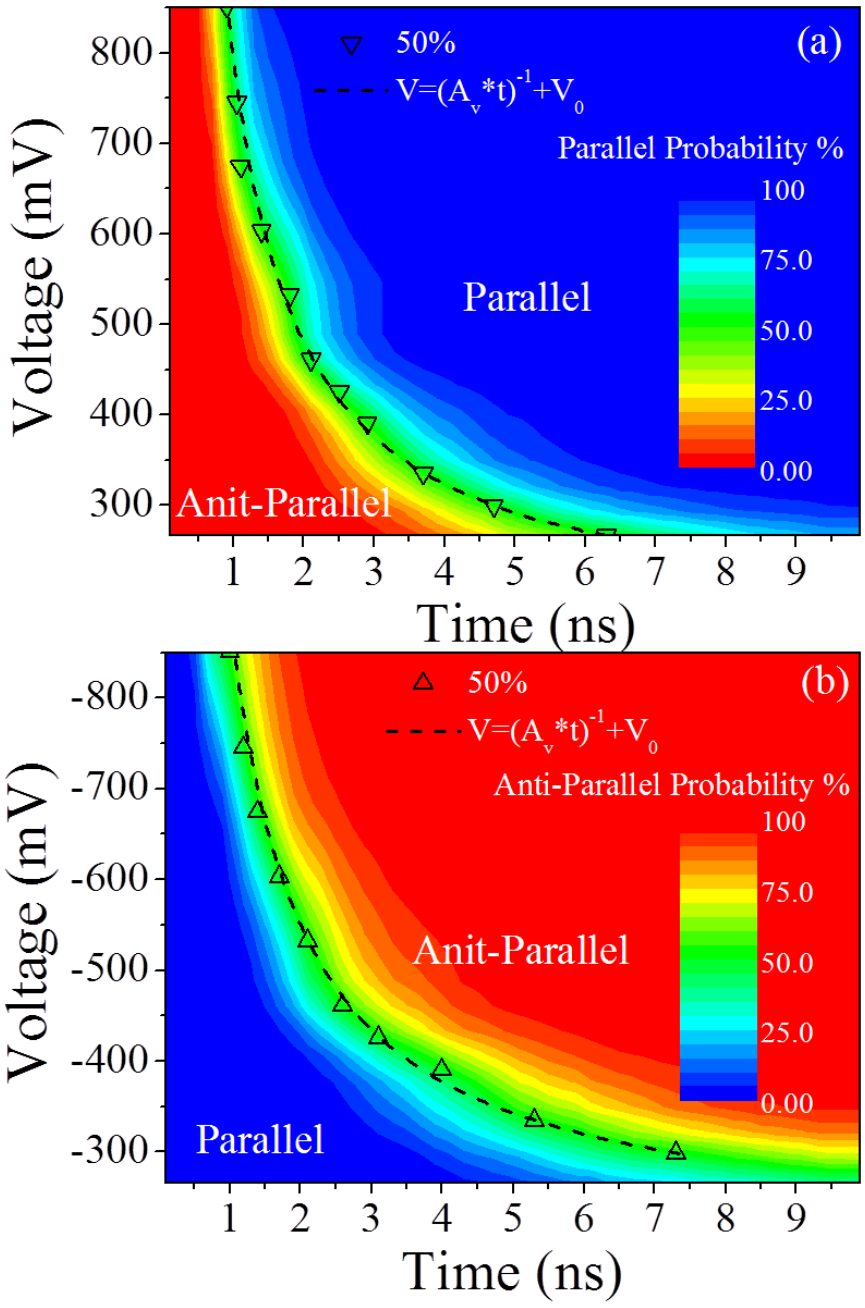


Figure 6-2 The time-voltage phase diagrams of the switching probabilities for (a) anti-parallel to parallel and (b) parallel to anti-parallel. The triangles represent the 50% switching probability points at different voltages with the fitting curve (dash lines).

To find out the switching time distribution vs. the mean switching time and voltage, the switching time distribution function needs to be fit for each applied voltages. Figure 6 4 (a) and (b) show the switching time distribution under three different voltages for both AP to P and P to AP switching. The bars represent counts of the switching happened in every 200 picoseconds. The log-normal function is applied to fit the switching time distribution at different voltages for both AP to P and P to AP switching. The fittings are shown as lines in Figure 6 4 (a) and (b). The mean switching times for AP to P under pulse amplitudes 298 mV, 461 mV and 851 mV are 4.66 ns, 2.09 ns and 0.97 ns, respectively. The switching time distribution decreases from 1.49 ns to 0.54 ns and further down to 0.28 ns. For the P to AP switching, both the mean value and the distribution of switching time decrease with the increase of pulse amplitude. The log-normal distribution function gives the mean switching times as 4.10 ns, 2.15 ns and 1.30 ns with the switching time distributions as 1.43 ns, 0.68 ns and 0.45 ns for the pulse amplitude -390 mV, -532 mV and -745 mV, respectively. It is noticed that the switching time distribution is proportional to the mean switching time, which is shown in Figure 6 5 (a) and (b) for AP to P and P to AP switching, respectively. The switching time variation coefficients, defined as the ratio between the switching time distribution and the mean switching time, are shown as the insert of Figure 6 5 (a) and (b) with the relation to the mean switching time.

In the thermal agitation switching regime, with the mean switching time up to milliseconds, the variation coefficient is found close to one. In this regime, the spin transfer torque excites the free layer dynamics and increases the system energy to certain level, while the energy dissipates through the damping process. Since the total energy

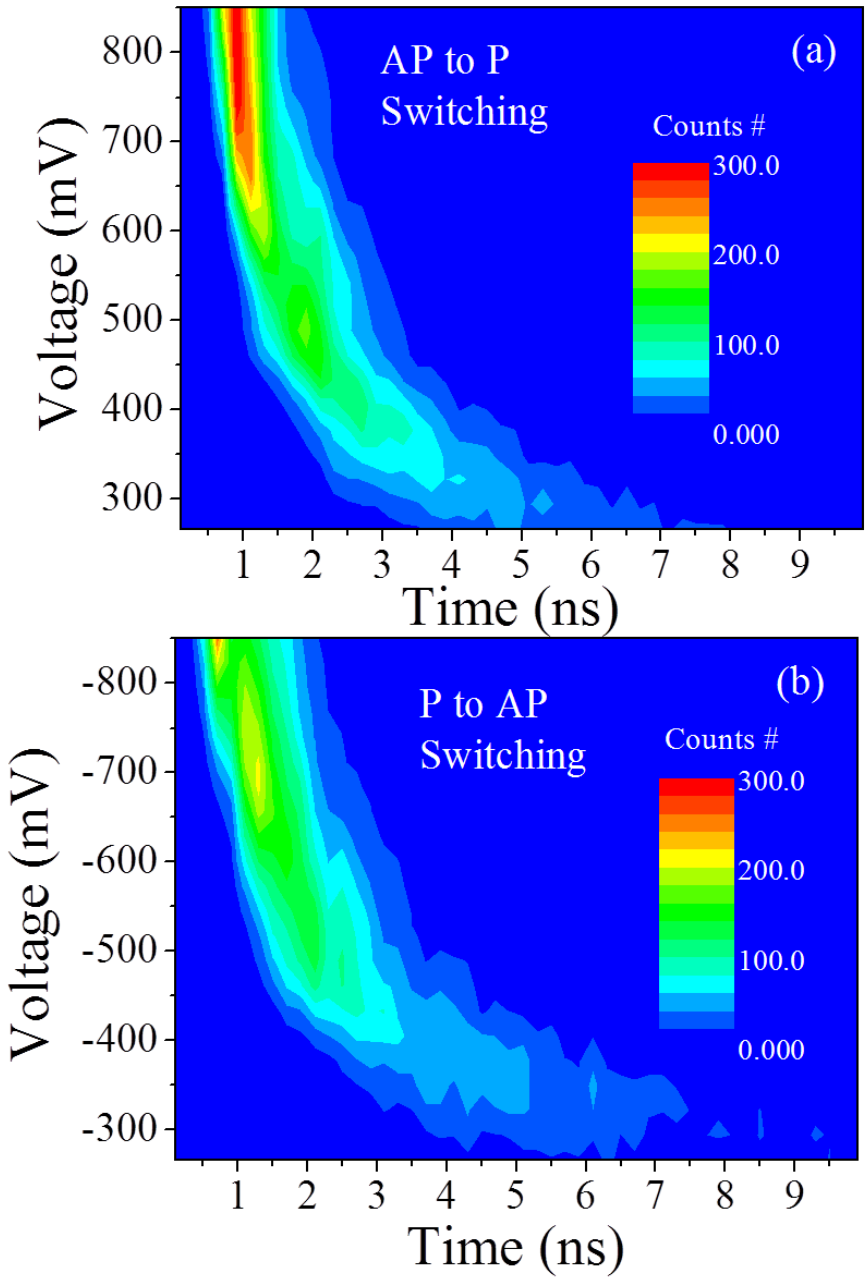


Figure 6-3 The time-voltage phase diagrams of the switching events for (a) anti-parallel to parallel and (b) parallel to anti-parallel.

gain is not enough for the switching, the magnetization still relies on the thermal agitation to trigger the switching. Therefore the switching time distribution approaches the Poisson distribution and the variation coefficient equals to one [149]. With the increase of the switching current, the free layer accumulates more energy to cross the energy barrier with less help from the thermal agitation. In this case, the switching time distribution is determined by both the thermal agitation switching and the precessional switching. The contribution of the precessional switching increases with the decrease of the mean switching time by applying a higher current. Therefore the switching time variation coefficient deviates from the constant value, one, and decreases with the mean switching time as the modeling indicated [149-150]. Hence, it would be very important to approximate the variation coefficient in the precessional switching regime. As we demonstrated in this work, the switching time variation coefficient remains almost constant as the switching time decreases from 7 ns to 1 ns, shown in the inserts of Figure 6-5 (a) and (b). A linear fit is applied to the mean switching time versus time distribution. Both AP to P and P to AP switching in this time region result a similar variation coefficient of about 0.38. In this regime, the switching is mainly determined by the magnetic dynamics driven by spin transfer torque rather than the thermal agitation. This dominated switching mechanism in this precessional switching regime is very sensitive to the initial magnetization of free layer, for instance the random angle between free layer and reference layer. In this case, the switching time distribution can be strongly affected by the initial magnetization of free layer which leads to the distributions as shown in Fig. 4 and limits the variation coefficient to further decrease.

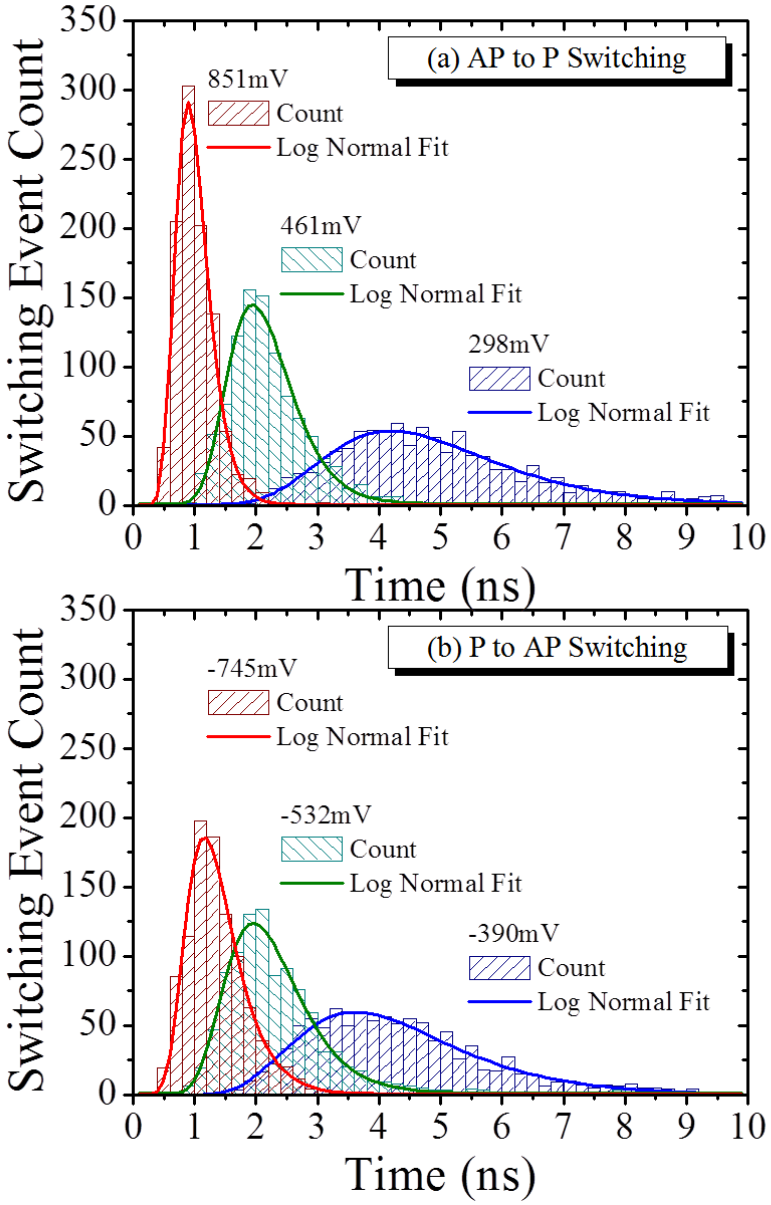


Figure 6-4 The switching time distributions at different voltages for both (a) anti-parallel to parallel and (b) parallel to anti-parallel.

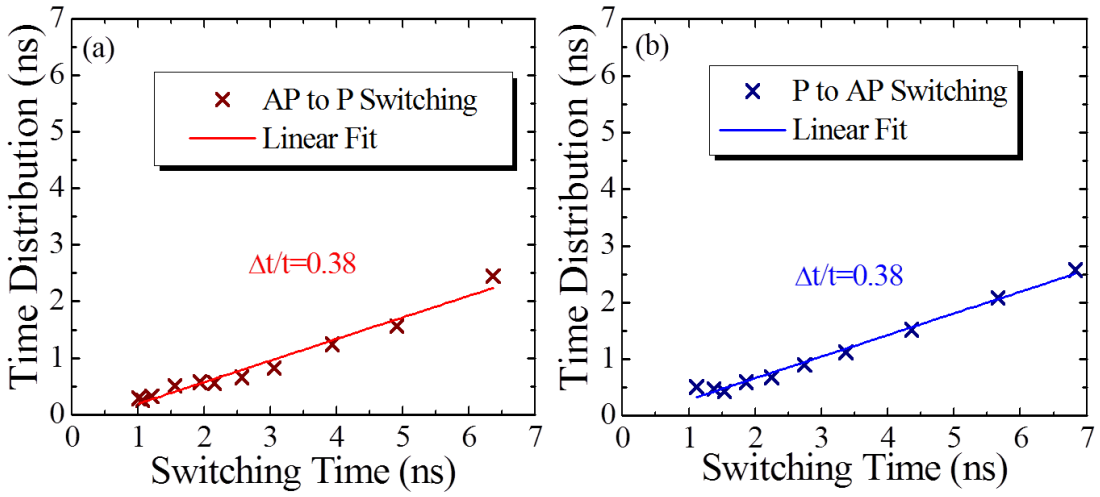


Figure 6-5 The switching time distribution changes with the average switching time for (a) anti-parallel to parallel and (b) parallel to anti-parallel.

## 6.4 Summary

In summary, we have used the single-shot time-domain measurement to study the dynamic switching for MTJs in the nanosecond precessional regime. The switching probability and distribution for switching events have been mapped in a voltage-time phase diagram. Switching time variation coefficient, the ratio of the time distribution and its mean value, was measured to be about 0.38 for both AP to P and P to AP. This result suggests a minimum of the switching time variation coefficient could be reached with future reduction of the switching time.

# Chapter 7. Conclusion and Future work

The spin transfer torque induced oscillation and switching were experimentally studied in the MgO barrier based magnetic tunnel junctions. In this thesis work, we focused on understanding and designing the spin torque oscillator in order to improve its key performance parameters, such as the oscillation operation condition, power output and linewidth. In addition, the oscillation modes were analyzed in the dual barrier magnetic tunnel junctions. For the spin transfer torque induced switching, the distribution of the switching time in the MgO barrier based magnetic tunnel junctions has been experimentally investigated in the precessional switching regime.

1. Based on the analysis of the power dependence on the tilted polarizer angle and magnetic free layer precession angle, we have fabricated spin torque oscillation devices with angular dependent polarizer directly by manipulating the shape anisotropy through the lithography and the pinning direction through the magnetic field post-annealing. The oscillation power increasing with the tilted polarizer angle was experimentally demonstrated, which qualitatively agrees with the analytical prediction. In addition, we found that the tilted polarizer tends to extend the operation current of the device.

2. Based on the learning from the power dependence on angle, we have designed and fabricated an external-field-free STO with a hard axis polarizer having a 90 degree configuration relative to the easy axis of the free layer. The hard axis polarizer STO provides much higher power output which was directly observed based on the time-domain voltage signal. Furthermore, the hard axis polarizer STO also lowered the critical current, due to much more efficient spin torque in the 90 degree configuration of the free and polarizer magnetic layers. In this case, the linewidth for the hard axis polarizer is

narrower under a lower operation current. This design also potentially extends the high end of the operation current range if the barrier breakdown voltage is higher. This is because the free magnetic layer is hard to be switched under this 90 degree configuration.

3. We have studied the spin torque oscillation modes of a dual MgO barrier MTJ with tilted polarizer. The frequency field dependence suggests that one of the modes appears to be the ordinary Kittel mode of the free layer, and the other might be due to the weakly-pinned top layer based on its markedly different dependences for opposite directions of the applied field.

4. For the spin torque induced magnetic switching, we have used the single-shot time-domain measurement to characterize the switching time of each switch under different voltages for MTJs in the nanosecond precessional regime. Using a statistical analysis, the switching time distributions for different voltages were mapped. The switching time variation coefficient, the ratio of the time distribution and its mean value, was measured to be about 0.38 for both anti-parallel to parallel and parallel to anti-parallel. This result suggests a minimum of the switching time variation coefficient could be reached with further reduction of the switching time.

For future research directions, the phase locking technique should be introduced for further improving the power and reducing the linewidth of the spin torque oscillators. One of the phase locking techniques is to couple all individual STOs electrically. One critical requirement for this method is to have high signal for each STO. The hard axis polarizer STOs designed and demonstrated in this thesis is a good candidate for the electrical phase locking.

# Bibliography


[1] M. N. Baibich, *et al.*, "Giant Magnetoresistance of (001)Fe/(001)Cr Magnetic Superlattices," *Physical Review Letters,* vol. 61, pp. 2472-2475, 1988.

[2] G. Binasch, *et al.*, "Enhanced magnetoresistance in layered magnetic structures with antiferromagnetic interlayer exchange," *Physical Review B,* vol. 39, pp. 4828-4830, 1989.

[3] N. F. Mott, "The electrical conductivity of transition metals," *Proc. R. Soc. Lond. A,* vol. 153, pp. 699-717, 1936.

[4] S. Zhang and P. M. Levy, "Conductivity perpendicular to the plane of multilayered structures," *Journal of Applied Physics,* vol. 69, pp. 4786-4788, 1991.

[5] W. P. Pratt, *et al.*, "PERPENDICULAR GIANT MAGNETORESISTANCES OF AG/CO MULTILAYERS," *Physical Review Letters,* vol. 66, pp. 3060-3063, Jun 10 1991.

[6] B. Dieny, *et al.*, "Magnetotransport properties of magnetically soft spin-valve structures (invited)," *Journal of Applied Physics,* vol. 69, pp. 4774-4779, 1991.

[7] T. Ching, *et al.*, "Design, fabrication and testing of spin-valve read heads for high density recording," *Magnetics, IEEE Transactions on,* vol. 30, pp. 3801-3806, 1994.

[8] B. Dieny, *et al.*, "GIANT MAGNETORESISTANCE IN SOFT FERROMAGNETIC MULTILAYERS," *Physical Review B,* vol. 43, pp. 1297-1300, Jan 1 1991.

[9] D. E. Heim, *et al.*, "Design and operation of spin valve sensors," *Magnetics, IEEE Transactions on,* vol. 30, pp. 316-321, 1994.

[10] J. M. Daughton, "GMR applications," *Journal of Magnetism and Magnetic Materials,* vol. 192, pp. 334-342, 1999.

[11] D. L. Graham, *et al.*, "Single magnetic microsphere placement and detection on-chip using current line designs with integrated spin valve sensors: Biotechnological applications," *Journal of Applied Physics,* vol. 91, pp. 7786-7788, 2002.

[12] P. P. Freitas, *et al.*, "Magnetoresistive biochips," *Europhysics News,* vol. 34, pp. 224-226, 2003.

[13] P. M. Tedrow and R. Meservey, "Spin-Dependent Tunneling into Ferromagnetic Nickel," *Physical Review Letters,* vol. 26, pp. 192-195, 1971.

[14] M. Julliere, "TUNNELING BETWEEN FERROMAGNETIC-FILMS," *Physics Letters A,* vol. 54, pp. 225-226, 1975 1975.

[15] J. S. Moodera, *et al.*, "Large Magnetoresistance at Room Temperature in Ferromagnetic Thin Film Tunnel Junctions," *Physical Review Letters,* vol. 74, pp. 3273-3276, 1995.

[16] T. Miyazaki and N. Tezuka, "Spin polarized tunneling in ferromagnet/insulator/ferromagnet junctions," *Journal of Magnetism and Magnetic Materials,* vol. 151, pp. 403-410, 1995.

[17] W. Dexin, *et al.*, "70% TMR at room temperature for SDT sandwich junctions with CoFeB as free and reference Layers," *Magnetics, IEEE Transactions on,* vol. 40, pp. 2269-2271, 2004.
[18] S. Yuasa, *et al.*, "Giant room-temperature magnetoresistance in single-crystal Fe/MgO/Fe magnetic tunnel junctions," *Nat Mater,* vol. 3, pp. 868-871, 2004.
[19] S. S. P. Parkin, *et al.*, "Giant tunnelling magnetoresistance at room temperature with MgO (100) tunnel barriers," *Nat Mater,* vol. 3, pp. 862-867, 2004.
[20] W. H. Butler, *et al.*, "Spin-dependent tunneling conductance of Fe|MgO|Fe sandwiches," *Physical Review B,* vol. 63, p. 054416, 2001.
[21] J. Mathon and A. Umerski, "Theory of tunneling magnetoresistance of an epitaxial Fe/MgO/Fe(001) junction," *Physical Review B,* vol. 63, p. 220403, 2001.
[22] W. H. Butler, "Tunneling magnetoresistance from a symmetry filtering effect," *Science and Technology of Advanced Materials,* vol. 9, p. 014106, 2008.
[23] G.-X. Miao, *et al.*, "Tunneling path toward spintronics," *Reports on Progress in Physics,* vol. 74, p. 036501, 2011.
[24] T. Kuwashima, *et al.*, "Electrical performance and reliability of tunnel magnetoresistance heads for 100-Gb/in<sup>2</sup> application," *Magnetics, IEEE Transactions on,* vol. 40, pp. 176-181, 2004.
[25] S. Mao, *et al.*, "Tunneling magnetoresistive heads beyond 150 Gb/in<sup>2</sup>," *Magnetics, IEEE Transactions on,* vol. 40, pp. 307-312, 2004.
[26] T. Kagami, *et al.*, "A performance study of next generation's TMR heads beyond 200 gb/in<sup>2</sup>," *Magnetics, IEEE Transactions on,* vol. 42, pp. 93-96, 2006.
[27] S. Mao, *et al.*, "Commercial TMR heads for hard disk drives: characterization and extendibility at 300 gbit/in<sup>2</sup>," *Magnetics, IEEE Transactions on,* vol. 42, pp. 97-102, 2006.
[28] A. Wang, "Pulse transfer controlling devices," *U.S. Patent,* vol. 2,708,722 A, 1955.
[29] E. P. G. Wright, "Electric connecting device," *U.S. Patent,* vol. 2,667,542 A, 1954.
[30] L. J. Schwee, *et al.*, "The concept and initial studies of a crosstie random access memory (CRAM)," *Journal of Applied Physics,* vol. 53, pp. 2762-2764, 1982.
[31] A. V. Pohm, *et al.*, "The design of a one megabit non-volatile M-R memory chip using 1.5×5 μm cells," *Magnetics, IEEE Transactions on,* vol. 24, pp. 3117-3119, 1988.
[32] J. M. Daughton, "Magnetoresistive memory technology," *Thin Solid Films,* vol. 216, pp. 162-168, 1992.
[33] D. D. Tang, *et al.*, "Spin-valve RAM cell," *Magnetics, IEEE Transactions on,* vol. 31, pp. 3206-3208, 1995.
[34] S. Tehrani, *et al.*, "High density nonvolatile magnetoresistive RAM," in *Electron Devices Meeting, 1996. IEDM '96., International,* 1996, pp. 193-196.
[35] S. S. P. Parkin, *et al.*, "Exchange-biased magnetic tunnel junctions and application to nonvolatile magnetic random access memory (invited)," *Journal of Applied Physics,* vol. 85, pp. 5828-5833, 1999.
[36] S. Tehrani, *et al.*, "Progress and outlook for MRAM technology," *Magnetics, IEEE Transactions on,* vol. 35, pp. 2814-2819, 1999.

[37] P. K. Naji, *et al.*, "A 256 kb 3.0 V 1T1MTJ nonvolatile magnetoresistive RAM," in *Solid-State Circuits Conference, 2001. Digest of Technical Papers. ISSCC. 2001 IEEE International*, 2001, pp. 122-123.

[38] M. Durlam, *et al.*, "A low power 1 Mbit MRAM based on 1T1MTJ bit cell integrated with copper interconnects," in *VLSI Circuits Digest of Technical Papers, 2002. Symposium on*, 2002, pp. 158-161.

[39] B. N. Engel, *et al.*, "A 4-Mb toggle MRAM based on a novel bit and switching method," *Magnetics, IEEE Transactions on*, vol. 41, pp. 132-136, 2005.

[40] W. J. Gallagher and S. S. P. Parkin, "Development of the magnetic tunnel junction MRAM at IBM: From first junctions to a 16-Mb MRAM demonstrator chip," *IBM Journal of Research and Development*, vol. 50, pp. 5-23, 2006.

[41] J. C. Slonczewski, "Current-driven excitations of magnetic multilayers," *J. Magn. Magn. Mater.*, vol. 159, pp. L1-L7, 1996.

[42] L. Berger, "Emission of spin waves by a magnetic multilayer traversed by a current," *Physical Review B*, vol. 54, p. 9353, 1996.

[43] M. Tsoi, *et al.*, "Excitation of a Magnetic Multilayer by an Electric Current," *Physical Review Letters*, vol. 80, p. 4281, 1998.

[44] E. B. Myers, *et al.*, "Current-Induced Switching of Domains in Magnetic Multilayer Devices," *Science*, vol. 285, pp. 867-870, August 6, 1999 1999.

[45] J. Z. Sun, "Current-driven magnetic switching in manganite trilayer junctions," *Journal of Magnetism and Magnetic Materials*, vol. 202, pp. 157-162, 1999.

[46] M. R. Pufall, *et al.*, "Materials dependence of the spin-momentum transfer efficiency and critical current in ferromagnetic metal/Cu multilayers," *Applied Physics Letters*, vol. 83, pp. 323-325, 2003.

[47] S. Mangin, *et al.*, "Current-induced magnetization reversal in nanopillars with perpendicular anisotropy," *Nat Mater*, vol. 5, pp. 210-215, 2006.

[48] H. Meng and J.-P. Wang, "Spin transfer in nanomagnetic devices with perpendicular anisotropy," *Applied Physics Letters*, vol. 88, pp. -, 2006.

[49] Y. Liu, *et al.*, "Current-induced magnetization switching in magnetic tunnel junctions," *Applied Physics Letters*, vol. 82, pp. 2871-2873, 2003.

[50] Y. Huai, *et al.*, "Observation of spin-transfer switching in deep submicron-sized and low-resistance magnetic tunnel junctions," *Applied Physics Letters*, vol. 84, pp. 3118-3120, 2004.

[51] Z. Diao, *et al.*, "Spin transfer switching and spin polarization in magnetic tunnel junctions with MgO and AlOx barriers," *Applied Physics Letters*, vol. 87, pp. -, 2005.

[52] J. Hayakawa, *et al.*, "Current-Driven Magnetization Switching in CoFeB/MgO/CoFeB Magnetic Tunnel Junctions," *Jpn. J. Appl. Phys.*, vol. 44, p. 4, 2005.

[53] S. Ikeda, *et al.*, "A perpendicular-anisotropy CoFeB–MgO magnetic tunnel junction," *Nat Mater*, vol. 9, pp. 721-724, 2010.

[54] S. Zhang, *et al.*, "Mechanisms of Spin-Polarized Current-Driven Magnetization Switching," *Physical Review Letters*, vol. 88, p. 236601, 2002.

[55] J. C. Slonczewski, "Currents, torques, and polarization factors in magnetic tunnel junctions," *Physical Review B*, vol. 71, p. 024411, 2005.

[56] Z. Li, *et al.*, "Perpendicular Spin Torques in Magnetic Tunnel Junctions," *Physical Review Letters,* vol. 100, p. 246602, 2008.
[57] K. Xia, *et al.*, "Spin torques in ferromagnetic/normal-metal structures," *Physical Review B,* vol. 65, p. 220401, 2002.
[58] S. Urazhdin, *et al.*, "Current-Driven Magnetic Excitations in Permalloy-Based Multilayer Nanopillars," *Physical Review Letters,* vol. 91, p. 146803, 2003.
[59] M. A. Zimmler, *et al.*, "Current-induced effective magnetic fields in Co/Cu/Co nanopillars," *Physical Review B,* vol. 70, p. 184438, 2004.
[60] S. Petit, *et al.*, "Spin-Torque Influence on the High-Frequency Magnetization Fluctuations in Magnetic Tunnel Junctions," *Physical Review Letters,* vol. 98, p. 077203, 2007.
[61] H. Kubota, *et al.*, "Quantitative measurement of voltage dependence of spin-transfer torque in MgO-based magnetic tunnel junctions," *Nat Phys,* vol. 4, pp. 37-41, 2008.
[62] J. C. Sankey, *et al.*, "Measurement of the spin-transfer-torque vector in magnetic tunnel junctions," *Nat Phys,* vol. 4, pp. 67-71, 2008.
[63] J. Z. Sun, "Spin-current interaction with a monodomain magnetic body: A model study," *Physical Review B,* vol. 62, pp. 570-578, 2000.
[64] E. B. Myers, *et al.*, "Thermally Activated Magnetic Reversal Induced by a Spin-Polarized Current," *Physical Review Letters,* vol. 89, p. 196801, 2002.
[65] Z. Li and S. Zhang, "Thermally assisted magnetization reversal in the presence of a spin-transfer torque," *Physical Review B,* vol. 69, p. 134416, 2004.
[66] M. Nakayama, *et al.*, "Spin transfer switching in TbCoFe / CoFeB / MgO / CoFeB / TbCoFe magnetic tunnel junctions with perpendicular magnetic anisotropy," *Journal of Applied Physics,* vol. 103, pp. -, 2008.
[67] D. C. Worledge, *et al.*, "Spin torque switching of perpendicular Ta | CoFeB | MgO-based magnetic tunnel junctions," *Applied Physics Letters,* vol. 98, pp. -, 2011.
[68] D. Bedau, *et al.*, "Spin-transfer pulse switching: From the dynamic to the thermally activated regime," *Applied Physics Letters,* vol. 97, pp. -, 2010.
[69] M. Gajek, *et al.*, "Spin torque switching of 20 nm magnetic tunnel junctions with perpendicular anisotropy," *Applied Physics Letters,* vol. 100, pp. -, 2012.
[70] G. D. Fuchs, *et al.*, "Adjustable spin torque in magnetic tunnel junctions with two fixed layers," *Applied Physics Letters,* vol. 86, pp. -, 2005.
[71] H. Meng, *et al.*, "Low critical current for spin transfer in magnetic tunnel junctions," *Applied Physics Letters,* vol. 88, pp. -, 2006.
[72] Z. Diao, *et al.*, "Spin transfer switching in dual MgO magnetic tunnel junctions," *Applied Physics Letters,* vol. 90, pp. -, 2007.
[73] H. Meng and J.-P. Wang, "Composite free layer for high density magnetic random access memory with lower spin transfer current," *Applied Physics Letters,* vol. 89, pp. -, 2006.
[74] Y. Zhang, *et al.*, "Spin-transfer-induced magnetization switching in tunnel junctions with nanocurrent channels," *Applied Physics Letters,* vol. 90, pp. -, 2007.
[75] X. Yao, *et al.*, "Improved current switching symmetry of magnetic tunneling junction and giant magnetoresistance devices with nano-current-channel structure," *Journal of Applied Physics,* vol. 103, pp. -, 2008.

[76] X. Chen and R. H. Victora, "Exchange-assisted spin transfer torque switching," *U.S. Patent*, vol. 8,134,864 B2, 2012.
[77] A. D. Kent, *et al.*, "Spin-transfer-induced precessional magnetization reversal," *Applied Physics Letters*, vol. 84, pp. 3897-3899, 2004.
[78] O. J. Lee, *et al.*, "Ultrafast switching of a nanomagnet by a combined out-of-plane and in-plane polarized spin current pulse," *Applied Physics Letters*, vol. 95, pp. -, 2009.
[79] C. Papusoi, *et al.*, "100 ps precessional spin-transfer switching of a planar magnetic random access memory cell with perpendicular spin polarizer," *Applied Physics Letters*, vol. 95, pp. -, 2009.
[80] H. Liu, *et al.*, "Ultrafast switching in magnetic tunnel junction based orthogonal spin transfer devices," *Applied Physics Letters*, vol. 97, pp. -, 2010.
[81] G. E. Rowlands, *et al.*, "Deep subnanosecond spin torque switching in magnetic tunnel junctions with combined in-plane and perpendicular polarizers," *Applied Physics Letters*, vol. 98, pp. -, 2011.
[82] I. N. Krivorotov, *et al.*, "Time-Domain Measurements of Nanomagnet Dynamics Driven by Spin-Transfer Torques," *Science*, vol. 307, pp. 228-231, January 14, 2005 2005.
[83] T. Devolder, *et al.*, "Single-Shot Time-Resolved Measurements of Nanosecond-Scale Spin-Transfer Induced Switching: Stochastic Versus Deterministic Aspects," *Physical Review Letters*, vol. 100, p. 057206, 2008.
[84] K. K. Hiroyuki Tomita, Takayuki Nozaki, Hitoshi Kubota, Akio Fukushima, Kay Yakushiji, Shinji Yuasa, Yoshinobu Nakatani, Teruya Shinjo, Masashi Shiraishi and Yoshishige Suzuki, "Single-Shot Measurements of Spin-Transfer Switching in CoFeB/MgO/CoFeB Magnetic Tunnel Junctions," *Appl. Phys. Express*, vol. 1, p. 061303 2008.
[85] I. N. Krivorotov, *et al.*, "Time-domain studies of very-large-angle magnetization dynamics excited by spin transfer torques," *Physical Review B*, vol. 77, p. 054440, 2008.
[86] Y. T. Cui, *et al.*, "Single-Shot Time-Domain Studies of Spin-Torque-Driven Switching in Magnetic Tunnel Junctions," *Physical Review Letters*, vol. 104, p. 097201, 2010.
[87] M. Hosomi, *et al.*, "A novel nonvolatile memory with spin torque transfer magnetization switching: spin-ram," in *Electron Devices Meeting, 2005. IEDM Technical Digest. IEEE International*, 2005, pp. 459-462.
[88] T. Kawahara, *et al.*, "2 Mb SPRAM (SPin-Transfer Torque RAM) With Bit-by-Bit Bi-Directional Current Write and Parallelizing-Direction Current Read," *Solid-State Circuits, IEEE Journal of*, vol. 43, pp. 109-120, 2008.
[89] A. Raychowdhury, *et al.*, "Design space and scalability exploration of 1T-1STT MTJ memory arrays in the presence of variability and disturbances," in *Electron Devices Meeting (IEDM), 2009 IEEE International*, 2009, pp. 1-4.
[90] A. Driskill-Smith, *et al.*, "Non-volatile spin-transfer torque RAM (STT-RAM): Data, analysis and design requirements for thermal stability," in *VLSI Technology (VLSIT), 2010 Symposium on*, 2010, pp. 51-52.

[91] M. Tai, *et al.*, "A Study of Write Margin of Spin Torque Transfer Magnetic Random Access Memory Technology," *Magnetics, IEEE Transactions on,* vol. 46, pp. 2322-2327, 2010.
[92] L. Young Min, *et al.*, "Highly scalable STT-MRAM with MTJs of top-pinned structure in 1T/1MTJ cell," in *VLSI Technology (VLSIT), 2010 Symposium on*, 2010, pp. 49-50.
[93] J. J. Nowak, *et al.*, "Demonstration of Ultralow Bit Error Rates for Spin-Torque Magnetic Random-Access Memory With Perpendicular Magnetic Anisotropy," *Magnetics Letters, IEEE,* vol. 2, pp. 3000204-3000204, 2011.
[94] T. Kawahara, *et al.*, "Spin-transfer torque RAM technology: Review and prospect," *Microelectronics Reliability,* vol. 52, pp. 613-627, 2012.
[95] J. A. Katine, *et al.*, "Current-driven magnetization reversal and spin-wave excitations in Co/Cu/Co pillars," *Physical Review Letters,* vol. 84, pp. 3149-3152, Apr 3 2000.
[96] M. Tsoi, *et al.*, "Generation and detection of phase-coherent current-driven magnons in magnetic multilayers," *Nature,* vol. 406, pp. 46-48, 2000.
[97] B. Ozyilmaz, "Current-induced magnetization reversal in high magnetic fields in Co/Cu/Co nanopillars," *Phys. Rev. Lett.,* vol. 91, pp. 067203-067203, 2003.
[98] W. H. Rippard, *et al.*, "Quantitative studies of spin-momentum-transfer-induced excitations in Co/Cu multilayer films using point-contact spectroscopy," *Appl. Phys. Lett.,* vol. 82, pp. 1260-1262, 2003.
[99] S. I. Kiselev, *et al.*, "Microwave oscillations of a nanomagnet driven by a spin-polarized current," *Nature,* vol. 425, pp. 380-383, 2003.
[100] D. Houssameddine, *et al.*, "Temporal Coherence of MgO Based Magnetic Tunnel Junction Spin Torque Oscillators," *Physical Review Letters,* vol. 102, p. 257202, 2009.
[101] S. Bonetti, *et al.*, "Experimental Evidence of Self-Localized and Propagating Spin Wave Modes in Obliquely Magnetized Current-Driven Nanocontacts," *Physical Review Letters,* vol. 105, p. 217204, 2010.
[102] P. K. Muduli, *et al.*, "Decoherence and Mode Hopping in a Magnetic Tunnel Junction Based Spin Torque Oscillator," *Physical Review Letters,* vol. 108, p. 207203, 2012.
[103] G. E. Rowlands, *et al.*, "Time Domain Mapping of Spin Torque Oscillator Effective Energy," *Physical Review Letters,* vol. 111, p. 087206, 2013.
[104] D. Houssameddine, *et al.*, "Spin-torque oscillator using a perpendicular polarizer and a planar free layer," *Nat Mater,* vol. 6, pp. 447-453, 2007.
[105] W. Jin, *et al.*, "Spin-Wave Excitations in Nanopillars With Perpendicular Polarizers," *Magnetics, IEEE Transactions on,* vol. 42, pp. 2682-2684, 2006.
[106] X. Zhu and J.-G. Zhu, "Bias-Field-Free Microwave Oscillator Driven by Perpendicularly Polarized Spin Current," *Magnetics, IEEE Transactions on,* vol. 42, pp. 2670-2672, 2006.
[107] C. Kittel, "Introduction to Solid State Physics," ed, 1996.
[108] W. H. Rippard, *et al.*, "Direct-current induced dynamics in Co90Fe10/Ni80Fe20 point contacts," *Physical Review Letters,* vol. 92, Jan 16 2004.

[109] A. N. Slavini and P. Kabos, "Approximate theory of microwave generation in a current-driven magnetic nanocontact magnetized in an arbitrary direction," *Magnetics, IEEE Transactions on,* vol. 41, pp. 1264-1273, 2005.
[110] A. Slavin and V. Tiberkevich, "Nonlinear Auto-Oscillator Theory of Microwave Generation by Spin-Polarized Current," *Ieee Transactions on Magnetics,* vol. 45, pp. 1875-1918, Apr 2009.
[111] J. C. Sankey, *et al.*, "Mechanisms limiting the coherence time of spontaneous magnetic oscillations driven by dc spin-polarized currents," *Physical Review B,* vol. 72, p. 224427, 2005.
[112] J.-V. Kim, *et al.*, "Generation Linewidth of an Auto-Oscillator with a Nonlinear Frequency Shift: Spin-Torque Nano-Oscillator," *Physical Review Letters,* vol. 100, p. 017207, 2008.
[113] M. L. Schneider, *et al.*, "Temperature dependence of spin-torque-driven self-oscillations," *Physical Review B,* vol. 80, p. 144412, 2009.
[114] K. V. Thadani, *et al.*, "Strong linewidth variation for spin-torque nano-oscillators as a function of in-plane magnetic field angle," *Physical Review B,* vol. 78, p. 024409, 2008.
[115] J.-V. Kim, *et al.*, "Line Shape Distortion in a Nonlinear Auto-Oscillator Near Generation Threshold: Application to Spin-Torque Nano-Oscillators," *Physical Review Letters,* vol. 100, p. 167201, 2008.
[116] B. Georges, *et al.*, "Origin of the spectral linewidth in nonlinear spin-transfer oscillators based on MgO tunnel junctions," *Physical Review B,* vol. 80, p. 060404, 2009.
[117] A. M. Deac, *et al.*, "Bias-driven high-power microwave emission from MgO-based tunnel magnetoresistance devices," *Nat Phys,* vol. 4, pp. 803-809, 2008.
[118] S. Kaka, *et al.*, "Mutual phase-locking of microwave spin torque nano-oscillators," *Nature,* vol. 437, pp. 389-392, Sep 15 2005.
[119] J. Grollier, *et al.*, "Synchronization of spin-transfer oscillators driven by stimulated microwave currents," *Physical Review B,* vol. 73, p. 060409, 2006.
[120] D. Houssameddine, *et al.*, "Spin transfer induced coherent microwave emission with large power from nanoscale MgO tunnel junctions," *Applied Physics Letters,* vol. 93, pp. 022505-3, 2008.
[121] J.-G. Zhu, *et al.*, "Microwave Assisted Magnetic Recording," *Magnetics, IEEE Transactions on,* vol. 44, pp. 125-131, 2008.
[122] F. B. Mancoff, *et al.*, "Phase-locking in double-point-contact spin-transfer devices," *Nature,* vol. 437, pp. 393-395, Sep 15 2005.
[123] X. Chen and R. H. Victora, "Phase locking of spin-torque oscillators by spin-wave interactions," *Physical Review B,* vol. 79, p. 180402, 2009.
[124] W. H. Rippard, *et al.*, "Injection Locking and Phase Control of Spin Transfer Nano-oscillators," *Physical Review Letters,* vol. 95, p. 067203, 2005.
[125] Z. Li, *et al.*, "Dynamic magnetization states of a spin valve in the presence of dc and ac currents: Synchronization, modification, and chaos," *Physical Review B,* vol. 74, p. 054417, 2006.
[126] B. Georges, *et al.*, "Impact of the electrical connection of spin transfer nano-oscillators on their synchronization: an analytical study," *Applied Physics Letters,* vol. 92, pp. -, 2008.

[127] P. M. Braganca, *et al.*, "Nanoscale magnetic field detection using a spin torque oscillator," *Nanotechnology,* vol. 21, p. 235202, 2010.
[128] S. E. Russek, *et al.*, *Spin-Transfer Nano-Oscillators*: CRC Press, 2010.
[129] S. Kaka, *et al.*, "CPP reader with phase detection of magnetic resonance for read-back," ed: Google Patents, 2009.
[130] H. Meng, "Spin transfer in nano-magnetic devices with new structures," Ph.D, Electrical and computer engineering, University of Minnesota, 2007.
[131] C. Wang, *et al.*, "Bias and angular dependence of spin-transfer torque in magnetic tunnel junctions," *Physical Review B,* vol. 79, p. 224416, 2009.
[132] O. Boulle, *et al.*, "Shaped angular dependence of the spin-transfer torque and microwave generation without magnetic field," *Nat Phys,* vol. 3, pp. 492-497, 2007.
[133] W. H. Rippard, *et al.*, "Current-driven microwave dynamics in magnetic point contacts as a function of applied field angle," *Physical Review B,* vol. 70, p. 100406, 2004.
[134] S. Bonetti, *et al.*, "Spin torque oscillator frequency versus magnetic field angle: The prospect of operation beyond 65 GHz," *Applied Physics Letters,* vol. 94, pp. 102507-3, 2009.
[135] Y. Zhou, *et al.*, "Spin-torque oscillator with tilted fixed layer magnetization," *Applied Physics Letters,* vol. 92, pp. 262508-3, 2008.
[136] F. B. Mancoff, *et al.*, "Angular dependence of spin-transfer switching in a magnetic nanostructure," *Applied Physics Letters,* vol. 83, pp. 1596-1598, 2003.
[137] Y. Zhang, *et al.*, "Power enhancement of angular polarizer spin torque oscillator in magnetic tunnel junction," *Journal of Applied Physics,* vol. 109, pp. -, 2011.
[138] G. Gerhart, *et al.*, "Angular dependence of the microwave-generation threshold in a nanoscale spin-torque oscillator," *Physical Review B,* vol. 76, p. 024437, 2007.
[139] Y. Zhang, *et al.*, "High power and low critical current spin torque oscillation from a magnetic tunnel junction with a built-in hard axis polarizer," *Applied Physics Letters,* vol. 100, pp. -, 2012.
[140] J. P. Park, *et al.*, "Spatially Resolved Dynamics of Localized Spin-Wave Modes in Ferromagnetic Wires," *Physical Review Letters,* vol. 89, p. 277201, 2002.
[141] Y. Guan, *et al.*, "Field and bias dependence of high-frequency magnetic noise in MgO-based magnetic tunnel junctions," *Journal of Applied Physics,* vol. 105, pp. 07D127-3, 2009.
[142] J. M. Shaw, *et al.*, "Spin dynamics and mode structure in nanomagnet arrays: Effects of size and thickness on linewidth and damping," *Physical Review B,* vol. 79, p. 184404, 2009.
[143] D. Gusakova, *et al.*, "Spin-polarized current-induced excitations in a coupled magnetic layer system," *Physical Review B,* vol. 79, p. 104406, 2009.
[144] D. Houssameddine, *et al.*, "Spin torque driven excitations in a synthetic antiferromagnet," *Applied Physics Letters,* vol. 96, pp. 072511-3, 2010.
[145] A. Konovalenko, *et al.*, "Spin dynamics of two-coupled nanomagnets in spin-flop tunnel junctions," *Physical Review B,* vol. 80, p. 144425, 2009.
[146] B. Heinrich, *et al.*, "Dynamic Exchange Coupling in Magnetic Bilayers," *Physical Review Letters,* vol. 90, p. 187601, 2003.

[147] Y. Zhang, *et al.*, "Spin torque oscillation modes of a dual magnetic tunneling junction," *Journal of Applied Physics*, vol. 109, pp. -, 2011.
[148] H. Zhao, *et al.*, "Spin-Transfer Torque Switching Above Ambient Temperature," *Magnetics Letters, IEEE*, vol. 3, pp. 3000304-3000304, 2012.
[149] X. Wang, *et al.*, "Spin Torque Induced Magnetization Switching Variations," *Magnetics, IEEE Transactions on*, vol. 45, pp. 2038-2041, 2009.
[150] X. Wang, "Exploration on sub-nanosecond spin torque random access memory," *in Proc. IEEE GLOBECOM Workshops*, pp. 1881-1885, 2010 2010.
[151] T. Aoki, *et al.*, "Spin transfer switching in the nanosecond regime for CoFeB/MgO/CoFeB ferromagnetic tunnel junctions," *Journal of Applied Physics*, vol. 103, pp. 103911-4, 2008.

# Appendix A: Current perpendicular to plane device lithography flow.

## A.1. Process flow based on positive ebeam resist

| Step | Process Detail |
|---|---|
| 1. Bottom electrode lithography | Prebake: 115C for 1 minute. |
| | Photoresist coating: PR1813 at 4000 RPM for 30 seconds (around 18000Å thick). |
| | Softbake: 105C for 1 minute. |
| | Exposure: Vacuum contact, mask I, 4.5 seconds |
| | Develop: Solution: H2O:351=5:1 for 25 seconds, DI wafer rinse and N2 blow dry |
| | Hardbake: 120C for 1 minute |
| 2. Bottom electrode milling | Angle: 60 degree, Rotation: 4RPM, Reference: full stack on glass, Process: etch 3 minutes stop 3 minutes. |
| 3. Photo resist remove | Acetone Ultrasonic(48%) for 10 minutes, DI water rinse, N2 blow dry |
| | O2 clean (100W) 2 minutes. |
| 4. Measure the bottom electrode step | Measure the etched height across the wafer. |
| 5. Ebeam resist coating | Prebake: 265C for 1 minute. |
| | Ebeam resist coating: PMGI(SF6) at 3000RPM for 1 minute. |
| | Softbake: 265C for 1 minute. |

| | |
|---|---|
| | Ebeam resist coating: PMMA(C2 950K) at 3000RPM for 1 minute. |
| | Softbake: 180C for 2 minute. |
| 6. Ebeam resist exposure | Voltage=100kV, app=10um, current=1nA, dose= uC/cm2, align mark p20, |
| 7. Ebeam resist develop | MIBK:IPA (1:3) for 30 sec and IPA rinse for PMMA. |
| | CD26:DI water (6:4) for 5min and DI water rinse for PMGI. |
| | Blow dry with N2. |
| 8. Residual resist clean | O2 clean (100W) 5 seconds. |
| 9. Hard mask deposit | electrical beam evaporator deposit 80 nm Ti |
| 10. Hard mask lift off | NMP solution on hot plate (185C) (solution about 90-100C), DI water rinse, N2 blow dry |
| 11. Device milling | Angle: 10 degree+70 degree(1minute side clean), Rotation: 4RPM, Reference: device stack + capping on glass. |
| 12. SiO2 deposit | PECVD Recipe: SiO2150, thickness=50 nm. |
| 13. Measure the SiO2 thickness | Measure the total SiO2 thickness for planarization process. |
| 14. Photo resist coating for planarization | Prebake: 150C for 5 minutes. |
| | HMDS 5 minutes. |
| | Photoresist coating: PR1805 spray at 500 RPM for 10 seconds then spin at 4000RPM for 30 seconds. |
| | Surface flatten bake: 50C for 3 minutes and then 105C for 1 minutes. |
| 15. Planarization | Measure the thickness of PR1805 (Recipe: resist on SiO2 on thermal SiO2 on Si) |
| | PR1805 etching (Recipe: planr12: Ar 70sccm, CF 47sccm, CHF3 |

| | |
|---|---|
| | 6sccm) |
| | Measure the thickness of residual PR1805 (Recipe: resist on SiO2 on thermal SiO2 on Si) |
| | PR1805 and SiO2 etching (Recipe: planr12: Ar 70sccm, CF 47sccm, CHF3 6sccm) |
| | Measure the thickness of SiO2 (Recipe: SiO2 on thermal SiO2 on Si) |
| 16. Bottom electrode VIA lithography | Prebake: 115C for 1 minute. |
| | Photoresist coating: PR1813 at 4000 RPM for 30 seconds (around 18000Å thick). |
| | Softbake: 105C for 1 minute. |
| | Exposure: Vacuum contact, mask II, 4.5 seconds |
| | Develop: Solution: H2O:351=5:1 for 25 seconds, DI wafer rinse and N2 blow dry |
| | Hardbake: 120C for 1 minute |
| 17. VIA open (SiO2 etching) | SiO2 etching (Recipe: planr12: Ar 70sccm, CF 47sccm, CHF3 6sccm), targeting the residual PECVD SiO2 thickness |
| 18. Residual photo resist clean | Acetone Ultrasonic(48%) for 10 minutes, DI water rinse, N2 blow dry |
| | O2 clean (100W) 2 minutes. |
| 19. Top and Bottom electrodes lithography | Prebake: 115C for 1 minute. |
| | Photoresist coating: PR1813 at 4000 RPM for 30 seconds (around 18000Å thick). |
| | Softbake: 105C for 1 minute. |
| | Exposure: Vacuum contact, mask III, 5 seconds |

| | |
|---|---|
| | Develop: Solution: H2O:351=5:1 for 30 seconds, DI wafer rinse and N2 blow dry |
| | Hardbake: 120C for 1 minute |
| 20. Electrodes deposit | Electrical beam evaporator deposit: Ti 10nm /Au 200nm. |
| 21. Electrodes Lift off | Developer 1165 on hot plate (110C) untill the metal off, DI water rinse, N2 blow dry |

# A.2. Process flow based on negative ebeam resist

| Step | Process Detail |
|---|---|
| 1. Bottom electrode lithography | Prebake: 115C for 1 minute. |
| | Photoresist coating: PR1813 at 4000 RPM for 30 seconds (around 18000Å thick). |
| | Softbake: 105C for 1 minute. |
| | Exposure: Vacuum contact, mask I, 4.5 seconds |
| | Develop: Solution: H2O:351=5:1 for 25 seconds, DI wafer rinse and N2 blow dry |
| | Hardbake: 120C for 1 minute |
| 2. Bottom electrode milling | Angle: 60 degree, Rotation: 4RPM, Reference: full stack on glass, Process: etch 3 minutes stop 3 minutes. |
| 3. Photo resist remove | Acetone Ultrasonic(48%) for 10 minutes, DI water rinse, N2 blow dry |
| | O2 clean (100W) 2 minutes. |
| 4. Measure the bottom electrode step | Measure the etched height across the wafer. |

| | |
|---|---|
| 5. Ebeam resist coating | Prebake: 170C for 15 minute. |
| | HMDS 5 minutes. |
| | Ebeam resist coating: NEB31 at 6000RPM for 1 minute. |
| | Softbake: 110C for 2 minute. |
| 6. Ebeam resist exposure | Voltage=100kV, app=10um, current=1nA, dose= ~100 uC/cm2, align mark p20, |
| 7. Ebeam resist develop | Hardbake: 95C for 4 minute |
| | MF319 10 seconds |
| | DI water rinse. Blow dry with N2. |
| 8. Device milling | Angle: 10 degree+70 degree(1minute side clean), Rotation: 4RPM, Reference: device stack + capping on glass. |
| 9. SiO2 deposit | Electrical beam evaporator deposit SiO2 |
| 10. SiO2 lift off | NMP on hotplate and the ultrasonic, repeat untill most of the devices lift off. |
| 11. Measure the SiO2 thickness | Measure the total SiO2 thickness for VIA open. |
| 12. Bottom electrode VIA lithography | Prebake: 115C for 1 minute. |
| | Photoresist coating: PR1813 at 4000 RPM for 30 seconds (around 18000Å thick). |
| | Softbake: 105C for 1 minute. |
| | Exposure: Vacuum contact, mask II, 4.5 seconds |
| | Develop: Solution: H2O:351=5:1 for 25 seconds, DI wafer rinse and N2 blow dry |
| | Hardbake: 120C for 1 minute |
| 13. VIA open (SiO2 | SiO2 etching (Recipe: planr12: Ar 70sccm, CF 47sccm, CHF3 |

| | |
|---|---|
| etching) | 6sccm), targeting the residual SiO2 thickness |
| 14. Residual photo resist clean | Acetone Ultrasonic(48%) for 10 minutes, DI water rinse, N2 blow dry |
| | O2 clean (100W) 2 minutes. |
| 15. Top and Bottom electrodes lithography | Prebake: 115C for 1 minute. |
| | Photoresist coating: PR1813 at 4000 RPM for 30 seconds (around 18000Å thick). |
| | Softbake: 105C for 1 minute. |
| | Exposure: Vacuum contact, mask III, 5 seconds |
| | Develop: Solution: H2O:351=5:1 for 30 seconds, DI wafer rinse and N2 blow dry |
| | Hardbake: 120C for 1 minute |
| 16. Electrodes deposit | Electrical beam evaporator deposit: Ti 10nm /Au 200nm. |
| 17. Electrodes Lift off | Developer 1165 on hot plate (110C) untill the metal off, DI water rinse, N2 blow dry |